

Modelling of Electromagnetic Fields in MICs Based on Full-wave Space-Time Discrete Numerical Techniques

by

Shujun Xiao

B.S., Beijing Institute of Technology, 1983

M.S., Beijing Institute of Technology, 1986

A Dissertation Submitted in Partial Fulfillment of the
Requirement for the Degree of

DOCTOR OF PHILOSOPHY

in the Department of Electrical and Computer Engineering

We accept this dissertation as conforming
to the required standard

Dr. R. Vahldieck, Supervisor (Dept. of Elec. and Comp. Eng.)

Dr. J. Bornemann, Departmental Member (Dept. of Elec. and Comp. Eng.)

Dr. L. Kirlin, Departmental Member (Dept. of Elec. and Comp. Eng.)

Dr. N. Djilali, Outside Member (Dept. of Mech. Eng.)

Dr. K. Wu, External Examiner (Ecole Polytechnique de Montreal)

© Shujun Xiao, 1996

University of Victoria

All rights reserved. This dissertation may not be reproduced in whole or in part, by photocopy or other means, without the permission of the author

Supervisor: Dr. Ruediger Vahldieck,

ABSTRACT

Numerical modelling of electromagnetic fields is an indispensable part in the design of modern communications equipment. For this purpose a variety of numerical techniques have been developed in recent years. The most attractive ones are those that rely on the discretization of space. Two of them, the finite difference time domain method (FDTD) and the method of lines (MoL) are selected in this thesis. Their algorithms are refined and applied to analyze a variety of planar transmission line structures and metal waveguide components.

The reason to focus on these two methods is the following:

The FDTD method is one of the most powerful time domain methods which, compared with other time domain techniques, is most flexible and requires the least number of field variables. However, a commonly known problem in the application of the FDTD method is the significant amount of computer memory and run-time required to resolve fine circuit details with sufficient accuracy. To alleviate this problem, a variable grading scheme with second order accuracy is developed. Furthermore, a new two dimensional hybrid FDTD scheme with real variables is developed and tested in the analysis of planar superconductor transmission lines with very thin conductor layer.

The FDTD method is a time domain method which carries substantial computational overhead when applied to the analysis problems over a narrow frequency range. Pure frequency domain techniques are then more appropriate. The MoL has been chosen here, because of its semi-analytical nature in one coordinate direction (i.e. planar transmission line). Since also the MoL is a space discretization technique, discretization errors are a problem. In this thesis, the inherent second order accuracy of the MoL is improved to fourth order and the MoL scheme is extended to cylindrical structures.

The refinements to both methods are original and have been published in refereed journals and conference proceedings.

Examiners:

Dr. R. Vahldieck, Supervisor (Dept. of Elec. and Comp. Eng.)

Dr. J. Bornemann, Departmental Member (Dept. of Elec. and Comp. Eng.)

Dr. L. Kirilin, Departmental Member (Dept. of Elec. and Comp. Eng.)

Dr. N. Djilali, Outside Member (Dept. of Mech. Eng.)

Dr. K. Wu, External Examiner (Ecole Polytechnique de Montreal)

Table of Contents

Table of Contents	iv
List of Tables	viii
List of Figures	ix
Acknowledgments	xiii
1 Introduction	1
1.1 Numerical techniques for CAD of microwave circuits.	1
1.1.1 Necessity of numerical modeling.	1
1.1.2 Efficiency versus versatility of numerical methods.	2
1.2 FDTD method	3
1.2.1 Historic review of FDTD.	3
1.2.2 Principle outline of the FDTD method	5
1.2.3 Convergence and stability	6
1.2.4 Choice of the excitation impulse	7
1.2.5 Solution process	8
1.3 Method of lines	9
1.4 Overview of the thesis	10
2 Full-wave 2D FDTD Method	12
2.1 Introduction	12
2.2 Full-wave 2D FDTD method	14
2.2.1 Theory	14
2.3 Stability criterion and numerical dispersion.	16
2.3.1 Stability criterion	17
2.3.2 Numerical dispersion	18
2.4 Comparison among the 2D FDTD schemes.	18
2.5 Conclusion	19

3	Improvement and extension to FDTD method	20
3.1	Modified FDTD grading algorithm	20
3.1.1	Grading FDTD algorithms	20
3.1.2	Modified variable mesh algorithm	21
3.2	Digital signal processing by Prony's method	25
3.3	Improved ABC for FDTD.	27
3.4	Modelling of lossy structures	29
3.4.1	Attenuation due to lossy dielectric and conductor material.	29
3.5	FDTD modeling of superconductor circuits	30
3.5.1	Signal propagation in superconductor CPW	30
3.5.2	FDTD modeling of superconductors	32
3.5.3	Characterization of anisotropic superconductors.	34
3.6	Numerical results and discussion	34
3.6.1	Analysis of microstrip and CPW with lossy media and finite metalli- zation	47
3.6.2	Analysis of metal-insulator-semiconductor transmission lines	37
3.6.3	Field distribution in superconductor CPW	38
3.6.4	Effect of buffer layers in superconductor transmission lines	40
3.6.5	Superconductor CPW gap resonator	43
3.6.6	Analysis of electrooptic modulator	43
3.6.7	Probe-fed waveguides	45
3.7	Conclusion	47
4	Modified method of lines	48
4.1	Introduction	48
4.2	Method of analysis	50
4.2.1	Discretization of Helmholtz equation	50
4.2.2	Continuity conditions at interfaces	54
4.2.3	Edge condition.	57
4.3	Numerical results	58
5	Cylindrical method of lines	62
5.1	Introduction	62
5.2	Semianalytical solution of Helmholtz equation	63
5.3	Eigenvalue equation of inhomogeneous waveguides	69
5.4	Cutoff frequencies in homogeneous waveguides	70
5.5	Improved accuracy for the cylindrical MoL.	71
5.5.1	Helmholtz equation	71
5.5.2	Field continuity equation	72

5.6	SVD technique	73
5.7	Numerical test	74
5.7.1	Cylindrical microstrip lines	75
5.7.2	Homogeneous waveguide structures	79
5.8	Conclusion and discussion	82
6	Characterization of resonators and cavities using the 3D CMoL	83
6.1	Introduction	83
6.2	Semianalytical solution of Helmholtz equation	84
6.2.1	Inhomogeneous structures	86
6.2.2	Homogeneous cavities	87
6.3	Numerical results	88
6.4	Conclusion	91
7	Analysis of waveguide discontinuities by CMoL	92
7.1	S-Parameter extractions by cavity model	92
7.1.1	Cavity Model	92
7.1.2	Procedure of S-parameter calculation	94
7.2	Hybrid-boundary model for CMoL	95
7.2.1	Introduction	96
7.2.2	Hybrid boundary conditions in CMoL.	96
7.3	Numerical results	100
8	Conclusion and future work	103
	Bibliography	105
	Appendix A Normalized Yee's 3D FDTD scheme	115
	Appendix B Stability criterion and numerical dispersion of 2D FDTD	117
B.1	Real-variable 2D FDTD	117
B.1.1	Stability criterion for the real variable 2D FDTD	117
B.1.2	Numerical dispersion	120
B.2	Complex-variable 2D FDTD	122
B.2.3	Stability	122
B.2.4	Numerical dispersion	123
B.3	Numerical results and discussion	124
B.4	Conclusion	126
	Appendix C Eigenmatrix for homogeneous structures	127

Appendix D Orthogonal transformation matrix for CMoL	129
Appendix E Existence of [T] for both [P] and [Q] in the modified CMoL with $o(h^4)$ accuracy	133
E.1 Modification to Helmholtz equation.	133
E.2 Permutability of [P] and [Q] and existence of [T]	134
E.3 Derivation of matrix [T]	134
E.4 Continuity condition in the CMoL	136
Appendix F Matrix [T] for the modified MoL in Cartesian Coordinates	139
Appendix G $o(h^4)$ accuracy of the MoL discretization in Cartesian coordinates	143
G.1 Discretization of Helmholtz's equation	143
G.2 Discretization of field continuity equation	145
Appendix H TE modes for homogeneous cavities	147

List of Tables

List of Figures

Figure 1.1	A 2-port CPW discontinuity.	5
Figure 1.2	Coplanar waveguide to be solved by MoL.	10
Figure 2.1	A real variable 2D FDTD mesh cell.	16
Figure 3.1	An arbitrary FDTD variable mesh arrangement; solid lines for electric fields, dashed lines for magnetic fields.	21
Figure 3.2	Grading ratio effect on the calculation accuracy and efficiency of planar structures by real-variable FDTD with (2nd order) and without (1st order) modifications. $\epsilon_r=12.9$, $\text{tg}\delta=4\times 10^{-4}$, $\sigma=4.0\times 10^7$, (a) a microstrip line, $d=8\ \mu\text{m}$, $t=4\ \mu\text{m}$, $h=100\ \mu\text{m}$, (b) cpw, $d=8\ \mu\text{m}$, $s=8\ \mu\text{m}$, $a=50\ \mu\text{m}$, $h=200\ \mu\text{m}$.	24
Figure 3.3	A unit FDTD mesh cell with arbitrary variable sizes.	33
Figure 3.4	Comparison for calculation of losses (lossy media and finite metallization) between eq. (3.20) and eq. (3.21), $\sigma=4.1\times 10^7\ \text{S/m}$, $\epsilon_r=12.9$, $\text{tan}\delta=3.0\times 10^{-4}$, (a) a microstrip line, $h=100\ \mu\text{m}$, $f=15\ \text{GHz}$, (b) CPW, $h=500\ \mu\text{m}$, $w=50\ \mu\text{m}$, $w/(w+2S)=0.4$, $f=10\ \text{GHz}$.	35
Figure 3.5	Total losses of a microstrip line, $\epsilon_r=12.9$, $\text{tan}\delta=3.0\times 10^{-4}$, $h=100\ \mu\text{m}$, $\sigma=4.1\times 10^7\ \text{S/m}$, $t=3\ \mu\text{m}$.	36
Figure 3.6	Metallization thickness effects of microstrip lines and conductor backed coplanar line, $f=50\ \text{GHz}$.	36
Figure 3.7	Frequency dependency of attenuation coefficient for GaAs transmission lines, $\epsilon_r=12.9$, $d=8\ \mu\text{m}$, $s=8\ \mu\text{m}$, $a=50\ \mu\text{m}$, $h=200\ \mu\text{m}$.	37
Figure 3.8	Numerical results of 2D FDTD compared to the experiment in [42]; $h=490$, $d=2$, $t=1$, $w=10$, $s=5$, $a=50$, $\epsilon_r=4$, $r=15\ \Omega$, $s=2.75\times 10^7\ \text{S/m}$, all dimensions are in μm .	38
Figure 3.9	Conductor-backed coplanar waveguide, $w=15\ \mu\text{m}$, $s=10\ \mu\text{m}$, $h=100\ \mu\text{m}$, $t=1\ \mu\text{m}$, $\epsilon_r=12.8$, $\text{tg}\delta=4.0\times 10^{-7}$	39
Figure 3.10	Gaussian pulse with width 40 ps in the superconductive CPW line, $t=400\Delta t$.	39

Figure 3.11	Gaussian pulse with width 40 ps in the superconductive CPW line, $t=600\Delta t$.	40
Figure 3.12	Attenuation of a superconductor microstrip line with and without a buffer layer ($\epsilon_r=500$, $d=0.1 \mu\text{m}$), $w=150 \mu\text{m}$, $t=0.5 \mu\text{m}$, $h=500 \mu\text{m}$, $\epsilon_r=9.8$, $\lambda=0.2 \mu\text{m}$, $\sigma_1=1.0 \text{ S}/\mu\text{m}$, $T_c=93 \text{ K}$, $T=77 \text{ K}$, $\lambda_z=5\lambda_{x,y}$	40
Figure 3.13	Propagation Characteristic of a superconductor microstrip line with and without a buffer layer ($\epsilon_r=500$, $d=0.1 \mu\text{m}$), $w=150 \mu\text{m}$, $t=0.5 \mu\text{m}$, $h=500 \mu\text{m}$, $\epsilon_r=9.8$, $\lambda=0.2 \mu\text{m}$, $\sigma_1=1.0 \text{ S}/\mu\text{m}$, $T_c=93 \text{ K}$, $T=77 \text{ K}$, $\lambda_z=5\lambda_{x,y}$	41
Figure 3.14	Attenuation Characteristic of a superconductor CPW with (solid line) and without (dashed line) a buffer layer ($\epsilon_r=500$, $d=0.1 \mu\text{m}$), $w=150 \mu\text{m}$, $s=100\text{mm}$, $t=0.5 \mu\text{m}$, $h=500 \mu\text{m}$, $\epsilon_r=9.8$, $\lambda=0.2 \mu\text{m}$, $\sigma_1=1.0 \text{ S}/\mu\text{m}$, $T_c=93 \text{ K}$, $T=77 \text{ K}$, $\lambda_z=5\lambda_{x,y}$	42
Figure 3.15	Propagation Characteristic of a superconductor CPW with (solid line) and without (dashed line) a buffer layer ($\epsilon_r=500$, $d=0.1 \mu\text{m}$), $w=150 \mu\text{m}$, $s=100\text{mm}$, $t=0.5 \mu\text{m}$, $h=500 \mu\text{m}$, $\epsilon_r=9.8$, $\lambda=0.2 \mu\text{m}$, $\sigma_1=1.0 \text{ S}/\mu\text{m}$, $T_c=93 \text{ K}$, $T=77 \text{ K}$, $\lambda_z=5\lambda_{x,y}$	42
Figure 3.16	CPW gap resonator, $\epsilon_r=9.8$, $\lambda=0.18 \mu\text{m}$, $\sigma_1=1.0 \text{ S}/\mu\text{m}$, $T_c=86 \text{ K}$, $T=80 \text{ K}$, $\lambda_z=5\lambda_{x,y}$, a buffer layer ($\epsilon_r=500$, $d=0.1 \mu\text{m}$), $t=0.5 \mu\text{m}$	43
Figure 3.17	Calculation of propagation characterization of an electrooptic modulator, $s=5\text{mm}$, $w=8\text{mm}$, $a=4\text{mm}$, $b=10\text{mm}$, $c=1\text{mm}$, $d=0\sim 0.4\text{mm}$, $l=5\text{mm}$.	44
Figure 3.18	Cross section of the coaxial fed probe in a rectangular waveguide	46
Figure 3.19	Cross section of the coaxial fed probe in waveguides with loading, all dimensions are in mm, $a=12.5\text{mm}$, $b=3.6\text{mm}$.	46
Figure 3.20	Effect of the probe position L for different probe insertion depth d	47
Figure 4.1	MoL calculation of a microstrip-slot line with two dielectric interfaces A and B, p is the edge parameter to satisfy the edge condition.	55
Figure 4.2	Calculation of a microstrip line, $w=d=1.25\text{mm}$, $a=b=c=12.5\text{mm}$, $\epsilon_r=8.875$, edge parameter $p = 0.30$ (case a), 0.25 (case b).	60
Figure 4.3	Calculation of a microstrip-slot line with tuning septums, $w=d=1.25\text{mm}$, $a=b=c=12.5\text{mm}$, $s=1\text{mm}$, $\epsilon_r=8.875$.	61
Figure 5.1	MoL discretization in a cylindrical coordinate system.	64
Figure 5.2	CMoL discretization for a waveguide with arbitrary contour.	71
Figure 5.3	Evaluation of the lowest singular values of the eigenvalue matrix versus the cutoff frequencies of a cylindrical waveguide, $a=2.54 \text{ cm}$, (a) TM modes, (b) TE modes.	74
Figure 5.4	Convergence test for frequency-dependent properties of the open cylindrical microstrip lines, substrate relative dielectric constant $\epsilon_1 = 9.6$ (alumina), curvilinear coefficient $R = a/b = 0.9$.	75

Figure 5.5	Effective dielectric constant of coupled striplines versus separation angle γ , $d_4/d_1=4$, $d_3/d_1=3$, $d_2/d_1=2$, $\epsilon_1=2$, $\epsilon_2=4$, $\epsilon_3=6$, $\alpha=10.195^\circ$	76
Figure 5.6	Effective dielectric constant of the open multiconductor microstrip lines versus the separation angle γ , της διμενσιών φασ μνλτιλαυερσ: $d_3/d_1 = 3$, $d_2/d_1 = 2$, $\epsilon_1 = 2$, $\epsilon_2 = 4$, $\epsilon_3 = 1$, $\alpha = 10.195^\circ$	76
Figure 5.7	Frequency-dependent effective relative dielectric constant of the open cylindrical microstrip lines, substrate relative dielectric constant $\epsilon_1 = 9.6$ (alumina), Curvilinear coefficient $R = a/b = 0.9$.	77
Figure 5.8	Frequency-dependent characteristic impedance of the open cylindrical microstrip lines, substrate relative dielectric constant $\epsilon_1 = 9.6$ (alumina), Curvilinear coefficient $R = a/b = 0.9$.	77
Figure 5.9	Frequency-dependent properties of the open cylindrical microstrip line, substrate relative permittivity $\epsilon_1 = 9.6$ (alumina), Curvilinear coefficient $R = a/b = 0.9$.	78
Figure 5.10	CMoL results of coupled microstrip lines, $\epsilon_r=9.6$, $w/h=1.0$, $s/h=1.0$, $a/b=0.9$.	78
Figure 5.11	CMoL results for TE_{10} and TM_{11} modes compared to analytical solutions for a rectangular waveguide, $b = a/2 = 3.555$ mm (WR-28).	79
Figure 5.12	CMoL results for TE_{11} and TM_{01} modes compared to analytical solutions for a circular waveguide, $R_0 = 2.54$ cm.	80
Figure 5.13	Normalized cutoff wavenumbers of elliptic waveguides for different axis ratio a/b calculated by MoL and compared to the BEM [72], (a) TE modes, (b) TM modes.	80
Figure 5.14	Effect of the ridges on the cutoff frequencies of the fundamental TE_{11} mode, $r_0 = 2.54$ cm.	81
Figure 5.15	Cutoff frequencies of CRW with fifth ridge, $R_0 = 2.54$ cm, $\theta_1 = 25^\circ$, $\theta_2 = 12.5^\circ$.	82
Figure 6.1	3D MoL discretization in a cylindrical coordinate system	84
Figure 6.2	Resonant frequencies of TE_{111} and TM_{010} modes by 3D cylindrical MoL compared to the analytical solutions for a circular waveguide, $L = R_0 = 2.54$ cm	89
Figure 6.3	Resonant frequencies of TE_{101} and TM_{110} modes by 3D cylindrical MoL compared to the analytical solutions for a rectangular waveguide, $L = b = a/2 = 3.555$ mm	89
Figure 6.4	3D CMoL calculation of resonant frequencies of the TM_{010} mode in a dielectric-loaded ($\epsilon_r=2.2$) circular waveguide cavity; $L = R_0 = 2.5400$ cm, 2.5654 cm, 2.5908 cm	90
Figure 6.5	3D CMoL calculation of Resonant frequencies of TM_{110} mode in a dielectric-loaded ($\epsilon_r=2.2$) rectangular waveguide cavity; $L = b = a/2 = 3.55500$ cm, 3.59055 cm, 3.62610 cm	90

Figure 6.6	Resonant frequencies of a dielectric loaded waveguide cavity, $a = b = L = 2.54$ cm, $R_0 = 1.54$ cm, $r_0 = R_0/2$, $\epsilon_r = 38.5$	91
Figure 7.1	(a) Waveguide short end, and (b) equivalent circuit.	93
Figure 7.2	(a) A 2-port CPW discontinuity, and (b) equivalent circuit.	93
Figure 7.3	Waveguide discontinuities in cylindrical coordinates.	93
Figure 7.4	Coaxial Low-Pass Filter	100
Figure 7.5	Discretization of discontinuity of coaxial line steps and its equivalent circuit	101
Figure 7.6	Capacitance of coaxial line steps versus $\alpha = (r_2 - r_1)/(r_3 - r_1)$	101
Figure 7.7	Circular Waveguide Band-Pass Filter calculated by CMoL.	102
Figure B.1	Effect of the stability factor and the discretization size on the relative error of the complex 2D FDTD [26] calculation of a rectangular waveguide, WR-28 waveguide, $a=7.111$ mm, $b=3.555$ mm, $\epsilon_r=2.2$, $\tan\delta=3.0 \times 10^{-4}$, $\beta=628.0425$, (a) $s=0.50$, (b) $s=0.25$.	125
Figure B.2	Effect of the stability factor and the discretization size on the relative error of the real-variable 2D FDTD calculation of a rectangular waveguide, WR-28 waveguide, $a=7.111$ mm, $b=3.555$ mm, $\epsilon_r=2.2$, $\tan\delta=3.0 \times 10^{-4}$, $\beta=628.0425$, (a) $s=0.5$, (b) $s=0.50$, (c) $s=0.25$, (d) $s=0.125$	126
Figure F.1	MoL calculation of a microstrip line with two dielectric interfaces A and B.	142
Figure G.1	MoL discretization in x-direction.	143

Acknowledgments

I would like to take this opportunity to thank my supervisor, Dr. R. Vahldieck, for his advice during my whole research and study at the University of Victoria. I am grateful to him for his continuous guidance, encouragement and seemingly endless patience throughout the development of this thesis. I am also grateful to him to provide financial support that made it possible to finish my Ph.D program and this thesis in time.

I would also like to thank Dr. J. Bornemann, Dr. L. Kirlin, Dr. N. Djilali, University of Victoria and Dr. K. Wu, Ecole Polytechnique de Montreal, for their suggestions and for serving on my supervisory committee.

Helpful discussions in this thesis with Dr. W.-S. Lu, Dr. K. Wu, and Dr. Z. Cai should be specially acknowledged.

Finally, I would like to thank Ms. Q. Zhang, Ms. U. Balaji, Dr. B. Varaihon de la Filolie, Dr. H. Jin, Mr. S. Chen, Dr. M. Yu, Dr. J. Huang, and all the members of the Laboratory for Lightwave, Electronics, Microwaves, and Communications (LLiMiC) in the Department of Electrical and Computer Engineering, University of Victoria, from whom I got much help.

The Graduate Research Engineering And Technology (GREAT) award from the Science Council of British Columbia during 1992-1995 was highly appreciated.

Chapter 1

Introduction

1.1 Numerical techniques for CAD of microwave circuits

1.1.1 Necessity of numerical modeling

The necessity of numerically modeling electromagnetic fields in microwave components has become more and more evident in recent years. The progress in miniaturizing microwave and millimeter wave integrated circuits has reduced circuit dimensions which are in the order of the wavelength of the operating frequency. As a result, the radiating interaction between circuit sections becomes an important design parameter which, if not accounted for, will lead to discrepancies between theoretical and measured results. Therefore, an accurate CAD procedure is required and aimed at first-run success to maximize circuit yield.

Commercially available software packages like *TouchtoneTM* and *SupercompactTM* are largely based on curve-fitting or empirical formulas. *SonnetTM* is mainly based on full-wave techniques and has set a trend for *TouchtoneTM* and *SupercompactTM* to implement more accurate modeling techniques to make the design more flexible and reliable. The objectives of numerical modeling is the circuit analysis, i.e. determining the characteristics of a specific structure versus frequency or dimension. From the analysis data either synthesis procedures are derived to design a specific component to specifications or use optimization strategies until prescribed performance characteristics are met. In either case the accuracy of the component design depends directly on the accuracy with which the circuit characteristics are derived. Therefore, accurate numerical model-

ing is an integral and important part of modern microwave system design. With this goal in mind, the purpose of this thesis is to examine and improve the two numerical techniques that are considered to be very effective. In the time domain: the time domain finite difference (FDTD) methods; and in the frequency domain: the method of lines (MoL). Both techniques employ space discretization which makes them very flexible.

1.1.2 Efficiency versus versatility of numerical methods

In the presence of dispersion, quasi-static approaches can not very well predict the characteristics of the circuits. Therefore, full-wave numerical methods for modeling microwave integrated circuits have been developed. The mode matching method (MMM), boundary/finite element method (BEM/FEM), method of moment, spectral domain approach (SDA), method of lines (MoL), transmission line matrix method (TLM), and finite difference time domain method (FDTD) are quite well known. These methods are extensively documented in the literature [1].

Each method has its own advantages and disadvantages, and a compromise must often be made between flexibility, CPU time and memory space required. Among these methods, the TLM method and FDTD method are two popular time domain methods. In parallel to the TLM method, the FDTD is one of the most universal techniques for time and frequency domain applications. However, in comparison to the TLM method, the FDTD method needs less memory space and less CPU run time. Also, the FDTD method is straightforward and easy to implement in program. That is why FDTD is chosen in this work instead of TLM. On the other hand, the MoL, a semi-analytical finite difference method, is one of the most efficient methods for frequency domain applications, because as a space discretization method, it requires less computational resources compared to other methods in this class (finite difference method (FD) or FEM). The MoL is especially suitable for layered microwave circuits like microstrip lines and coplanar waveguides (CPW). Therefore, the MoL is another main topic in this thesis. Since the FDTD method and the MoL belong to the class of space discretization techniques, which are the most versatile analysis tools, they are still computationally very demanding for complex microwave structures. To maintain their versatility but at the same time improve their computa-

tional efficiency is the main objective of this thesis.

1.2 FDTD method

1.2.1 Historic review of FDTD

The FDTD method has been widely used for many electromagnetic field problems. The popularity of the method is due to several reasons. Firstly, Maxwell's equations are solved in a sequential manner which makes the algorithm simple and very appropriate for parallel computer operations. Secondly, the method can be applied to problems with complex structures which can be very difficult to solve with either analytical or other numerical methods. Thirdly, the FDTD provides a direct solution for transient problems. Frequency domain methods are very limited for this kind of application, because computations are needed at many frequencies before a Fourier transform can be applied to obtain the transient response with sufficient accuracy. The impulse response from the FDTD method contains the frequency domain information over the entire spectrum, but only one computation run is needed. Fourthly, the FDTD can be applied to solve such complex problems as inhomogeneous, lossy, nonlinear, anisotropic, and random time-varying media etc. Most other approaches can not treat such a variety of problems within the frame work of one method. Especially for nonlinear and time-varying media, frequency domain methods are limited.

Although the many attractive features of the FDTD method have made this numerical technique a subject of numerous research papers, the main disadvantage of the FDTD method is still its requirement for large computer memory space and long CPU time which both increase with the complexity of the problem. This can only be overcome by either using supercomputers (or parallel processors) or improving the method itself. The latter point is addressed in this thesis by introducing a two dimensional (2D) hybrid FDTD method with a variable mesh size of second order accuracy, improving the absorbing boundary conditions and using signal processing techniques to accelerate the FDTD algorithm.

Since the first paper on the FDTD by Yee [2] in 1966, great efforts have been

made to apply the method and improve its efficiency [3]-[41]. Recent research mainly concentrates on reducing computational overhead. An outstanding topic is the accurate termination of guided wave structures extending beyond the FDTD grid boundaries. The key difficulty is that the propagation in a waveguide can be multimodal and dispersive, and absorbing boundary conditions (ABC) utilized to terminate the waveguide must be able to absorb energy having widely varying transverse distributions and group velocities v_g .

Typical FDTD ABC's developed for free space problems include the space-time extrapolation method [3], the one-way wave equations [4], the impedance boundary condition [5], Engquist & Majda's [6], Liao et. al's [7] and Higdon's method [8], and the super-absorbing method [9]. However, when applied to terminate guided wave structures, such ABC's perform best only for narrowband energy of propagation modes where v_g is well defined. Some researchers have tried to account for variations of the waveguide modal v_g with frequency [16]. But these algorithms are global in time requiring the evaluation of a convolution integral for each mode, thus resulting in inefficient calculations.

One of the most recent contributions to the FDTD method which, in its importance could be ranked right after Yee's original work, is presented by Berenger's perfectly matched layer (PML) technique which reduces reflections from the absorbing boundary conditions [10]. This work was extended to 3D problems [12]. But, in applying this technique, many layers (typically 10-20) are required to achieve a high resolution of frequency domain parameters such as S-parameters and wave propagation constant. This leads to a noticeable increase of CPU time. Previously used absorbing boundary conditions fail when fields near outer boundaries are mostly evanescent waves instead of outgoing waves. As a result, in FDTD modeling of microwave integrated circuits (taking an open microstrip line or CPW as an example) outer boundaries parallel to the microstrip line or CPW have to be placed far away from the metal strip in order to minimize the influence of reflected waves from these boundaries. It has been observed that even a modest amount of error in transient solutions, caused by the reflection from the outer bound-

aries, can severely deteriorate the accuracy of frequency-dependent circuit parameters obtained through a Fourier transform of the transient solution [13]. To ensure accurate numerical results without requiring excessive computer resources, the absorbing boundary must absorb both outgoing propagating and evanescent waves. This topic will be discussed in Chapter 3.

1.2.2 Principle outline of the FDTD method

To illustrate the method a conductor-backed coplanar waveguide (CPW) discontinuity (Figure 1.1), is used. The bottom plane and strip are made of perfect conductors, and the structure is assumed to extend infinitely above the metal strip plane, as well as the horizontal plane.

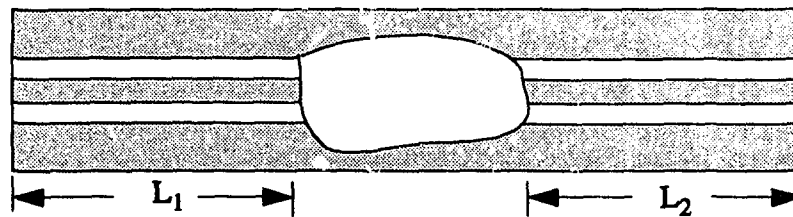


Figure 1.1 A 2-port CPW discontinuity.

Maxwell's curl equations are

$$\frac{\partial \vec{E}}{\partial t} = \frac{1}{\epsilon} \nabla \times \vec{H}, \quad \frac{\partial \vec{H}}{\partial t} = -\frac{1}{\mu} \nabla \times \vec{E}, \quad (1.1)$$

with ϵ and μ as material parameters. For uniqueness of the solution of Maxwell's equations, the following conditions must be satisfied:

- (a) The initial condition at $t=t_0$ for the fields must be given over the entire domain of interest.
- (b) The tangential field components at the boundary must be given for $t>t_0$. For the boundary at infinity, Sommerfeld's radiating condition must be satisfied, that is, the wave at infinity must be of an outgoing type.

There are many ways to solve the system of Maxwell's equation. The FDTD arranges the discrete nodal points as in Figure 3.3 on page 46. The whole computation domain is discretized by those cells. It follows from eq. (1.1) that every electric field component can be obtained from the loop integral of four magnetic field components. Similarly, the magnetic field is obtained from the electric fields. In this algorithm, not only the placement of electric and magnetic nodes are offset in space by a 0.5 space step, but also the time steps are offset by a 0.5 time step. To be more specific, if the components of E are calculated at $n\Delta t$, where Δt is the discretization unit in time, or the time step, and n is any non-negative integer, then the components of H are calculated at $(n+0.5)\Delta t$. For this reason, this staggered process is also called leap-frog algorithm.

For a source-free and inhomogeneous region of space, Maxwell's equation leads to the following expression (taking the E_x component as an example, other field components can be given in a similar form):

$$E_x^{n+1}(i, j, k) = E_x^n(i, j, k) + \frac{\Delta t}{\epsilon} \left(\frac{H_z^{n+0.5}(i, j, k) - H_z^{n+0.5}(i, j-1, k)}{\Delta y} - \frac{H_y^{n+0.5}(i, j, k) - H_y^{n+0.5}(i, j, k-1)}{\Delta z} \right), \quad (1.2)$$

with Δx , Δy , and Δz being the space discretization units in x , y , and z direction respectively, and Δt is the time discretization interval. Knowing the initial and boundary conditions, the time-dependent fields can be calculated in a leap-frog time-marching process using the above equation.

1.2.3 Convergence and stability

The convergence and stability of the algorithm are a major concern. The FDTD algorithm is based on the linear hyperbolic differential equations, to prove that the FDTD algorithm converges is equivalent to the proof for simultaneously satisfying the consistency and stability conditions.

The consistency condition states that when the discretization interval approaches

zero, also the local truncation error approaches zero on all the mesh points. The discretized system is said to be consistent with the original differential system. The staggering FDTD scheme satisfies the consistency condition. The proof is easily shown in that the local truncation error of the scheme is of a second order $o(\Delta h^2)$ and $o(\Delta t^2)$. This is an advantage of the FDTD because the central finite difference scheme in both time and space ensures that the local truncation error is of second order in both domains, however, only if a uniform mesh is used.

The stability condition requires that the numerical errors, which are generated in one step of the calculation, do not increase from step to step as the computation goes on. The stability criterion of the FDTD determines the choices of the time and space steps, that is [3]

$$v\Delta t \leq \left(\Delta x^{-2} + \Delta y^{-2} + \Delta z^{-2} \right)^{-1/2}. \quad (1.3)$$

For the special case of $\Delta x = \Delta y = \Delta z = \Delta h$, the above equation becomes $v\Delta t \leq \Delta h / \sqrt{3}$, which shows that the time step must be chosen much smaller than the space steps.

1.2.4 Choice of the excitation impulse

The selection of the excitation impulse is a practical issue and mainly depends on the individual structure to be analyzed and the frequency band needed. An impulse propagating along the structure must contain the spectrum of interest. The excitation impulse used for microstrip lines and CPW has been chosen to be Gaussian in shape, because it has a smooth waveform in time, and its Fourier transform is also a Gaussian distribution centered at zero frequency. Appropriate choice of the Gaussian impulse width will give the frequency-dependent parameters we want. An ideal Gaussian impulse which propagates in the +z direction will have the following expression

$$g(z, t) = \exp \left[- \left(t - t_0 - (z - z_0) / v \right)^2 / T^2 \right], \quad (1.4)$$

where v is the velocity of the pulse in a specific media. The impulse has its maximum at $z=z_0$ when $t=t_0$. The Fourier transform of the above Gaussian impulse has the form

$$G(f) = \exp\{-(\pi T f)^2\}. \quad (1.5)$$

The choice of the parameter T , t_0 and z_0 are subject to the following requirements:

- (A) After the space discretization step Δz and the time interval Δt have been chosen according to the stability criterion, the Gaussian impulse must contain enough space divisions so as to be well represented by its discretized form. We define an impulse width w as the width between the two symmetric points which have approximately 5% of the maximum values of the impulse. Therefore,

$$\exp\{-(w/2)^2 / (vT)^2\} = \exp(-3) \approx 5\%. \quad (1.6)$$

When the width w is chosen around 20 space steps, T is determined by

$$T = 10\Delta z / v\sqrt{3}. \quad (1.7)$$

- (B) For a chosen T , the maximum frequency ($G(f_{\max})=0.1$) that can be calculated is

$$f_{\max} = 1 / (2T) = 0.05\sqrt{3}v / \Delta z. \quad (1.8)$$

1.2.5 Solution process

The FDTD applications for various microwave integrated circuits can be summarized as follows:

- (A) Place the structure to be analyzed into a computation volume.
- (B) Fill the computation space with FDTD meshes.
- (C) Truncate the computation space with reflection-free walls to simulate an infinite space.
- (D) Excite the structure at one transversal plane over a period of time with an impulse whose width is chosen to cover the frequency bandwidth of interest.
- (E) Switch on the leap-frog FDTD explicit process and observe the transient wave form in the time domain at a proper location.
- (F) Extract the frequency parameters by using the Fourier transform.

1.3 Method of lines

Although the method of lines was proposed to solve partial differential equations back in the 60s, the application of this method to the microwave area was first proposed in the 80s. In this method, one or two space variables are discretized for numerical processing while analytical expressions are sought for the remaining space variable. Considering a CPW transmission line as an example (Fig. 1.2), first, the x direction is discretized by a family of N straight lines parallel to the y axis and separated by h . When the partial derivatives with respect to the x coordinate are replaced with finite differences, the electric and magnetic potentials, ψ^e and ψ^h , satisfy the discretized wave equation

$$\frac{d^2 \psi_i}{dy^2} + \frac{1}{h^2} [\psi_{i-1} - 2\psi_i + \psi_{i+1}] + (k^2 - \beta^2) \psi_i = 0, \quad i=1,2,3,\dots,N, \quad (1.9)$$

or in matrix form

$$h^2 \frac{d^2 \bar{\Psi}}{dy^2} - \{ [P] - h^2 (k^2 - \beta^2) [I] \} \bar{\Psi} = 0, \quad (1.10)$$

where I is the identity matrix and $[P]$ is a tridiagonal matrix determined by the lateral boundary conditions at $x=0$ and $x=a/2$. The ψ^e and ψ^h are shifted by half the discretization distance, $h/2$, so that the lateral boundary conditions are easily implemented and the approximation of partial derivatives by finite differences has a second order accuracy, both for ψ^e and ψ^h simultaneously. The main advantage of the method lies in the decoupling procedure of the above equation (1.10) through diagonalization of the matrix $[P]$, so that the equation for ψ^e and ψ^h can be solved independently and analytically for each discretization point i . This is accomplished by an orthogonal transformation $[T] \bar{\Psi} = \bar{U}$, where $[T]^t$ denotes the transpose of an orthogonal matrix $[T]$ determined by the lateral boundary conditions. Then the uncoupled equations take the following form

$$h^2 \frac{d^2 U_i}{dy^2} + \{ \lambda_i - h^2 (k^2 - \beta^2) \} U_i = 0, \quad i=1,2,3,\dots,N, \quad (1.11)$$

with λ_i being the eigenvalue of $[P]$. After the above equations are solved analytically, boundary conditions and field continuity at the interfaces between different uniform regions may be imposed. Finally, the condition that the tangential electric fields on a metal strip or current density in a dielectric interface must vanish is imposed in the original domain, and the following matrix equation is derived

$$[A] \begin{bmatrix} J_x \\ J_z \end{bmatrix} = \begin{bmatrix} 0 \\ 0 \end{bmatrix}, \quad (1.12)$$

where J_x and J_z are the current vectors. The non-trivial solution requires that the determinant of eigenvalue matrix $[A]$ vanish.

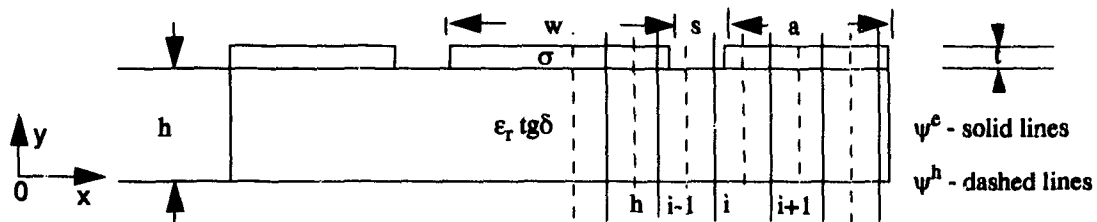


Figure 1.2 Coplanar waveguide to be solved by MoL.

Then the transmission parameters can be determined and from these also the fields and currents.

The method can be extended to three dimensional problems such as microstrip resonators and antennas.

1.4 Overview of the thesis

FDTD is one of the most popular, powerful, and universal techniques. However, the MoL, a semi-analytical technique, is one of the numerically most efficient methods. The common feature of FDTD and MoL is that both of them are space discretization techniques. MoL is in the frequency domain. FDTD is in time domain. Chapter 1 reviews these two techniques, which will be further developed in the following chapters.

Chapter 2 outlines new improvements to the FDTD algorithm developed in this

thesis. First the 2D FDTD method which improves the computational efficiency of the method significantly, especially for frequency-selective applications. The scheme is further improved by introducing real-variables in the FDTD process.

In chapter 3, a variable grading scheme that preserves second order accuracy is presented to further improve the efficiency and accuracy of the FDTD. Extending the variable grading scheme to 3D and combining it with Prony's spectrum estimation technique and improved ABC, the efficiency and accuracy of the FDTD is further improved. To validate the improvements, the method is applied to simulate waveguide discontinuities, superconductors, lossy structures considering lossy media and finite but thin metallization thickness.

In Chapter 4, the MoL is modified to provide 4th order accuracy. The continuity condition and edge condition are included in this new scheme to provide an overall error reduction. As a result, the new MoL algorithm has significantly improved accuracy and is computationally much more efficient.

In chapter 5, the cylindrical MoL (CMoL) is proposed for the general case of asymmetric cylindrical structures. It will be shown that the new algorithm is suitable to analyze complex structures with mixed coordinate systems. The method can handle static problems as well by solving Poisson's equation.

In Chapter 6, the CMoL is extended to 3D analysis. A class of homogeneous and inhomogeneous cavities and resonators with mixed coordinates are analyzed.

Chapter 7 briefly introduces the cavity model and discusses problems with inhomogeneous boundary conditions to calculate S-parameters of 3D circuits by the CMoL.

Chapter 8 concludes this thesis.

Chapter 2

Full-wave 2D FDTD Method

2.1 Introduction

When Yee in 1966 [2] introduced the FDTD method, he discretized Maxwell's equations directly by the central finite differences in time and space. Since then the FDTD has been further developed and is now well established as a versatile technique to solve electromagnetic field problems. The method is in particular attractive for transmission line problems with complicated circuit contours. Application examples have been reported in i.e. [3-13]. Although the method has many attractive features for time domain problems, one commonly known disadvantage of the FDTD method for frequency selective analysis problems is that it requires large amounts of memory space and CPU time, in particular for the full wave analysis of hybrid modes in quasi-planar circuits or in general in inhomogeneous waveguide structures. The large memory space and CPU time requirements in the FDTD method are mainly due to the fact that processing a time domain impulse involves from the start much more frequency information than what is actually needed for the circuit analysis and that a full wave analysis requires a three-dimensional mesh. Only after the impulse has reached stability in the three-dimensional mesh, a Fourier transform can be applied to select the information of interest. Up to now a two-dimensional mesh could only be used to calculate the special case of TM or TE modes separately [2]. Although several slightly different approaches for the FDTD have been reported, all of them require a three-dimensional mesh to determine hybrid modes. For example, one of those methods uses a Gaussian pulse as excitation for a single shielded microstrip line [15]. Typically 160

space meshes are required in propagation direction and about 5 to 7 time steps for any one mesh to satisfy the stability condition. Another approach is to resonate a section of the guided structure by placing two short-circuited planes along the z-axis a distance L apart. The length L corresponds to half a guided wavelength of the mode of interest. The resonance frequency of the cavity corresponds to the frequency at which this particular propagation constant is valid. The relationship between the propagation constant and L is then $\beta=2\pi/L$. By changing L also β changes. Repeating the calculation of the resonant frequency of the resonator for each β the dispersion characteristic of the guided structure can be obtained [14]. Since also this method involves a three dimensional mesh, there are easily thousands of iteration steps involved.

To alleviate these problems, this chapter introduces a novel approach for the FDTD which uses only a two-dimensional mesh consisting of a three-dimensional space grid for the analysis of hybrid modes. This two-dimensional mesh could also be regarded as one slice out of a three-dimensional mesh, with the third dimension, the propagation direction, being replaced by introducing a phase shift. The idea was first introduced for the TLM method in [23,24]. This step even allows to reduce the size of the space grid to only half of its normal size. At a first glance, the introduction of a phase shift in the time domain algorithm seems to be an odd approach. However, by choosing the propagation constant and then exciting the system with a time domain pulse provides correct results (after a Fourier transform) only at the frequency at which this propagation constant is valid. This step must then be repeated for different propagation constants to obtain the frequency behavior for that particular mode. Since this approach requires only a two-dimensional mesh with a half-size space grid and since the propagation constant is given as an input parameter, the convergence rate is much faster than in the conventional approach. Also the memory space is reduced significantly.

In this chapter, the principle steps for the frequency selective 2D FDTD method will be discussed.

2.2 Full-wave 2D FDTD method

2.2.1 Theory

The basic idea for the new 2D FDTD algorithm is to replace the space discretization in propagation direction (z) by the phase shift. The new approach follows also the two-step leapfrog FDTD procedure initially developed for a full size three-dimensional grid (eq.(A.3)-(A.8)). Due to the introduction of the mode concept, the variables in the 2D FDTD process becomes complex. However, it is found that the complex process can be avoided if a simple functional transform is performed. Furthermore, a truly 2D grid can be obtained if the mesh size in the propagation direction is approaching zero as shown in Fig. 2.1.

Assume the structures are homogeneous along the mode propagation direction (z -axis). A phase delay is involved along the line. Assume

$$E_x, E_y, H_z = j \{E_x, E_y, H_z\} \exp \{-j\beta z\} \quad (2.1)$$

$$H_x, H_y, E_z = \{H_x, H_y, E_z\} \exp \{-j\beta z\}, \quad (2.2)$$

the discretized Maxwell's equations yield:

$$H_x^{n+0.5}\left(i + \frac{1}{2}, k\right) = H_x^{n-0.5}\left(i + \frac{1}{2}, k\right) - \frac{\Delta t}{\mu} \left(\frac{E_z^n\left(i + \frac{1}{2}, k + \frac{1}{2}\right) - E_z^n\left(i + \frac{1}{2}, k - \frac{1}{2}\right)}{\Delta y} - \beta E_y^n\left(i + \frac{1}{2}, k\right) \right), \quad (2.3)$$

$$H_y^{n+0.5}\left(i, k + \frac{1}{2}\right) = H_y^{n-0.5}\left(i, k + \frac{1}{2}\right) - \frac{\Delta t}{\mu} \left(\beta E_x^n\left(i, k + \frac{1}{2}\right) - \frac{E_z^n\left(i + \frac{1}{2}, k + \frac{1}{2}\right) - E_z^n\left(i - \frac{1}{2}, k + \frac{1}{2}\right)}{\Delta x} \right), \quad (2.4)$$

$$H_z^{n+0.5}(i, k) = H_z^{n-0.5}(i, k) - \frac{\Delta t}{\mu} \left(\frac{E_y^n\left(i + \frac{1}{2}, k\right) - E_y^n\left(i - \frac{1}{2}, k\right)}{\Delta x} - \frac{E_x^n\left(i, k + \frac{1}{2}\right) - E_x^n\left(i, k - \frac{1}{2}\right)}{\Delta y} \right), \quad (2.5)$$

$$E_x^{n+1}\left(i, k + \frac{1}{2}\right) = E_x^n\left(i, k + \frac{1}{2}\right) + \frac{\Delta t}{\epsilon} \left(\frac{H_z^{n+0.5}(i, k+1) - H_z^{n+0.5}(i, k)}{\Delta y} + \beta H_y^{n+0.5}\left(i, k + \frac{1}{2}\right) \right), \quad (2.6)$$

$$E_y^{n+1}\left(i + \frac{1}{2}, k\right) = E_y^n\left(i + \frac{1}{2}, k\right) + \frac{\Delta t}{\epsilon} \left(\frac{H_z^{n+0.5}(i, k) - H_z^{n+0.5}(i+1, k)}{\Delta x} - \beta H_x^{n+0.5}\left(i + \frac{1}{2}, k\right) \right), \quad (2.7)$$

$$E_z^{n+1}\left(i + \frac{1}{2}, k + \frac{1}{2}\right) = E_z^n\left(i + \frac{1}{2}, k + \frac{1}{2}\right) + \frac{\Delta t}{\epsilon} \left(\frac{H_y^{n+0.5}\left(i + 1, k + \frac{1}{2}\right) - H_y^{n+0.5}\left(i, k + \frac{1}{2}\right)}{\Delta x} - \frac{H_x^{n+0.5}\left(i + \frac{1}{2}, k + 1\right) - H_x^{n+0.5}\left(i + \frac{1}{2}, k\right)}{\Delta y} \right), \quad (2.8)$$

From the above equations, it is obvious that now only a two-dimensional real-variable process is involved. In other words, only a 2-D iteration process along the x- and y-axis is used leading to much faster convergence than for the conventional 3-D one [2,14,15].

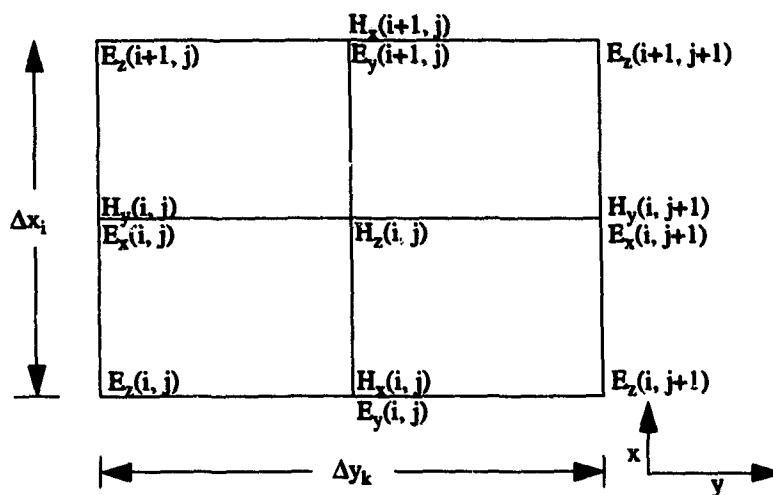


Figure 2.1 A real variable 2D FDTD mesh cell

2.3 Stability criterion and numerical dispersion

Numerical dispersion and stability are two basic but very important issues for the FDTD method because the FDTD involves finite difference approximations and the scheme is explicit. Lack of a rigorous analysis of these two issues will limit the effective application of the method due to the following reasons. First, the stability criterion determines a rule of selecting the time step size which must be small enough to guarantee that the numerical errors do not accumulate during the process. On the other hand, in practical applications, the time step is desired as big as possible to speed up the process. Therefore, a rigorous derivation of the stability criterion is important in choosing the time and space discretization steps. The second issue in this regard is the numerical dispersion. The numerical discretization of Maxwell's equations produces numerical dispersion which means that the phase velocity is a function of the mesh size. Therefore it is different from the physical dispersion. This effect must be reduced as much as possible in simulation of guided wave structures. The dispersion relation shows that the numerical dispersion is related to the stability factor. However any value satisfying the stability condition inequality can be used in the calculation. A stability factor of 0.5 (uniform discretization) is usually used for FDTD modeling without solid supporting reason. Kim & Hofer [28-30]

studied the relation between numerical dispersion and stability factor for the conventional 3D FDTD. For the full wave 2D FDTD methods, detailed discussion will be provided in the Appendix B.

2.3.1 Stability criterion

Assume that the electric and magnetic field components will have a form of where $P = E$ or H ; n ($n=1,2,3,\dots,M$), i ($i=1,2,3,\dots,M$) and k ($k=1,2,3,\dots,N$) are, respectively, where $P = E$ or H ; n ($n=1,2,3,\dots,M$), i ($i=1,2,3,\dots,M$) and k ($k=1,2,3,\dots,N$) are, respectively, the time and space discretization indexes; k_x and k_y are wave numbers, respectively, along the x - and y -directions. Δt , Δx , and Δy are the time and space discretization steps respectively.

We normalize the electric and magnetic fields by using the wave impedance $\eta = \sqrt{\mu/\epsilon}$

$$\vec{E} \rightarrow \vec{E}/\sqrt{\eta}; \vec{H} \rightarrow \vec{H} \times \sqrt{\eta}, \quad (2.10)$$

and the stability criterion is obtained as (Appendix B)

$$v\Delta t \leq \frac{1}{\sqrt{\left(\frac{1}{\Delta x}\right)^2 + \left(\frac{1}{\Delta y}\right)^2 + \left(\frac{\beta}{2}\right)^2}}, \quad (2.11)$$

For the 2D FDTD scheme with complex variables, we obtain the stability condition that is exactly the same as that in (2.11).

As mentioned in Section 2.1 on page 25, the standard 2D FDTD for cutoff characteristics for TE or TM modes [2] is different from the full wave 2D FDTD methods in this thesis. The former one can solve only TE or TM modes separately, but the later one can also analyze hybrid modes in inhomogeneous guided waves. In comparison to the full wave 2D FDTD methods in this thesis, the stability condition of the standard 2D FDTD method in [2] is shown as follows

$$v\Delta t \leq \frac{1}{\sqrt{\left(\frac{1}{\Delta x}\right)^2 + \left(\frac{1}{\Delta y}\right)^2}}. \quad (2.12)$$

Therefore, we found that the real-variable 2D FDTD scheme and the complex one have the same stability condition which is different from the standard 2D FDTD method. However, the real variable 2D FDTD process saves half computer memory space requirement and converges much faster than the complex one.

2.3.2 Numerical dispersion

The numerical dispersion relation for the real variable 2-D FDTD method is as follows (Appendix B)

$$\left(\sin \frac{\omega\Delta t}{2}\right)^2 = \left(\frac{v\Delta t}{\Delta x} \sin \frac{k_x\Delta x}{2}\right)^2 + \left(\frac{v\Delta t}{\Delta y} \sin \frac{k_y\Delta y}{2}\right)^2 + \left(\frac{v\Delta t\beta}{2}\right)^2, \quad (2.13)$$

The numerical dispersion for the complex scheme has the same form as that in (2.13). The numerical dispersion for the standard 2D FDTD scheme has a form as

$$\left(\sin \frac{\omega\Delta t}{2}\right)^2 = \left(\frac{v\Delta t}{\Delta x} \sin \frac{k_x\Delta x}{2}\right)^2 + \left(\frac{v\Delta t}{\Delta y} \sin \frac{k_y\Delta y}{2}\right)^2. \quad (2.14)$$

In all cases, when $\Delta x = \Delta y = \Delta t = 0$, we will have

$$\omega^2 = v^2 (k_x^2 + k_y^2 + \beta^2), \quad (2.15)$$

which corresponds to the dispersion relation for fields in real physical space.

2.4 Comparison among the 2D FDTD schemes

The stability condition in standard 2D FDTD is $v\Delta t/h \leq 1/\sqrt{2}$ when using a uniform space discretization $\Delta x = \Delta y = h$. However, a limiting case of $\Delta z \rightarrow 0$ for the full wave 2D FDTD requires $v\Delta t/h \leq 1/\sqrt{2 + (\beta h/2)^2}$. This holds also for the real variable 2D FDTD. We make a brief comparison as follows

(1) All the new 2D FDTD full-wave methods have different stability conditions and

dispersion relations from the standard 2D FDTD.

(2) The real-variable 2-D FDTD scheme has the same stability condition and dispersion relation as that in the complex one. However, the real variable 2D FDTD process saves at least half computer memory space requirement and converges much faster than the complex one.

Detailed derivations and discussions of the stability conditions and dispersion relations for these 2D FDTD methods are provided in Appendix B.

2.5 Conclusion

A full-wave 2D FDTD methods have been presented and studied. The stability and dispersion of these methods are investigated and discussed.

Chapter 3

Improvement and extension to FDTD method

3.1 Modified FDTD grading algorithm

3.1.1 Grading FDTD algorithms

The computation efficiency of the uniform FDTD mesh deteriorates rapidly with smaller mesh size. In order to resolve circuits with large dimension ratio, for instance, inhomogeneous quasi-planar circuits with thin finite metallization thickness and thick substrate, a grading scheme is necessary. Efforts to find a suitable grading scheme have been published in [38-40]. The common feature of the work in [38-40] is that the mesh size is regionally constant and that time and space interpolations are used. A lattice that is continuously varying in all three space directions and also exhibits second order accuracy has not been reported. The option to use a variable lattice size with fine space resolution around metal corners where field changes are significant, and to use a continuously growing lattice size with greater distance from that corner is very desirable since it leads to better computational accuracy with less computer memory and CPU time. The problems with the schemes reported in the literature so far are that the remaining discretization error is always of first order. With increasing mesh ratio, this leads to a large time domain error. As a consequence, increasing time domain errors lead also to greater frequency domain errors. Therefore, in the following this thesis is concerned with a graded lattice scheme which can be continuously adjusted along any space direction with arbitrary lattice ratio. The ratio needs not to be an integer number. The contribution here is that a second order accuracy is maintained by eliminating the first order errors without the use of additional wave equations or space interpolations as necessary in other approaches.

3.1.2 Modified variable mesh algorithm

Let us first consider the graded mesh shown in Fig. 3.1. The discretization steps along the x - and y -directions are all variable with mesh sizes $\Delta x_i = p_i \Delta h$ and $\Delta y_k = q_k \Delta h$ (Fig. 3.1), where the mesh parameters p_i ($i=1, 2, 3, \dots, M$) and q_k ($k=1, 2, 3, \dots, N$) are positive real numbers as required to resolve the specific structure. M, N are, respectively, the total mesh numbers along the x - and y -directions. If $p_i = \text{constant}$ ($i=1, 2, 3, \dots, M$), $q_k = \text{constant}$ ($k=1, 2, 3, \dots, N$), the variable lattice will be a rectangular one. If all mesh parameters are set to unity, the lattice will be reduced to be a uniform one. Before we develop the algorithm with second order accuracy, let's first look at the problem of the first order error in the variable lattice scheme. Using the E_y -field at the boundary of two neighboring lattices in the FDTD as an example

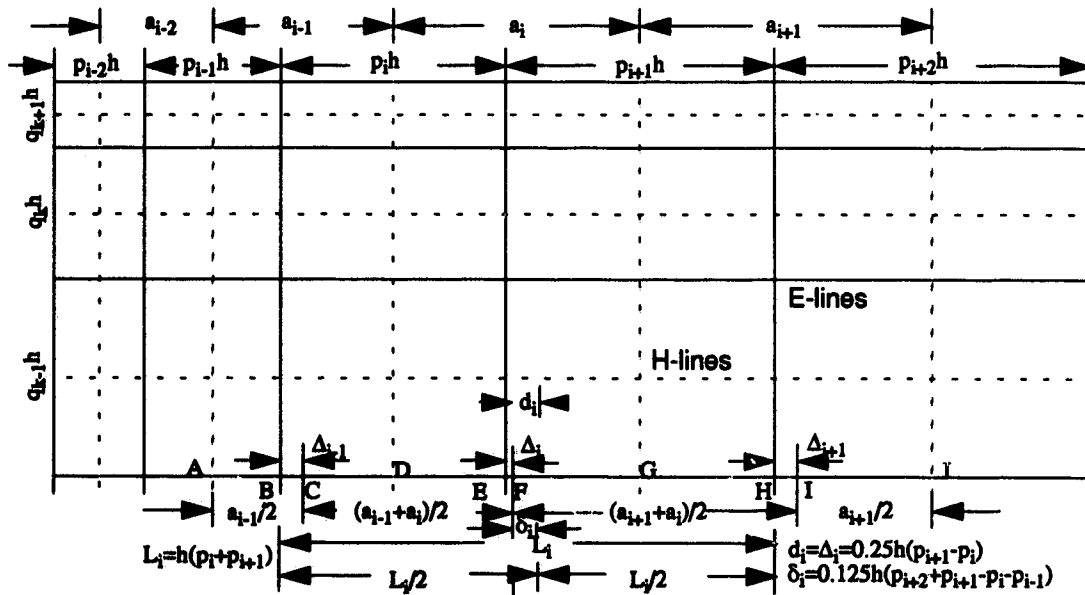


Figure 3.1 An arbitrary FDTD variable mesh arrangement; solid lines for electric fields, dashed lines for magnetic fields.

$$E_y^{n+1}\left(i, k + \frac{1}{2}\right) = E_y^n\left(i, k + \frac{1}{2}\right) + \frac{\Delta t}{\epsilon} \left(\frac{\partial H_z^{n+0.5}(i, k)}{\partial x} - \beta H_x^{n+0.5}\left(i, k + \frac{1}{2}\right) \right), \quad (3.1)$$

we find that by developing the x -dependent term in this equation by a Taylor series yields:

$$\frac{\partial H_z^{n+0.5}(i, k)}{\partial x} = \frac{H_z^{n+0.5}(i+1, k) - H_z^{n+0.5}(i, k)}{\Delta h (p_{i+1} + p_i) / 2} + o((p_{i+1} - p_i) \Delta h) \quad (3.2)$$

Similarly, we can analyze other field components. It is obvious to see from eq. (3.2) that normally a variable grading scheme provides only a first order accuracy. In the following it is shown that a second order accuracy can be obtained for any non-integer lattice ratios by combining the three neighboring lattice cells. The one dimensional case will be treated as an example without loss of generality. The 2-D or 3-D case can be easily extended from this analysis.

It is obvious from an arbitrary mesh arrangement in Fig. 3.1, that the magnetic field components at point A, point D, point G, and point I can be always arranged in the middle of the electric field components. For example, in Fig. 3.1, point D is always at the center between point B and point E; G is at the center between E and H. Therefore, calculating the magnetic field components at D and G from the electric field components at B, E, and H provides automatically a second order accuracy since the central finite difference is maintained. The problem arises when we calculate the E-field from the H-field. Let's consider the E-field at point E as example, which is not located in the middle between D and G. In this case, calculating the E-field from the H-fields leads to a first order error as shown in eq. (3.2). Examining eq. (3.2), we found, however, that a compensation factor can always be found to cancel the first order error term leaving only a second order term. To find this compensation factor three neighboring lattice cells must be used. In other words, a second order accuracy can be obtained by combining neighboring field lattices through a series expansion. To illustrate this procedure, consider the central finite difference scheme to calculate the electric field component from the magnetic field components at points D and G. The result is the point F in the middle between points D and G. Point F is Δ_1 away from point E, which is the electric field node in the variable mesh. Applying a Taylor series analysis the electric field at point F can be given as:

$$E_y^{\Delta_1}(i) = \frac{H_z(i+1) - H_z(i)}{(p_i + p_{i-1}) h / 2} + o(h^2). \quad (3.3)$$

Similarly for other electric field components at points in the middle of magnetic nodes. For instance, $E_y^{\Delta_{i+1}}(i+1)$ at point I and $E_y^{\Delta_{i-1}}(i-1)$ at point C are, respectively, Δ_{i+1} and Δ_{i-1} away from the electric nodes $E_y(i+1)$ and $E_y(i-1)$. The dimension parameters Δ_{i+1} , Δ_i and Δ_{i-1} shown in Fig. 3.1 can be expressed as

$$\Delta_r = \frac{h}{4} (p_{r+1} - p_r), \quad r=i-1, i, i+1. \quad (3.4)$$

Developing the electric field component $E_y(i)$ at the electric node E from the electric field $E_y^{\Delta_i}(i)$ at point F in Fig. 3.1 in a Taylor series yields

$$E_y(i) = E_y^{\Delta_i}(i) + \Delta_i \frac{\partial E_y^{\Delta_i}(i)}{\partial x} + o(h^2). \quad (3.5)$$

This shows a first order partial differential term which can be expressed by using the first order partial differential expansion at the electric nodes as follows

$$\frac{\partial E_y^{\Delta_i}(i)}{\partial x} = \frac{\partial E_y^{d_i}(i)}{\partial x} + d_i \frac{\partial^2 E_y^{d_i}(i)}{\partial x^2} + o(h^2), \quad (3.6)$$

or

$$\frac{\partial E_y^{\Delta_i}(i)}{\partial x} = \frac{E_y(i+1) - E_y(i-1)}{L_i} + \left(d_i \frac{\partial^2 E_y^{d_i}(i)}{\partial x^2} + o(h^2) \right). \quad (3.7)$$

Therefore, the electric field component $E_y(i)$ at the electric node E can be obtained with second order accuracy by including neighboring field components $E_y(i+1)$ and $E_y(i-1)$ as

$$E_y(i) = E_y^{\Delta_i}(i) + \Delta_i \left(\frac{E_y(i+1) - E_y(i-1)}{L_i} \right) + o(h^2) \quad (3.8)$$

due to $\Delta_i d_i = (\Delta_i)^2 = o(h^2)$.

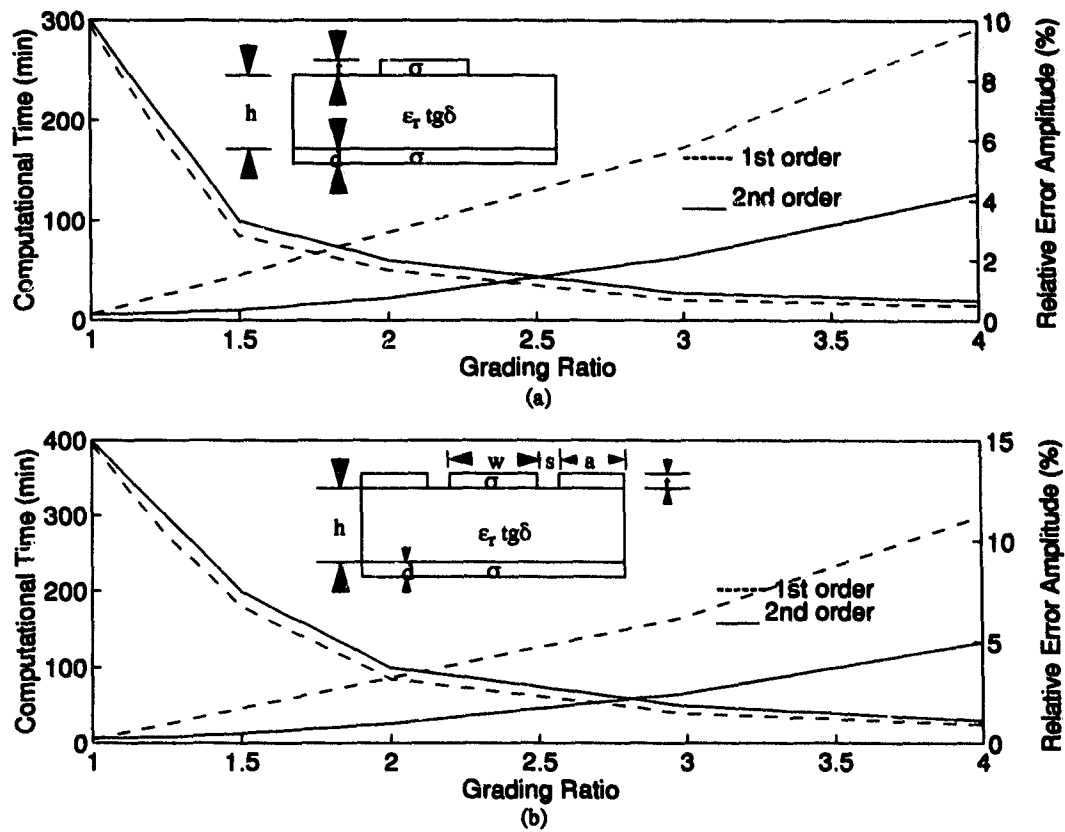


Figure 3.2 Grading ratio effect on the calculation accuracy and efficiency of planar structures by real-variable FDTD with (2nd order) and without (1st order) modifications. $\epsilon_r=12.9$, $tg\delta=4 \times 10^{-4}$, $\sigma=4.0 \times 10^7$, (a) a microstrip line, $d=8 \mu\text{m}$, $t=4 \mu\text{m}$, $h=100 \mu\text{m}$, (b) cpw, $d=8 \mu\text{m}$, $s=8 \mu\text{m}$, $a=50 \mu\text{m}$, $h=200 \mu\text{m}$

Similar modifications can be extended to other space directions. Since all field components required in eq. (3.3)-(3.8) are known, only minor additional computations are required.

A convergence test for the variable mesh scheme is given in Fig. 3.2 for a microstrip line and for a conductor backed coplanar waveguide. Fine discretization steps are always used around metal edges and increasing mesh sizes are used away from the edges. The mesh ratios are between neighboring meshes. Good results are obtained for mesh ratios smaller than 4:1. As illustrated in Fig. 3.2 a significant reduction of CPU time can be achieved for grading ratios of 1.5:1 - 2:1. After that the CPU time savings are not as great and the error increases. Compared to the uniform case, this simulation shows that significant computer resources can be saved by using the variable scheme.

$$\mu^n + \alpha_1 \mu^{n-1} + \alpha_2 \mu^{n-2} + \dots + \alpha_{n-1} \mu + \alpha_n = 0 \tag{3.11}$$

so that the left hand term of (3.11) is identified with the product

$$(\mu - \mu_1) (\mu - \mu_2) \dots (\mu - \mu_n) .$$

In order to determine the coefficients $\alpha_1, \dots, \alpha_n$ in (3.11) we multiply the first equation in (3.10) by α_n , the second equation by α_{n-1}, \dots , the n th equation by α_1 , and the $(n+1)$ th equation by 1, and add the results. If we pay attention to the fact that each μ satisfies (3.11), the result is of the form

$$f_n + \alpha_1 f_{n-1} + \dots + \alpha_n f_0 = 0$$

A set of $(N-n-1)$ additional equations of similar type is obtained in the same way by starting instead successively with the second, third, ..., $(N-n)$ th equations. In this way we find that (3.10) and (3.11) imply the $(N-n)$ linear equations

$$f_n + f_{n-1} \alpha_1 + f_{n-2} \alpha_2 + \dots + f_0 \alpha_n = 0$$

$$f_{n+1} + f_n \alpha_1 + f_{n-1} \alpha_2 + \dots + f_1 \alpha_n = 0$$

.....

$$f_{N-1} + f_{N-2} \alpha_1 + f_{N-3} \alpha_2 + \dots + f_{N-n-1} \alpha_n = 0 \tag{3.12}$$

Since the ordinates f_k ($k=1, \dots, n, \dots, N$) are known, this set of equations can be solved directly for the n α 's if $N=2n$, or solved approximated by the method of least squares if $N>2n$.

After the α 's are determined, the n μ 's are found as the roots of (3.11). The equations (3.10) then become linear equations in the n C 's, with known coefficients. The C 's can be determined, finally, from the first n of these equations or, preferably, by applying the least-squares technique to the entire set. Thus the non-linearity of the system is concentrated in a single algebraic equation (3.11). The technique described is known as

Prony's technique.

In order to handle high-Q resonant structures with short time iterations, other signal filtering and spectrum estimation techniques can also be used, such as auto-regressive (AR) and auto-regressive moving average (ARMA) models to improve the efficiency of the FDTD CAD models.

3.3 Improved ABC for FDTD

For open structures absorbing boundary conditions (ABC) are needed to confine a computational domain. Improving the ABC will result in not only higher accuracy but also a reduced computational domain. The Mur's ABC is designed to optimize the boundary condition according to the propagation direction of the waves, which is critical in a small computational domain. The dispersive boundary condition (DBC) in [16] is designed to optimize the boundary condition according to the dispersion characteristics of the waves. The DBC allows the dispersion of the waves to be incorporated into the design of the absorbing boundary condition. This feature is useful when the dispersion for a major outgoing wave is known. However, another feature of the DBC is that it is sensitive to individual structures. Recently, Perfectly Matched Layers (PML) are introduced to effectively absorb outgoing waves [10-12]. However, the number of layers and the layer parameters need to be determined for individual structures. A common feature of available ABCs is that they are valid only for outgoing waves. They work well for antenna and scattering problems, but they can not effectively absorb evanescent modes [13]. This is a major reason why the FDTD method has not been successfully developed for CAD of microwave circuits where higher order evanescent modes exist. Therefore, a good ABC should include a combination of propagation and evanescent modes [13].

Generally, the boundary condition which can absorb both outgoing waves and evanescent modes in the FDTD computational domain can be expressed as [13]

$$\prod_p^P \left(\frac{\partial}{\partial z} + \frac{\beta_p}{C} \frac{\partial}{\partial t} + \alpha_p \right) E = 0, \quad (3.13)$$

in which the kernel, the differential operator, can be approximated by using finite differences (α_p and β_p are constants, C is the speed of light).

Substituting

$$E = \exp\left(j\{\omega t - k_x x - k_y y - k_z z\}\right) + \Gamma \left(\exp\left(j\{\omega t - k_x x - k_y y + k_z z\}\right)\right) \quad (3.14)$$

into the kernel in eq.(3.13) yields

$$\Gamma = \frac{j\beta_p k + \alpha_p - jk_z}{j\beta_p k + \alpha_p + jk_z} \quad (3.15)$$

where $k = \omega/v_p$, k_x , k_y , k_z are respectively the wave numbers in the x-, y-, and z-directions. The wave number k_z generally can be expressed as

$$k_z = \beta_z - j\alpha_z \quad (3.16)$$

which can be substituted into eq.(3.15) and then

$$\Gamma = \frac{j(\beta_p k - \beta_z) + \alpha_p - \alpha_z}{j(\beta_p k + \beta_z) + \alpha_p + \alpha_z} \quad (3.17)$$

From eq. (3.17), we can deduce a rule of thumb in selecting parameters α_p and β_p to minimize the reflection coefficient Γ . For outgoing waves, which correspond to $\alpha_z = 0$, α_p can be set to zero, and β_p is chosen according to the estimated propagation speed and the incident angle of outgoing waves. For evanescent waves, which correspond to $\beta_z = 0$, β_p can be set to zero, α_p is chosen to be the estimated attenuation rate of the fields near the outer boundary. For attenuating-propagation waves, both α_p and β_p can be chosen to be some non-zero numbers.

The ABC utilized above is relatively simple and straightforward. It is easier to understand and implement in CAD program compared to the PML method [10-12].

3.4 Modelling of lossy structures

The new 2D FDTD algorithm is also suitable for the analysis of lossy structures. The conventional 3-D FDTD not only requires huge memory space and long CPU run time, but it also meets difficulties in providing correct solutions. Especially for inhomogeneous transmission lines with losses and finite metallization thickness, there has been no successful method reported yet for accurate FDTD simulations, although Shibata and Sano reported a 3D FDTD technique for lossy media analysis [42]. To solve this problem, other researchers have been trying to apply the 2-D TLM and the 2-D FDTD to this problem [24-25]. The method used in that work is to simulate a resonator. The final solution will be determined by the eigenvalue and its corresponding quality factor as well as the wave velocity. However, the attenuation coefficient is very sensitive to the wave velocity which is calculated through the dispersion curve by $v = \Delta\omega/\Delta\beta$. Any small error in $\Delta\beta$ can cause significant errors in v because $\Delta\beta$ is in that denominator. To overcome these problems, in this section, the field perturbation method is utilized in combination with the real variable 2-D FDTD. Various numerical tests show that this method is robust and accurate. Moreover, a real variable process can be maintained, which was thought to be impossible before.

3.4.1 Attenuation due to lossy dielectric and conductor material

In the conventional 3D FDTD method, lossy media is accounted for by including a conductivity term in the formulation.

In the 2D FDTD method, the attenuation due to imperfect conductor and dielectric losses can be calculated by the field perturbation method which has been widely used, for instance in [52,53]. The attenuation coefficient can be given as

$$\alpha_d = \frac{P_l}{2P_0}, \quad (3.18)$$

where P_0 is the average power transmitted along the z-direction, and P_l is the power loss in the dielectric medium ϵ with loss tangent $\tan\delta$ at the angle frequency ω :

$$P_0 = \frac{1}{2} \text{Re} \left(\int_S \vec{E} \times \vec{H}^* \cdot \hat{n} dS \right), \quad (3.19)$$

$$P_l = \frac{1}{2} \omega \epsilon \tan \delta \int_{S_d} |\vec{E}|^2 dS. \quad (3.20)$$

If the conductor thickness t is sufficiently greater than the skin depth d ($t > 3d$), the fields in the conductor will die out before reaching the other surface, the total power loss in the conductor can be calculated as

$$P_l = \frac{1}{2} R_s \oint_C |\vec{H}_t|^2 dl, \quad (3.21)$$

where R_s is the surface resistance of an infinitely thick conductor and H_t is the tangential magnetic fields on the conductor surface C in the lossless case.

For the very thin conductor ($t < 3d$), the fields are penetrating from both surfaces of the conductor and overlap each other, and the power loss in the conductor must be calculated by

$$P_l = \frac{1}{2} \int_{S_c} \sigma |\vec{E}|^2 dS, \quad (3.22)$$

where S_c is the conductor cross-section. It should be noted that for accurate results, very fine meshes must be used inside the conductor, especially for very thin conductors.

In the 2D FDTD, the transversal electric and magnetic fields are readily obtained in eq. (2.3)-(2.8). From these fields, the total transmission power and the power loss in the medium or in the conductor are calculated, respectively, by eq. (3.19) and eq.(3.20)-(3.22). The attenuation is calculated by eq. (3.18). Therefore, the total attenuation due to the lossy medium and conductors can be obtained by a linear sum of the power losses in the above equations, depending on the thickness of the conductor analyzed.

3.5 FDTD modeling of superconductor circuits

3.5.1 Signal propagation in superconductor CPW

With the introduction of a graded mesh, the FDTD method can now be applied to field simulation in structures with thin conductor layers. In this chapter we will investigate pulse propagation in superconductor conductor backed coplanar waveguide using the

3D FDTD method. The two-fluid model is used to describe the superconductivity. The frequency-dependent negative imaginary part of the conductivity is modeled with the FDTD by storing the electric field history.

The pulse distortion problem in transmission lines may be mainly attributed to two factors: a frequency-dependent propagation velocity due to modal dispersion, and an attenuation due to the skin effect in the conductor.

The existence of the energy gap of superconductors leads not only to significant variations in attenuation of the signal, but also changes in signal velocity. A superconductor is a "perfect" conductor only for DC current. Significant dispersion occurs around the energy gap. All these features are functions of temperature and frequency for a very wide bandwidth (narrow pulse propagation).

Superconductor coplanar waveguides (CPW) and coplanar striplines (CPS) have been studied for microwave applications [50-51]. However, a superconductor can not be simply treated as a low loss conductor, but rather as a conductor with complex conductivity [43-49]. This kind of description is valid for vanishingly small field strength and operating frequency much smaller than the energy gap, and a temperature well below the critical temperature of the superconductor.

Although this problem has been investigated by a number of authors [43-49], investigation of superconductors directly in the time domain was attempted only for one dimensional problems [43]. No data is available so far for superconducting CPW with back metallization. Since the attenuation and phase velocity of signal propagation on superconductors are frequency-dependent, space-dependent, and power-dependent, this interdependency leads itself to a time domain method for the analysis of this kind of problem.

In this section, the FDTD method with variable mesh is utilized to study conductor-backed superconductor coplanar transmission lines. Thin buffer layers are included in the analysis. In order to accurately model the propagation of narrow pulses on these superconductor lines, we will take into account the modal dispersion, dielectric properties of the substrate, the effect of metal backing and ground planes, and the complex conductivity.

3.5.2 FDTD modeling of superconductors

The two-fluid model can be used to describe the superconductors as a conductor with complex conductivity [43-47]

$$\sigma_{sc} = \sigma_1 - j\sigma_2, \quad (3.23)$$

where the frequency-, space-, and power-dependent parameters are given as follows

$$\sigma_1 = \sigma_n \theta, \quad \sigma_2 = 1 / \left(\omega \mu \lambda_L^2(T) \right),$$

$$\lambda_L(T) = \frac{\lambda_L(0)}{\sqrt{1-\theta}}, \quad \theta = (T/T_c)^4,$$

where σ_n , $\lambda_L(0)$ and T_c are the normal conductivity near the critical temperature, zero temperature penetration depth and critical temperature of the superconductor, respectively. For this complex conductivity, Maxwell's equations can be modified as

$$\nabla \times \hat{H} = (j\omega\epsilon + \sigma_1) \hat{E} + \frac{1}{j\omega\mu\lambda_L^2} \hat{E} \quad (3.24)$$

which can also be expressed in the time domain as

$$\nabla \times \hat{H} = \epsilon \frac{\partial}{\partial t} \hat{E} + \sigma_1 \hat{E} + \frac{1}{\mu\lambda_L^2} \int \hat{E} dt. \quad (3.25)$$

First, the electric and magnetic fields are normalized by the free-space wave impedance

$$Z_0 = \sqrt{\mu_0/\epsilon_0}$$

$$\hat{E} \rightarrow \hat{E}/\sqrt{Z_0}, \quad \hat{H} \rightarrow \hat{H} \times \sqrt{Z_0}.$$

Because of the very thin superconductor layer and the high conductivity, a variable mesh and very small time steps are required. The variable mesh algorithm has been developed in Section 3.1 and provides stable solutions with second order accuracy. In order to maximize the stability for the high conductivity of materials used, we use $\sigma_1 \mathbf{E}^{(n+1)}$ for $\sigma_1 \mathbf{E}$. To analyze materials with high conductivity, the FDTD algorithm requires a much smaller

time discretization step Δt to satisfy the stability condition which has not been exactly derived so far. However, in this thesis, it is found that a much larger time step Δt (3~12 times larger for the examples shown in this thesis) can be used if we use $\sigma_1 E^{(n+1)}$ for $\sigma_1 E$ instead of using $\sigma_1 E^{(n)}$. Therefore, the convergence of the FDTD algorithm will be much faster. We assume that all the fields are zero before $t=0$. For instance, the update equation for the electric field E_x at time $t=(n+1)\Delta t$ at point p (i, j, k) (Fig. 3.3) may be given as

$$\begin{aligned}
 E_x^{n+1}(i, j, k) = & \frac{1}{1 + \sigma_1 \Delta t / \epsilon} \left(E_x^n(i, j, k) + \frac{1}{\epsilon_r} \left(\frac{c \Delta t}{\lambda_L} \right)^2 \sum_{p=0}^n E_x^p(i, j, k) \right) \\
 & + \frac{s}{\epsilon_r (1 + \sigma_1 \Delta t / \epsilon)} \left(\frac{H_z^{n+0.5}(i, j, k) - H_z^{n+0.5}(i, j-1, k)}{q_j} \right. \\
 & \left. - \frac{H_z^{n+0.5}(i, j, k) - H_z^{n+0.5}(i, j, k-1)}{r_k} \right) \quad (3.26)
 \end{aligned}$$

where $s=c\Delta t/\Delta h$ with the speed of light $c=2.9979 \times 10^8$ m/s. Similar equations can be obtained for other field components.

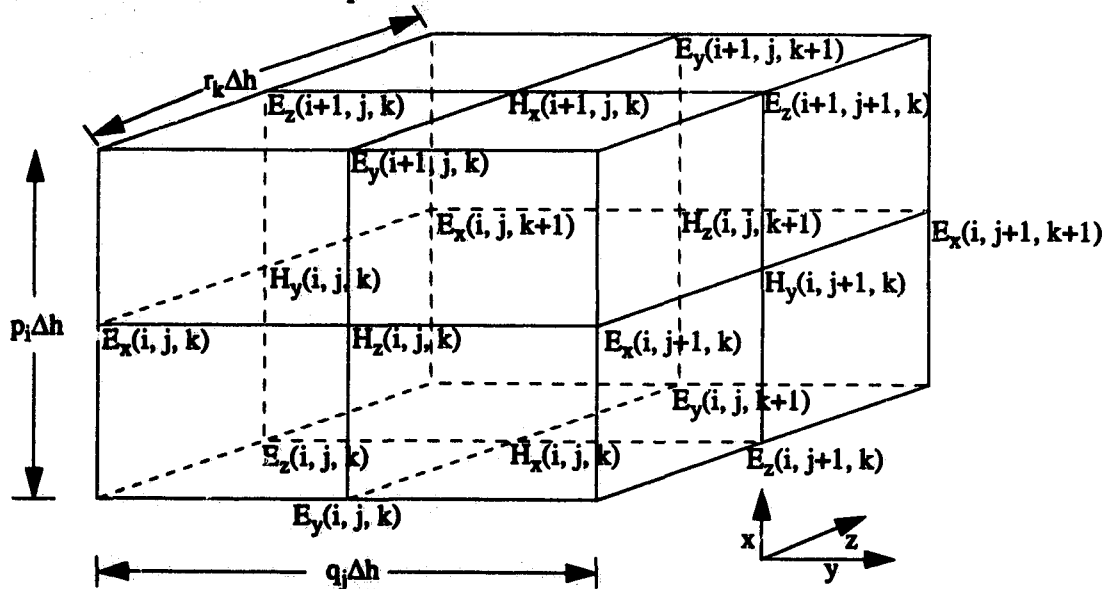


Figure 3.3 A unit FDTD mesh cell with arbitrary variable sizes.

3.5.3 Characterization of anisotropic superconductors

To include also anisotropy of the superconducting film, the complex conductivity may be represented as a tensor

$$\bar{\sigma}_{sc} = \bar{\sigma}_1 - j\bar{\sigma}_2, \quad (3.27)$$

$$\bar{\sigma}_2(T) = \begin{bmatrix} \sigma_x(T) & \sigma_{xy}(T) & 0 \\ \sigma_{yx}(T) & \sigma_y(T) & 0 \\ 0 & 0 & \sigma_z(T) \end{bmatrix}. \quad (3.28)$$

When the principle axes of the superconducting film are aligned with the coordinates, $\sigma_{yx}(T) = \sigma_{xy}(T) = 0$. In the case of YBCO, $\sigma_j = 1/\omega\mu\lambda_j^2$ ($j=x, y, z$), and the penetration depths are equal along the x- and y-axes, namely, $\lambda_x = \lambda_y$. The z-axis penetration depth becomes

$$\sigma_z = \delta\sigma_{x,y} \quad (3.29)$$

where the coefficient δ is constant [43-47]. Then the FDTD can be modified to include this tensor conductivity. The normal state conductivity along the transverse x-y plane is typically almost an order of magnitude higher than the conductivity along the z-axis [43-47].

3.6 Numerical results and discussion

3.6.1 Analysis of microstrip and CPW with lossy media and finite metallization

In this part, we will test and discuss the theory proposed in this chapter. In order to reduce the memory space and run time, symmetrical structures are chosen here without loss of generality. Quasi-static field distributions are usually used as an initial input excitation. After the modes are established, the resulting field distributions are used as an excitation impulse. Absorbing boundary conditions presented in this chapter (Section 3.3 on page 40) are employed to simulate open structures. The numerical study of the effect of stability factor and numerical dispersions is conducted in Appendix B.

Calculation examples are given in the following and compared to experimental results. Fig. 3.4 (a) shows a comparison for the accuracy of attenuation coefficient calculation of the microstrip line between using eq. (3.20) and eq. (3.21). From this example, we

can find that eq. (3.21) gives accurate solutions only for metallization thickness $t > 3d$ (roughly $2.0 \mu\text{m}$ in this case). Eq. (3.20) must be used instead of eq. (3.21) for accurate calculation of thin metallization. For a CPW line, the results calculated from eq. (3.20) and eq. (3.21) are shown in Fig. 3.4 (b), in comparison to experiment [52] and the Spectral Domain Approach (SDA) solution. This example further confirms that eq. (3.21) gives accurate solutions only for metallization thickness $t > 3d$ (roughly $2.5 \mu\text{m}$ in this case). Also here eq. (3.20) must be used instead of eq. (3.21) for accurate calculation of thin metallization.

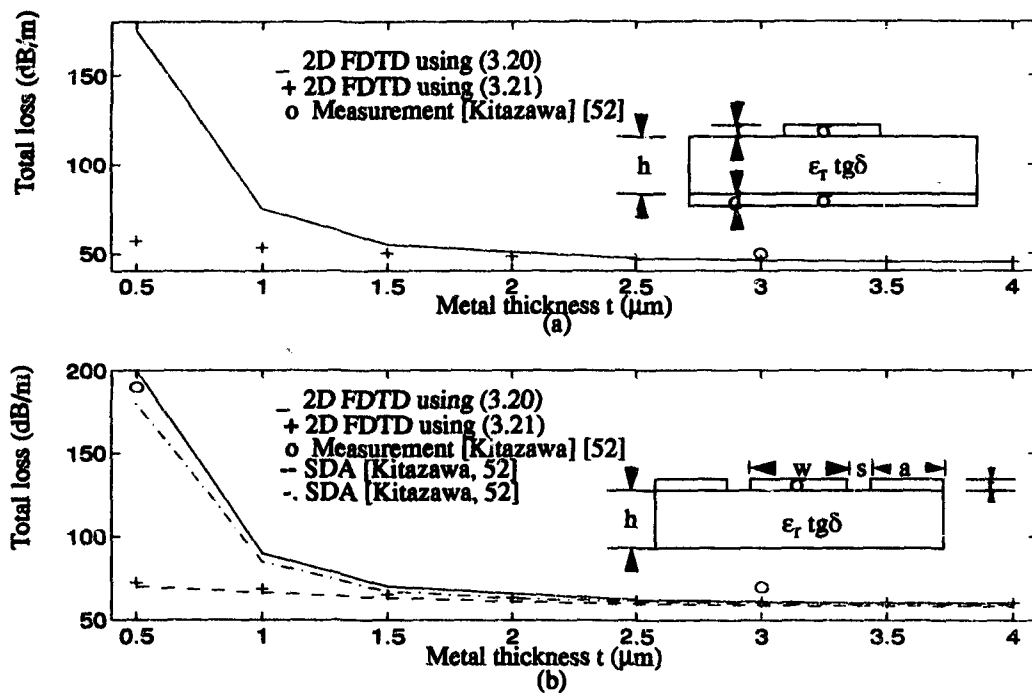


Figure 3.4 Comparison for calculation of losses (lossy media and finite metallization) between eq. (3.20) and eq. (3.21), $\sigma=4.1 \times 10^7 \text{ S/m}$, $\epsilon_r=12.9$, $\text{tg}\delta=3.0 \times 10^{-4}$, (a) a microstrip line, $h=100 \mu\text{m}$, $f=15 \text{ GHz}$, (b) CPW, $h=500 \mu\text{m}$, $w=50 \mu\text{m}$, $w/(w+2s)=0.4$, $f=10 \text{ GHz}$.

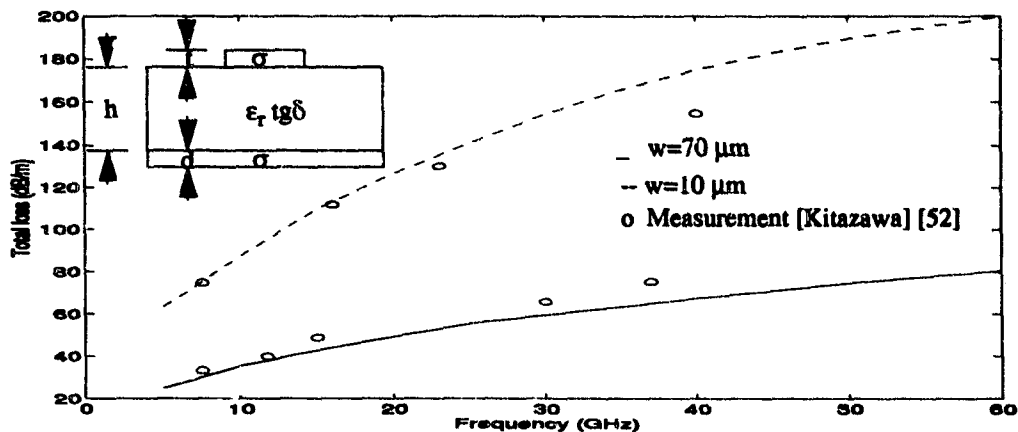


Figure 3.5 Total losses of a microstrip line, $\epsilon_r=12.9$, $\tan\delta=3.0\times 10^{-4}$, $h=100\ \mu\text{m}$, $\sigma=4.1\times 10^7\ \text{S/m}$, $t=3\ \mu\text{m}$.

The frequency dependent attenuation coefficient for a microstrip line is calculated in Fig. 3.5 (eq. (3.20)), and compared to measurements [52]. The real variable 2D FDTD scheme is used here. The graded mesh discretization is utilized. Near the metal strip edge, the discretization steps are $1\ \mu\text{m}$ in vertical y -direction and $2\ \mu\text{m}$ along the horizontal x -direction. Then 5 meshes with a ratio of 1.25 are used away from the metal strip in x -direction, and 1.5:1 is used in y -direction. After that, meshes with ratios of 1.5:1 and 2:1 are used, respectively, along the x - and y -direction. The typical computation time for the structures in Fig. 3.5 is about 20-50 minutes per curve on an IBM Risk 6000. A reasonable agreement between measurement and numerical simulation can be stated.

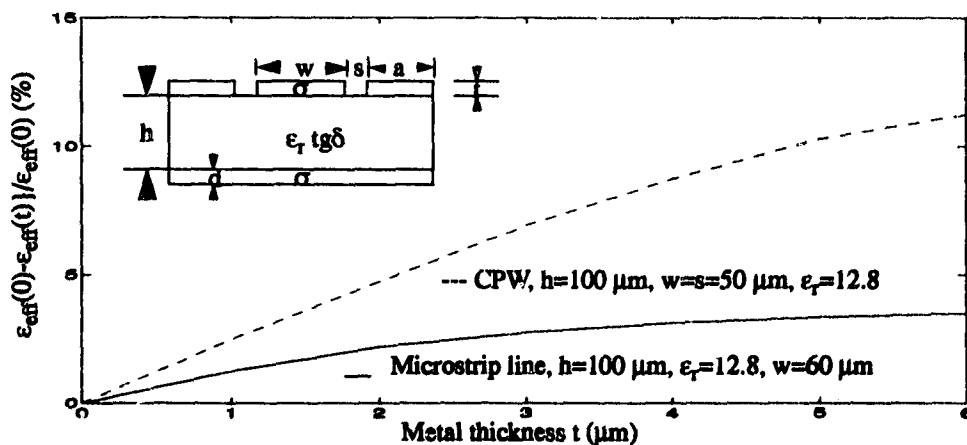


Figure 3.6 Metallization thickness effects of microstrip lines and conductor backed coplanar line, $f=50\ \text{GHz}$.

Fig. 3.6 shows the effect of metallization thickness of the strips on the microstrip

line and conductor-backed CPW. It is found that the metallization thickness has a significant effect on the transmission characteristics, especially for conductor-backed CPW, and this kind of effect must be taken into account for practical circuit design. From the calculation of microstrip lines and coplanar waveguides, it was found that the metal strip loss is dominant. It was also found that the dielectric loss is small and the ground plane metal loss is negligible. Therefore, results for these two loss factors are not shown here. Only the total attenuation is shown in the figures. Fig. 3.7 (a) shows the total losses of a microstrip line with different metal strip width. The narrower the strip is, the larger the losses will introduce. That explains why miniaturizing circuits will increase the losses. Fig. 3.7 (b) shows results for a conductor-backed coplanar waveguide with different metal strip and slot widths. For a constant slot width, also here the losses increase when the strip width decreases.

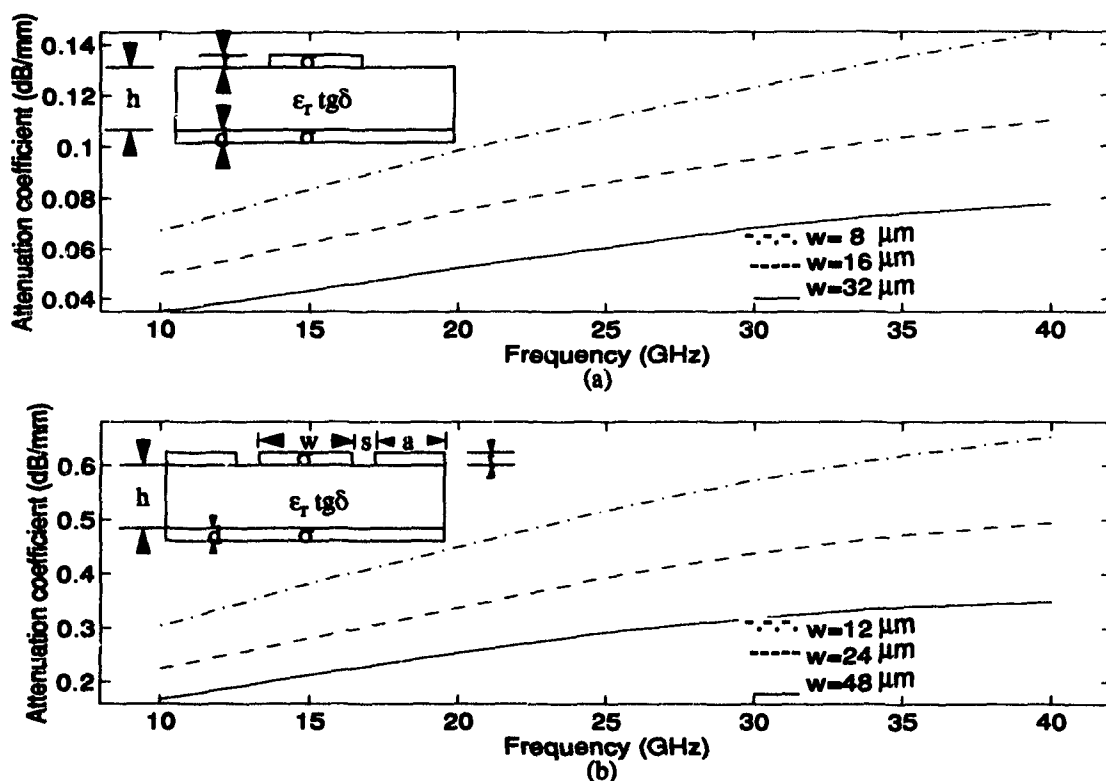


Figure 3.7 Frequency dependency of attenuation coefficient for GaAs transmission lines, $\epsilon_r = 12.9$, $d = 8 \mu\text{m}$, $s = 8 \mu\text{m}$, $a = 50 \mu\text{m}$, $h = 200 \mu\text{m}$.

3.6.2 Analysis of metal-insulator-semiconductor transmission lines

Further examples of lossy structures are given for metal-insulator-semiconductor (MIS) transmission lines in Fig. 3.8 and compared to the experimental results [42].

MIS transmission lines find wide application in monolithic microwave integrated circuits, where the existence of propagation modes with low phase velocity allows to reduce the dimension of the distributed circuits. The applications also include devices such as variable attenuators and phase shifters. Basic studies of MIS structures have been made experimentally and numerically [42,61]. In the following the real variable 2D FDTD method is applied to only half of the MIS CPW in Fig. 3.8 due to the symmetry of the structure. The smallest meshes of $0.5 \mu\text{m}$ are used around the slot. The mesh sizes increase away from the slot with mesh ratio 1.2:1. The total matrix size is 40×30 . The time step is chosen as $\Delta t = 0.835 \text{ fs}$. The cpu time for Fig. 3.8 is about 25 minutes.

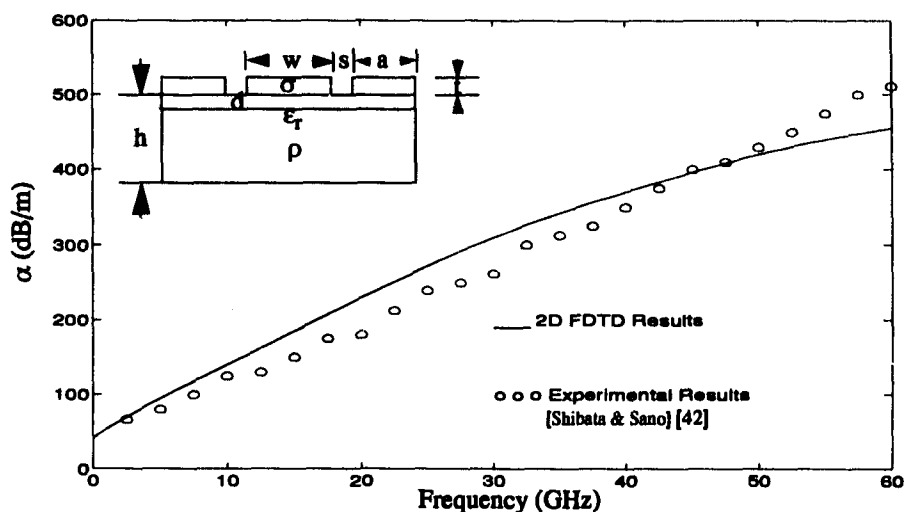


Figure 3.8 Numerical results of 2D FDTD compared to the experiment in [42]; $h=490$, $d=2$, $t=1$, $w=10$, $s=5$, $a=50$, $\epsilon_r=4$, $\rho=15\Omega$, $\sigma=2.75 \times 10^7 \text{ S/m}$, all dimensions are in μm .

3.6.3 Field distribution in superconductor CPW

In order to verify the above 3D FDTD model of superconductors, different Gaussian pulses are used to excite a coplanar waveguide. The strip width is $15 \mu\text{m}$, the gap is $10 \mu\text{m}$, and the dielectric substrate thickness is $100 \mu\text{m}$ with dielectric constant $\epsilon_r=12.9$, and a small loss of $\text{tg}\delta=4.0 \times 10^{-7}$ (Fig. 3.9). The superconductor strip has a thickness of $1.0 \mu\text{m}$, and the material is characterized by $T_c=92.5 \text{ K}$, the penetration depth is $\lambda=0.3 \mu\text{m}$, $\sigma=1.7 \text{ S}/\mu\text{m}$. The ambient temperature is taken as 77 K . Fig. 3.10 and Fig. 3.11 show a Gaussian pulse propagating smoothly through a CPW line after $t=400$ and $t=600$ time steps, respectively. The pulse width used is $W=40 \text{ ps}$. Total meshes used are $10 \times 30 \times 120$ (height

by width by length). Typical CPU time is around 40 minutes. We find that the narrower the pulse width, the more distorted the pulse shape becomes. This distortion may be due to the modal dispersion and leakage effects. The higher frequencies travel at a slower velocity, resulting in increased pulse distortion, and ringing on the back of the pulse. These effects will increase with transmission distance and are more pronounced for narrow pulses or large structure dimensions.

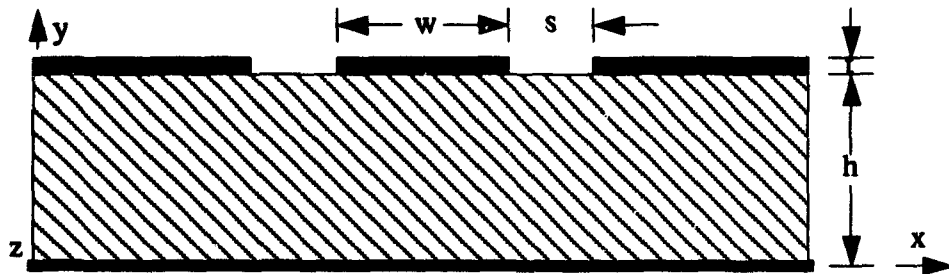


Figure 3.9 Conductor-backed coplanar waveguide, $w=15\ \mu\text{m}$, $s=10\ \mu\text{m}$, $h=100\ \mu\text{m}$, $t=1\ \mu\text{m}$, $\epsilon_r=12.8$, $\text{tg}\delta=4.0\times 10^{-7}$

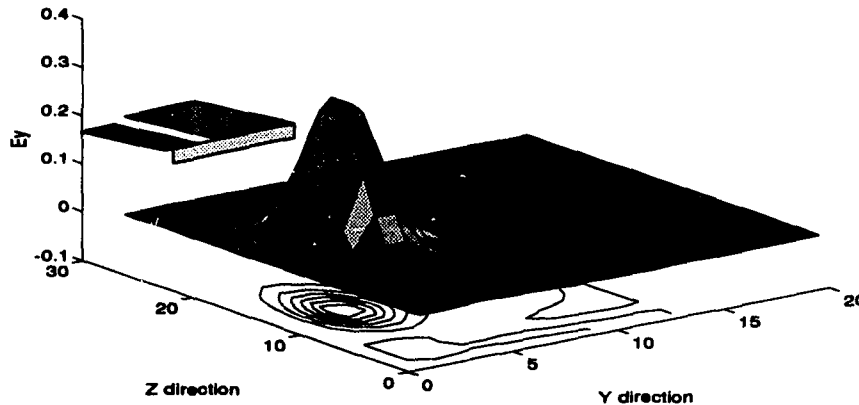


Figure 3.10 Gaussian pulse with width 40 ps in the superconductive CPW line, $t=400dt$

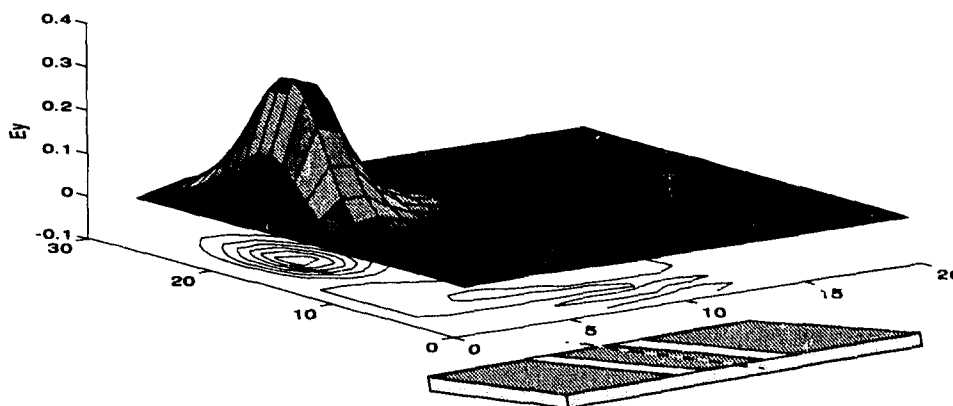


Figure 3.11 Gaussian pulse with width 40 ps in the superconductive CPW line, $t=600dt$

3.6.4 Effect of buffer layers in superconductor transmission lines

The attenuation characteristic of a superconductor microstrip line with buffer layer is analyzed using the variable mesh 3D FDTD. Results are shown in Fig. 3.12 and Fig. 3.13.

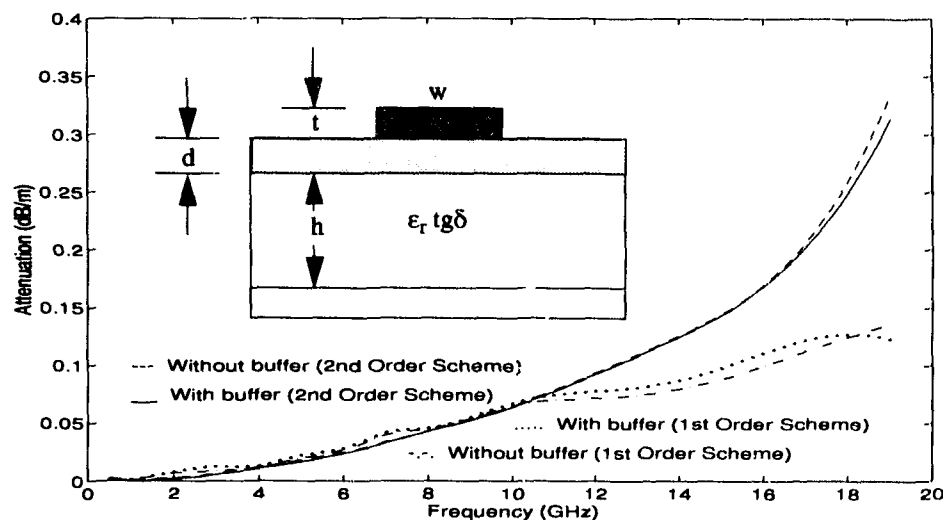


Figure 3.12 Attenuation of a superconductor microstrip line with and without a buffer layer ($\epsilon_r=500$, $d=0.1 \mu\text{m}$), $w=150 \mu\text{m}$, $t=0.5 \mu\text{m}$, $h=500 \mu\text{m}$, $\epsilon_r=9.8$, $\lambda=0.2 \mu\text{m}$, $\sigma_1=1.0 \text{ S}/\mu\text{m}$, $T_c=93 \text{ K}$, $T=77 \text{ K}$, $\lambda_2=5\lambda_{x,y}$

Fine meshes of $0.1 \mu\text{m}$ are used in the buffer layer and conductor. The mesh ratio is 2:1 away from the buffer layer and the microstrip edge. Half of the structure is discretized by 40×30 meshes in the transverse plane. A total of 160 uniform meshes are used in wave propagation direction. From Fig. 3.12, one can clearly see the problems in the

original Yee's algorithm with variable meshes which do not represent the real phenomenon very well since the first order errors accumulate and cause uncertain and erroneous results, especially for frequencies above 10 GHz in this example. Therefore the improvements in the second order grading schemes developed in this thesis are necessary for correct results in the analysis of thin film superconductors. For the thin metal and buffer layers chosen here, the buffer layer influence on the attenuation is marginal. This is not the case for the propagation constant, as illustrated in Fig. 3.13. The tensor conductivity in this structure was chosen to be $\lambda_z=5\lambda_{x,y}$.

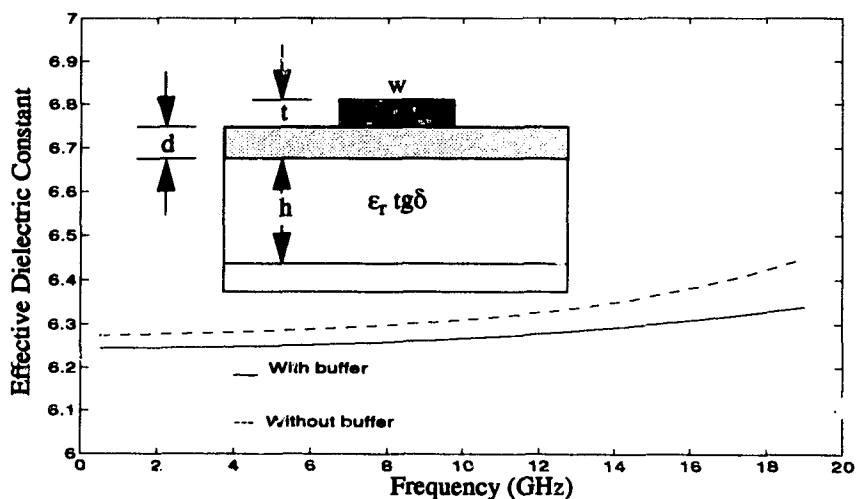


Figure 3.13 Propagation Characteristic of a superconductor microstrip line with and without a buffer layer ($\epsilon_r=500$, $d=0.1 \mu\text{m}$), $w=150 \mu\text{m}$, $t=0.5 \mu\text{m}$, $h=500 \mu\text{m}$ $\epsilon_r=9.8$, $\lambda=0.2 \mu\text{m}$, $\sigma_1=1.0 \text{ S}/\mu\text{m}$, $T_c=93 \text{ K}$, $T=77 \text{ K}$, $\lambda_z=5\lambda_{x,y}$

Similar results and conclusions are valid for CPW structures. The attenuation of a superconductor CPW with buffer layer is shown in Fig. 3.14, where for the thin metal and buffer layer chosen here, the buffer layer influence is negligible. But this is not the case for the propagation constant, as illustrated in Fig. 3.15.

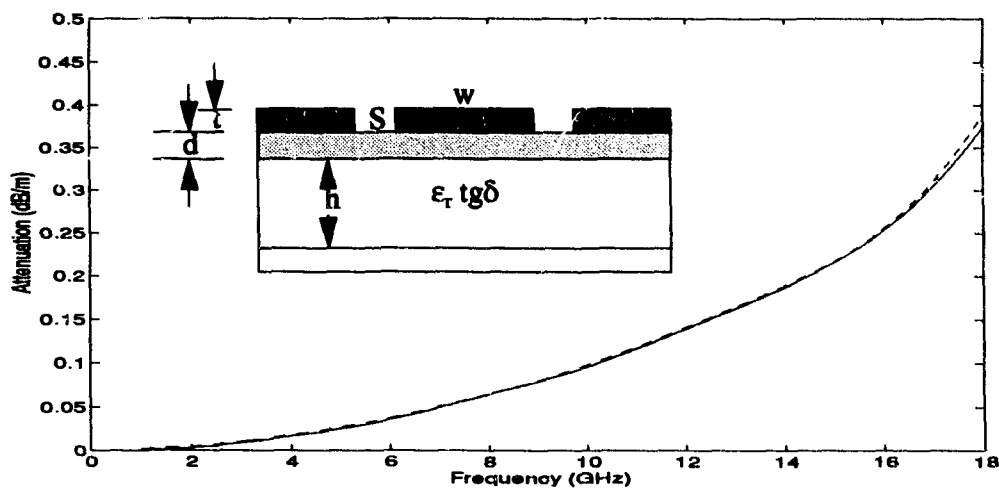


Figure 3.14 Attenuation Characteristic of a superconductor CPW with (solid line) and without (dashed line) a buffer layer ($\epsilon_r=500$, $d=0.1 \mu\text{m}$), $w=150 \mu\text{m}$, $s=100 \mu\text{m}$, $t=0.5 \mu\text{m}$, $h=500 \mu\text{m}$ $\epsilon_r=9.8$, $\lambda=0.2 \mu\text{m}$, $\sigma_1=1.0 \text{ S}/\mu\text{m}$, $T_c=93 \text{ K}$, $T=77 \text{ K}$, $\lambda_z=5\lambda_{x,y}$

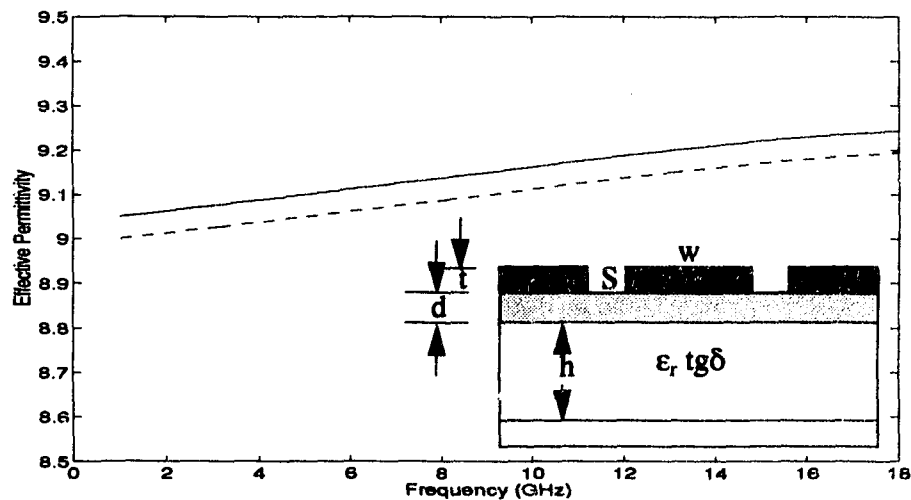


Figure 3.15 Propagation Characteristic of a superconductor CPW with (solid line) and without (dashed line) a buffer layer ($\epsilon_r=500$, $d=0.1 \mu\text{m}$), $w=150 \mu\text{m}$, $s=100 \mu\text{m}$, $t=0.5 \mu\text{m}$, $h=500 \mu\text{m}$ $\epsilon_r=9.8$, $\lambda=0.2 \mu\text{m}$, $\sigma_1=1.0 \text{ S}/\mu\text{m}$, $T_c=93 \text{ K}$, $T=77 \text{ K}$, $\lambda_z=5\lambda_{x,y}$

3.6.5 Superconductor CPW gap resonator

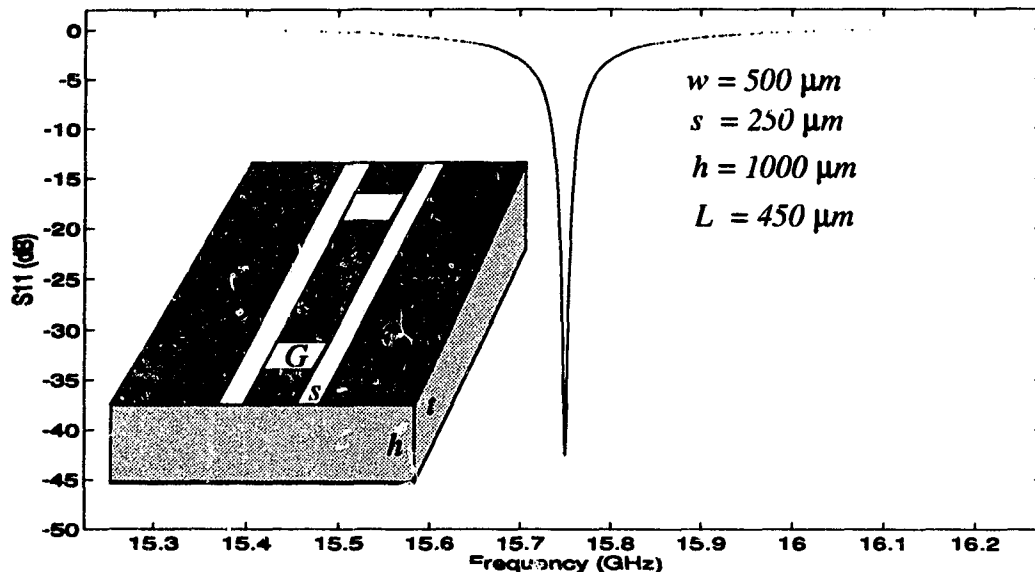


Figure 3.16 CPW gap resonator, $\epsilon_r=9.8$, $\lambda=0.18 \mu\text{m}$, $\sigma_1=1.0 \text{ S}/\mu\text{m}$, $T_c=86 \text{ K}$, $T=80 \text{ K}$, $\lambda_z=5\lambda_{x,y}$, a buffer layer ($\epsilon_r=500$, $d=0.1 \mu\text{m}$), $t=0.5 \mu\text{m}$

Fig. 3.16 demonstrates the application of the 3D FDTD method for the analysis of a superconductor CPW resonator. The dimensions are given in Fig. 3.16. A buffer layer of $d=0.1 \mu\text{m}$ is considered and the metal strip thickness is $t=0.5 \mu\text{m}$. The ratio between the largest and the smallest circuit detail is $h:d=10000:1$. The conventional uniform discretized 3D FDTD method is not able to solve this structure without the use of a supercomputer. However, with the variable mesh FDTD developed in this thesis we were able to analyze the structure on a workstation computer. The finest mesh is $0.1 \mu\text{m}$. The mesh sizes increase with ratio 1.5:1 away from the conductors and the buffer layer. The CPU time for S-parameter calculations is about 5 hours per curve on an IBM Risk6000 computer. With a gap width of $G=200 \mu\text{m}$, the resonance peak was calculated at 15.75 GHz.

3.6.6 Analysis of electrooptic modulator

The cross section of a typical electrooptic modulator is shown in Fig. 3.17. An optical waveguide has been formed in the surface region of a lithium niobate substrate by the indiffusion of titanium. Coplanar control electrodes are separated from the lithium niobate by a thin silicon dioxide buffer layer. The optical waveguide is located below the gap

between the strips (Fig. 3.17) or otherwise below strip edges depending on the direction of the controlling electric field. This integrated electrooptic modulator is based on the interaction of a controlling electric field with the field of a guided optical wave in a dielectric medium. The permittivity of the guiding medium is perturbed through the linear electrooptic effect (Pockels) [93], achieving electrooptic modulation. To maximize the electrooptic effect, the optical axis of the lithium niobate is aligned with the direction of the polarization of the optical wave. The ultimate limit of the bandwidth for traveling wave modulators is set by the difference between velocities of the optical and electrical signals. To overcome this velocity mismatch limitation and optimize the electrooptic interaction operating at higher frequencies, clearly an accurate characterization of microwave propagation parameters with dispersion effects is required. Basic problems in previous work has been the accuracy and efficiency of analysis and design of these integrated optical modulators [94]. Because of its flexibility, the FDTD method is suitable for this structure with the complex media.

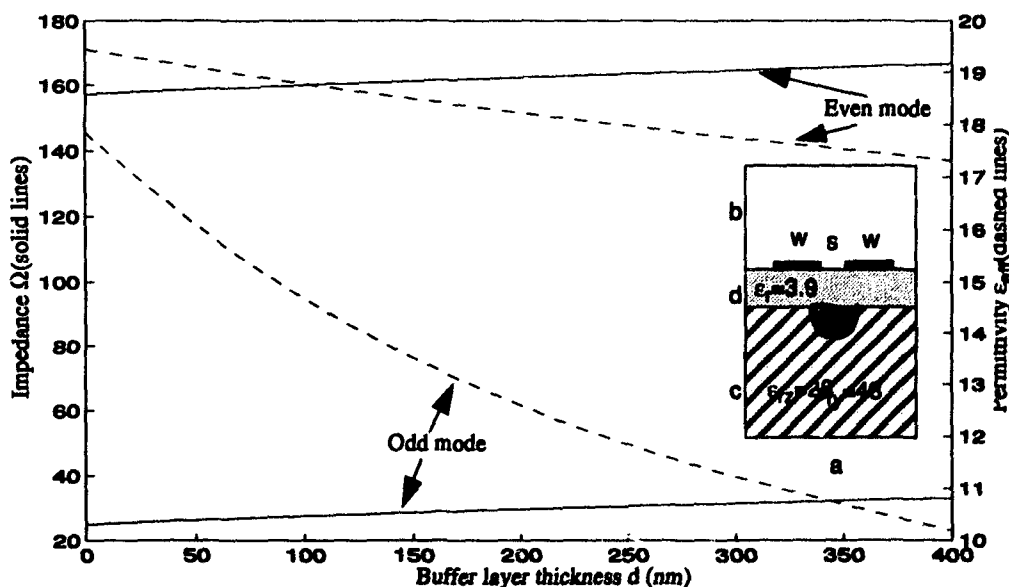


Figure 3.17 Calculation of propagation characterization of an electrooptic modulator, $s=5\mu\text{m}$, $w=8\mu\text{m}$, $a=4\text{mm}$, $b=10\text{mm}$, $c=1\text{mm}$, $d=0\sim 0.4\mu\text{m}$, $\lambda=5\text{mm}$.

The substrate of integrated optical modulators is usually made of anisotropic dielectric. This anisotropy can be modelled with the FDTD discussed in Section 3.5.3. Also, a buffer layer is usually used to minimize the optical loss. Without considering the metallization thickness in this example, the calculation effort is greatly reduced. The real variable grading 2D FDTD algorithm needs about 30×20 meshes with mesh ratio 2.5:1. Typical cpu time is about 5 minutes per buffer layer thickness.

3.6.7 Probe-fed waveguides

3.6.7.1 Introduction

Further applications of the FDTD algorithm developed in this thesis are in the area of waveguide components. For example, the input and output ports of microwave periodic or cavity filters are usually realized by coaxial probe (Fig. 3.18) protruding into the waveguide on the wide side of the rectangular waveguide with an electric wall on one side of the probe and the filter on the other side in order to avoid using extra waveguide transitions.

Although the probe-excited waveguide has been treated numerically by several authors [88-90], the assumption of semi-infinite long waveguides and certain uniform current distribution was always made to extract empirical formulas. Unfortunately a recent work by Zaki and Liang [90] still dealt with the semi-infinite waveguide with limited accuracy. Therefore, fine-tuning is necessary.

To eliminate the need for fine tuning, our objective is to establish some design data from exact numerical analysis utilizing the 3D FDTD method.

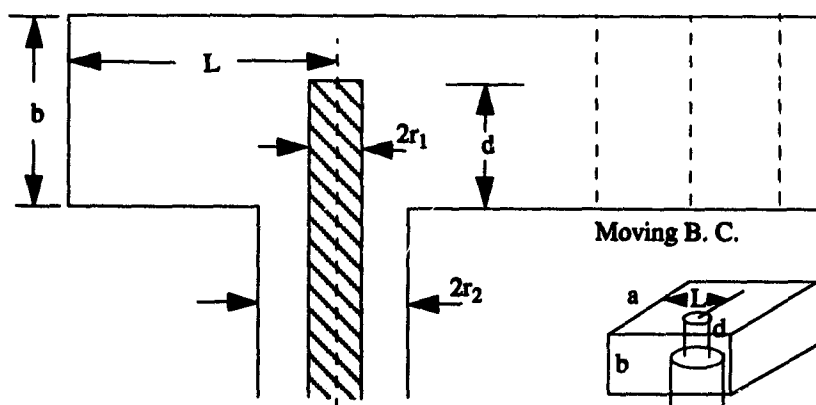


Figure 3.18 Cross section of the coaxial fed probe in a rectangular waveguide

The goal is to obtain maximum efficiency of coupling energy into the filter. The question then is:

What is the optimum dimensions and locations of the probe in order to effectively couple the coaxial line signal into the filters? Or in other words, what is the minimum reflection if we have different choices of the matching network?

3.6.7.2 Coaxial Probe in Waveguides

For the probe-excited waveguide structure with loading effect (Fig. 3.19), the variable mesh FDTD will be used and the boundary of the coaxial waveguide will be approximated by staircase function. Analytical quasi-static field distributions are enforced in the coaxial line. The spectra of the reflected pulse over that of the input pulse determine the S-parameters or the input impedance. The next task will be to determine how the dimensions affect the input impedance.

Some approximations and limitations include: (1) perfect conductors are always assumed although this is not necessary; (2) only symmetrical structures have been analyzed to save computation efforts.

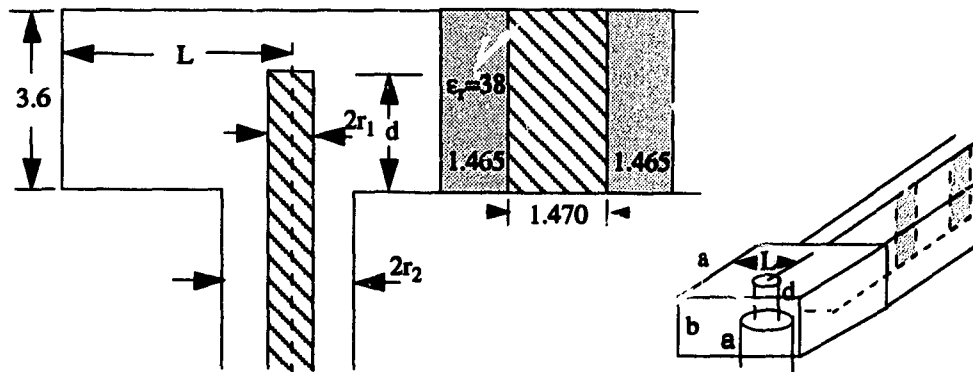


Figure 3.19 Cross section of the coaxial fed probe in waveguides with loading, all dimensions are in mm, $a=12.5$, $b=3.6$, dielectric thickness of the E-plane filter= 0.635 .

3.6.7.3 Effect of the probe insertion depth in the waveguide

The dimension is chosen as required in Fig. 3.19. The waveguide width is $a=12.5$ mm, the height is $b=3.6$ mm. The waveguide is fed by a RG-142 coaxial line, with inner conductor diameter $r_1=0.89$ mm and outer conductor diameter $r_2=2.95$ mm. The dielectric is Duroid ($\epsilon_r = 2.2$). The first higher order mode cutoff frequency in the coaxial line is

around 17 GHz. A 5% margin is used so that $f=16$ GHz. The operation center frequency of the loading section is at $f = 14.2$ GHz.

The simulation results are shown in Fig. 3.20. It is evident that (1) for different probe positions, L , away from the short circuit plane, the input impedance is increasing as the probe insertion depth increases; (2) It is not possible to improve the matching results (near 50 ohms) by using a shorter insertion depth. For the probe which is around 5 mm away from the short plane, we need around 3 mm insertion depth of the probe to have 50 ohms of the real part of the impedance. It is difficult or impossible to match the coaxial line with the probe very near to the short plane. The distance L must be large enough to achieve a matching condition.

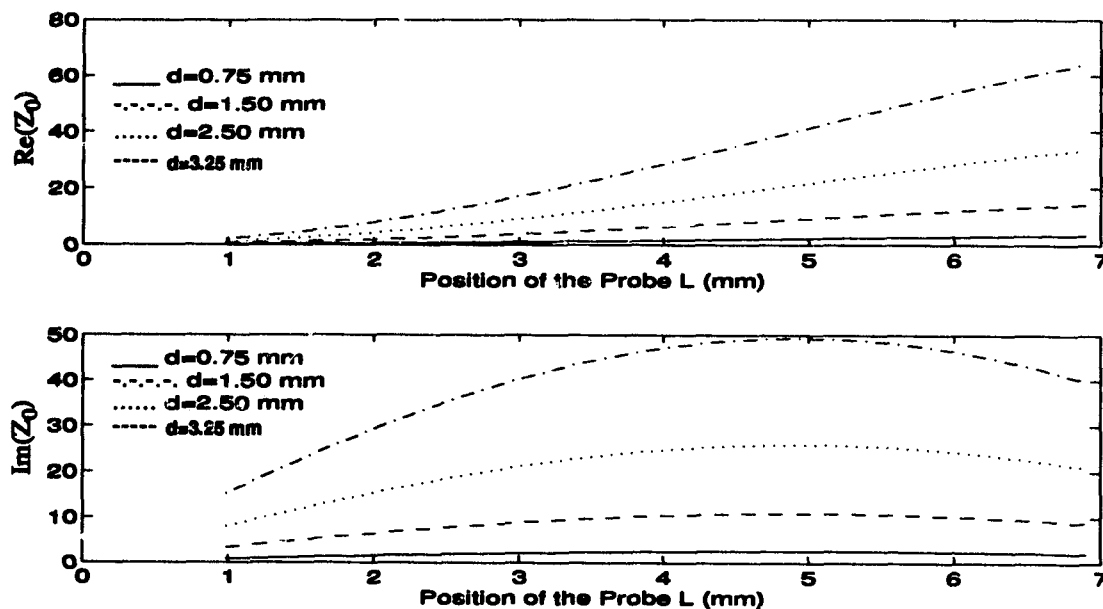


Figure 3.20 Effect of the probe position L for different probe insertion depth d

3.7 Conclusion

An effective variable mesh scheme has been described to further increase the FDTD efficiency. Prony's method and a modified ABC have been discussed. Application examples to lossy structures, superconductors, and waveguide discontinuities have been presented.

Chapter 4

Modified method of lines

This chapter presents a modified method of lines in which the error $o(h^2)$ inherent in the traditional method has been reduced to $o(h^4)$. The resulting algorithm provides better accuracy, reduced memory space and shorter computation time.

4.1 Introduction

To place the improvements made to the MoL in a better context, the following paragraph summarizes the basic features of the method. The MoL is a semi-analytical method first introduced in 1930 by Russian mathematicians. Since then the method has been further developed, until in 1980 it was first applied to microwave problems by Pregla and co-workers [55-60].

The MoL analysis of hybrid-modes in arbitrarily shaped planar and quasi-planar electromagnetic structures is based on two independent scalar potential functions from which all electromagnetic field components are derived. These potential functions satisfy Helmholtz equation and the correspondent boundary conditions. Applying the MoL, for instance, to a layered quasi-planar multi-conductor transmission line, the electric and magnetic potentials are discretized by vertical straight lines which are normal to the metal strips and the dielectric interfaces. After some mathematical preprocessing, the discretized Helmholtz equations are diagonalized and then solved analytically. Using the central finite difference scheme to approximate the first order partial differential operator two neighboring field components are required. This leads to an accuracy of $o(h^2)$ because the value of the first order differential is defined in the middle between these two

field components. The electric and magnetic potential functions are shifted with each other. This is not only convenient for matching the boundary conditions, but the advantage of this shifting is also that second order accuracy is preserved simultaneously for both e-lines and h-lines. This is important when the first order differentials are used to calculate the second order differential operator which is defined at the exact same point as the field component itself, namely in the middle between two neighboring first order differentials. Therefore, in both approximations, the error is on the order of $o(h^2)$, with h being the spacing between the lines. The same applies for the field continuity conditions. The first order differential operator is defined in the middle (central finite difference) between the two field components. Otherwise, only a first order accuracy can be obtained. Since the accuracy of the method mainly depends on the size of the discretization steps, it is obvious that the finer the steps, the better the results from this scheme. On the other hand, the use of finer discretization steps means also that the memory space and CPU-time would increase. To overcome this problem, it is better not to increase the number of lines but to increase the accuracy of the scheme itself.

In this chapter a modified approach to the method of lines is introduced which reduces the error to a higher order, $o(h^4)$. This leads to a faster convergence rate compared to the conventional MoL. Or, in other words, to achieve the same accuracy known from the conventional approach, a smaller number of lines is required.

To appreciate the modifications made in this thesis, one must understand that the overall error in the MoL results not only from the discretizations of the Helmholtz equation, but also from the continuity equation and the edge condition. In previous work it was tried to modify the scheme only in part [55], but an overall improvement was not achieved. The important point was that any modification in only one of above sources of error will not lead to a reduction of the overall error. In [55] the fourth order scheme was only applied to the discretization of the Helmholtz equation. However, instead of a better accuracy less accurate results were obtained. Application of the fourth order scheme to all three sources of error was first demonstrated in [70] with excellent results. This work was further applied to optic waveguides in [97].

In the following, details of the modified scheme as it applies to the Helmholtz equation, matching condition and edge condition will be discussed.

For clarity, the discussion will be limited to 2D problems only. An extension of the approach to 3D discontinuities is straightforward.

4.2 Method of analysis

4.2.1 Discretization of Helmholtz equation

A planar microwave structures with several homogeneous layers of dielectric is assumed. The electromagnetic field in each homogeneous region can be derived from two independent scalar potential functions ϕ_e and ϕ_h which satisfy the Helmholtz equation and the boundary conditions at the lateral walls.

The field components are related to the potential functions ϕ_e and ϕ_h as

$$E = \frac{1}{j\omega\epsilon} \nabla \times \nabla (\phi_e \hat{z}) - \nabla (\phi_h \hat{z}) , \quad H = \frac{1}{j\omega\mu} \nabla \times \nabla (\phi_h \hat{z}) + \nabla (\phi_e \hat{z}) . \quad (4.1)$$

Both scalar potentials, ϕ_e and ϕ_h satisfy the Helmholtz equation

$$\frac{\partial^2 \phi}{\partial x^2} + \frac{\partial^2 \phi}{\partial y^2} + (k^2 - \beta^2) \phi = 0 . \quad (4.2)$$

($k = \omega\sqrt{\mu\epsilon}$) and the boundary conditions. A time harmonic term of $\exp(j\omega t - j\beta z)$ is always assumed.

Since the hybrid field problem can not be solved analytically for the whole region, the calculation domain is discretized along the x-direction by a number of straight lines along the y-axis, which are spaced by a constant h . The discretization lines for the electric potential function ϕ_e are shifted with respect to the lines ϕ_h by a distance of half a discretization step, $h/2$. By doing this, the boundary conditions can be fitted easily and the discretization error of the Helmholtz equation can be reduced from the first order $o(h)$ to

second order $o(h^2)$.

The discretized potential functions ϕ_e and ϕ_h are placed at equidistant intervals x_i ($i= 1, 2, 3, \dots, N$)

$$x_i = x_0 + ih, \quad (4.3)$$

with h being the spacing between the lines (Fig. G.1).

It should be noted that the first order partial derivatives of ϕ_e fall on the ϕ_h lines and vice versa when the central finite difference approximation is utilized

$$\left. \frac{\partial \phi_{e,h}}{\partial x} \right|_{i+0.5} = \frac{\phi_{e,h}|_{i+1} - \phi_{e,h}|_i}{h}, \quad i= 1, 2, 3, \dots, N, \quad (4.4)$$

or, in a matrix notation

$$h \frac{\partial \bar{\phi}_{e,h}}{\partial x} = [D] \bar{\phi}_{e,h}. \quad (4.5)$$

The first order difference operator, $[D]$, depends on the lateral boundary conditions. For instance, for the Neumann-Dirichlet (N-D) case, $[D]$ reads as

$$[D] = \begin{bmatrix} -1 & 1 & 0 & \dots & 0 & 0 \\ 0 & -1 & 1 & \dots & 0 & 0 \\ 0 & 0 & -1 & \dots & 0 & 0 \\ \dots & \dots & \dots & \dots & \dots & \dots \\ 0 & 0 & 0 & \dots & -1 & 1 \\ 0 & 0 & 0 & \dots & 0 & -1 \end{bmatrix}, \quad -[D]^t = \begin{bmatrix} -1 & 0 & 0 & \dots & 0 & 0 \\ 1 & -1 & 0 & \dots & 0 & 0 \\ 0 & 1 & -1 & \dots & 0 & 0 \\ \dots & \dots & \dots & \dots & \dots & \dots \\ 0 & 0 & 0 & \dots & -1 & 0 \\ 0 & 0 & 0 & \dots & 1 & -1 \end{bmatrix}. \quad (4.6)$$

Applying the central finite difference scheme again to calculate the second order partial differential operator yields:

$$h^2 \frac{d^2 \bar{\phi}_e}{dx^2} = -[D]^t [D] \bar{\phi}_e = [P_e] \bar{\phi}_e, \quad h^2 \frac{d^2 \bar{\phi}_h}{dx^2} = -[D] [D]^t \bar{\phi}_h = [P_h] \bar{\phi}_h.$$

For the special case of N-D boundaries, $[P_e]=[P_h]=[P]$. Then the wave equation (eq. (4.2)) becomes

$$\frac{d^2 \phi_i}{dy^2} + \frac{1}{h^2} [\phi_{i-1} - 2\phi_i + \phi_{i+1}] + (k^2 - \beta^2) \phi_i = r_i, \quad i = 1, 2, 3, \dots, N, \quad (4.7)$$

where the discretization error

$$r_i = \frac{h^2}{12} \frac{\partial^4}{\partial x^4} \phi_i + \frac{h^4}{360} \frac{\partial^6}{\partial x^6} \phi_i + o(h^6) \quad (4.8)$$

is dominated by the $o(h^2)$ term.

When we omit the discretization errors in (4.7), the discretized wave equation can be written as

$$\frac{d^2 \bar{\phi}}{dy^2} + \left\{ (k^2 - \beta^2) [I] - \frac{1}{h^2} [P] \right\} \bar{\phi} = 0. \quad (4.9)$$

Since the accuracy of the method mainly depends on the size of the discretization steps, it is obvious that the finer the steps, the better the results from this scheme. On the other hand, the use of finer discretization steps means also that the memory space and CPU-time would increase. To overcome this problem, it is better not to increase the number of lines but to increase the accuracy of the scheme itself.

To eliminate the $o(h^2)$ term in eq.(4.7), at any index i , this equation must be combined with the equations at the three neighboring lines, $i-1$, i and $i+1$. It is found that appropriate coefficients can be found to cancel the $o(h^2)$ providing an $o(h^4)$ accuracy.

The mathematical procedure is as follows. Combining the discretized Helmholtz equations at the two neighboring lines and the line itself with appropriate coefficients leads to the following expression (details can be found in Appendix G):

$$\begin{aligned} & \frac{1}{12} \frac{d^2}{dy^2} (\phi_{i-1} + 10\phi_i + \phi_{i+1}) + \frac{1}{h^2} (\phi_{i-1} - 2\phi_i + \phi_{i+1}) \\ & + \frac{1}{12} (\phi_{i-1} + 10\phi_i + \phi_{i+1}) (k^2 - \beta^2) \phi_i = r_{io}, \quad i=1, 2, 3, \dots, N, \end{aligned} \quad (4.10)$$

where, the discretization error is now reduced to $o(h^4)$

$$r_{io} = \frac{7h^4}{720} \frac{\partial^6}{\partial x^6} \phi_i + o(h^6), \quad i=1, 2, 3, \dots, N. \quad (4.11)$$

Omitting the error term, eq. (4.10) can be written in matrix form as

$$[Q] \frac{d^2 \Phi}{dy^2} + \{ (k^2 - \beta^2) [Q] - \frac{1}{h^2} [P] \} \Phi = 0, \quad (4.12)$$

where the matrices [P] and [Q] are of tri-diagonal form

$$[Q] = \frac{1}{12} \begin{bmatrix} q_1 & 1 & 0 & \dots & 0 & 0 \\ 1 & 10 & 1 & \dots & 0 & 0 \\ 0 & 1 & 10 & \dots & 0 & 0 \\ \dots & \dots & \dots & \dots & \dots & \dots \\ 0 & 0 & 0 & \dots & 10 & 1 \\ 0 & 0 & 0 & \dots & 1 & q_2 \end{bmatrix}, \quad [P] = \begin{bmatrix} p_1 & -1 & 0 & \dots & 0 & 0 \\ 1 & 2 & -1 & \dots & 0 & 0 \\ 0 & -1 & 2 & \dots & 0 & 0 \\ \dots & \dots & \dots & \dots & \dots & \dots \\ 0 & 0 & 0 & \dots & 2 & -1 \\ 0 & 0 & 0 & \dots & -1 & p_2 \end{bmatrix},$$

with the coefficients p_i and q_i ($i=1$ or 2) depending on the lateral boundary conditions

$$p_i = \begin{cases} 2, & i=1 \text{ or } 2; \text{ for the Dirichlet (D) boundary conditions.} \\ 1, & i=1 \text{ or } 2; \text{ for the Neumann (N) boundary conditions.} \end{cases}$$

$$q_i = \begin{cases} 10, & i=1 \text{ or } 2; \text{ for the Dirichlet (D) boundary conditions.} \\ 11, & i=1 \text{ or } 2; \text{ for the Neumann (N) boundary conditions.} \end{cases}$$

It is found that the difference between the new scheme and the conventional MoL in the discretization of the Helmholtz equation is that, instead of only a tri-diagonal matrix [P], there is now an additional matrix [Q] to be considered, which is different

from [P]. In other words, to find an analytical solution for this equation, one must not only diagonalize matrix [P] but also matrix [Q] with the same transformation.

For any kind of lateral boundary condition, one can always construct a matrix to diagonalize not only the matrix [P] or matrix [Q] but diagonalize both of them simultaneously. This is obvious when we rewrite these two matrices

$$12[Q] + [P] - 12[I] = 0, \text{ or } [Q] = [I] - [P]/12. \quad (4.13)$$

Therefore, an orthogonal matrix [T] which diagonalizes [P] can also diagonalize [Q]. More details of this procedure are given in the Appendix F.

Multiplying eq. (4.12) with matrix [T] and its transpose from the right and the left sides, respectively, leads to a set of decoupled ordinary differential equations

$$\frac{d^2 \bar{V}}{dy^2} + \left\{ (k^2 - \beta^2) - \frac{\bar{\delta}^2}{h^2} \right\} \bar{V} = 0, \quad (4.14)$$

which can be solved analytically, where \bar{V} (\bar{V}^e, \bar{V}^h) = [T] $\bar{\phi}$ is the transformed potential and [$\bar{\delta}$] a diagonal matrix with elements

$$\bar{\delta}_k^2 = \frac{\lambda_k^2}{\mu_k^2} = \frac{12(1 - \cos \varphi_k)}{(5 + \cos \varphi_k)} = \frac{12}{1 - 3(\csc \varphi_k / 2)^2}. \quad (4.15)$$

4.2.2 Continuity conditions at interfaces

The continuity condition at any interface between region k and region $k+1$ requires that the tangential field components at the interface of two regions (Figure 4.1) are matched

$$E_{z,k} = E_{z,k+1}, E_{x,k} = E_{x,k+1}, H_{z,k} = H_{z,k+1} + J_x, H_{x,k} = H_{x,k+1} - J_z.$$

The tangential fields can be expressed by the scalar potentials (eq.(4.1))

$$E_t = \frac{1}{\epsilon_r k_0 - \beta^2} (j\omega\mu\nabla\times\bar{\phi}_h + j\beta\nabla\bar{\phi}_e), \quad H_t = \frac{1}{\epsilon_r k_0 - \beta^2} (j\omega\epsilon\nabla\times\bar{\phi}_e - j\beta\nabla\bar{\phi}_h),$$

where the differential operator is tangential to the interface. From the above equations, one obtains

$$\text{Ex: } \frac{\beta}{\omega\epsilon_0} \frac{\partial}{\partial x} \left(\frac{\phi_{e,k}}{\epsilon_{r,k}} - \frac{\phi_{e,k+1}}{\epsilon_{r,k+1}} \right) = \frac{\partial}{\partial y} (\phi_{h,k+1} - \phi_{h,k}), \quad (4.16)$$

$$\text{Ez: } \frac{1}{\epsilon_{r,k}} (\epsilon_{r,k} k_0^2 - \beta^2) \phi_{e,k} = \frac{1}{\epsilon_{r,k+1}} (\epsilon_{r,k+1} k_0^2 - \beta^2) \phi_{e,k+1}, \quad (4.17)$$

$$\text{Hx: } \frac{\partial}{\partial y} (\phi_{e,k} - \phi_{e,k+1}) = \frac{\beta}{\omega\mu} \frac{\partial}{\partial x} (\phi_{h,k+1} - \phi_{h,k}) - J_z, \quad (4.18)$$

$$\text{Hz: } (\epsilon_{r,k} k_0^2 - \beta^2) \phi_{h,k} = (\epsilon_{r,k+1} k_0^2 - \beta^2) \phi_{h,k+1} - j\omega\mu J_x. \quad (4.19)$$

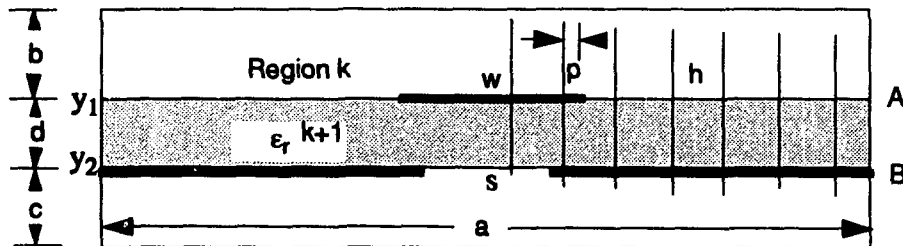


Figure 4.1 MoL calculation of a microstrip-slot line with two dielectric interfaces A and B, p is the edge parameter to satisfy the edge condition.

The derivatives with respect to x can be found from the central finite differences between two lines, for instance

$$\frac{\beta}{\omega\epsilon_0} \left\{ \frac{(\phi_{e,k,i+1} - \phi_{e,k,i})/h - r_{k,i}^e}{\epsilon_{r,k}} - \frac{(\phi_{e,k+1,i+1} - \phi_{e,k+1,i})/h - r_{k+1,i}^e}{\epsilon_{r,k+1}} \right\} = \frac{d}{dy} (\phi_{h,k+1,i} - \phi_{h,k,i}), \quad (4.20)$$

$$\begin{aligned} \frac{\beta}{\omega\mu} \left\{ \frac{(\phi_{h,k,i+1} - \phi_{h,k,i})}{h} - r_{k,i}^h - \frac{(\phi_{h,k+1,i+1} - \phi_{h,k+1,i})}{h} - r_{k+1,i}^h \right\} - J_{zi} \\ = \frac{d}{dy} (\phi_{e,k,i} - \phi_{e,k+1,i}). \end{aligned} \quad (4.21)$$

The discretization error can be found as (Appendix F)

$$r_{k,k+1,i}^{e,h} = \frac{h^2}{4!} \frac{\partial^3}{\partial x^3} \phi_{k,k+1,i}^{e,h} + \frac{h^4}{2^4 5!} \frac{\partial^5}{\partial x^5} \phi_{k,k+1,i}^{e,h} + o(h^6). \quad (4.22)$$

It is obvious that the above discretization accuracy is at best of second order. To improve the discretization accuracy to $o(h^4)$ three neighboring lines must be combined in the discretized scheme. (4.20) and (4.21) then read as

$$\begin{aligned} \frac{\beta}{\omega\epsilon_0} \left\{ \frac{(\phi_{e,k,i+1} - \phi_{e,k,i})/h - s_{k,i}^e}{\epsilon_{r,k}} - \frac{(\phi_{e,k+1,i+1} - \phi_{e,k+1,i})/h - s_{k+1,i}^e}{\epsilon_{r,k+1}} \right\} \\ = \frac{1}{24} \frac{d}{dy} \left\{ (\phi_{h,k+1,i+1} - \phi_{h,k,i+1}) + 22(\phi_{h,k+1,i} - \phi_{h,k,i}) + (\phi_{h,k+1,i-1} - \phi_{h,k,i-1}) \right\} \end{aligned} \quad (4.23)$$

$$\begin{aligned} \frac{\beta}{\omega\mu} \left\{ \frac{(\phi_{h,k,i+1} - \phi_{h,k,i})}{h} - s_{k,i}^h - \frac{(\phi_{h,k+1,i+1} - \phi_{h,k+1,i})}{h} - s_{k+1,i}^h \right\} - J_{zi} \\ = \frac{1}{24} \frac{d}{dy} \left\{ (\phi_{e,k+1,i+1} - \phi_{e,k,i+1}) + 22(\phi_{e,k+1,i} - \phi_{e,k,i}) + (\phi_{e,k+1,i-1} - \phi_{e,k,i-1}) \right\} \end{aligned} \quad (4.24)$$

Developing this equation in a Taylor series (Appendix F) leads to the expression

$$s_{k,k+1,i}^{e,h} = \frac{17h^4}{2 \times 4! \times 5!} \frac{\partial^5}{\partial x^5} \phi_{k,k+1,i}^{e,h} + o(h^6), \quad (4.25)$$

which clearly shows that the discretization accuracy of the modified MoL is now of 4th order.

By making use of the difference operator notation the above equations can be written in matrix form

$$\frac{\beta}{\omega \epsilon_0} [D] \begin{pmatrix} \bar{\Phi}_{e,k} - \bar{\Phi}_{e,k+1} \\ \bar{\epsilon}_{r,k} - \bar{\epsilon}_{r,k+1} \end{pmatrix} = [Q_x] \frac{d}{dy} (\bar{\Phi}_{h,k+1} - \bar{\Phi}_{h,k}), \quad (4.26)$$

$$\frac{\beta}{\omega \mu} [D]^t (\bar{\Phi}_{h,k} - \bar{\Phi}_{h,k+1}) + [Q_x] J_z = [Q_x] \frac{d}{dy} (\bar{\Phi}_{e,k+1} - \bar{\Phi}_{e,k}), \quad (4.27)$$

Matrices $[D]$ and $[D]^t$ are given in eq. (4.6), and $[Q_x]$ is a new matrix as a result of the modified MoL approach

$$[Q_x] = \frac{1}{24} \begin{bmatrix} q_{x1} & 1 & 0 & \dots & 0 & 0 \\ 1 & 22 & 1 & \dots & 0 & 0 \\ 0 & 1 & 22 & \dots & 0 & 0 \\ \dots & \dots & \dots & \dots & \dots & \dots \\ 0 & 0 & 0 & \dots & 22 & 1 \\ 0 & 0 & 0 & \dots & 1 & q_{x2} \end{bmatrix}.$$

The coefficients q_{xi} ($i=1$ or 2) depend on the lateral boundary conditions

$$q_{xi} = \begin{cases} 22, & i=1 \text{ or } 2; \text{ for the Dirichlet (D) boundary conditions.} \\ 23, & i=1 \text{ or } 2; \text{ for the Neumann (N) boundary conditions.} \end{cases}$$

Also here it is found that the matrix $[D]$ and matrix $[Q_x]$ can be diagonalized by the same matrix $[T]$ because in analogy to eq.(4.13) we find that $24[Q_x] = 24[I] - [D]$. Hence, analytical solutions can be found since only diagonal matrices are involved after the transformation. Elements of all the matrices can be stored as one-dimensional arrays. All inverses of matrices are equivalent to their transpose.

4.2.3 Edge condition

In the above error analysis it is assumed that the higher order partial derivatives of the potential functions are continuous. However, the field behavior is singular at the

edges of the conductor. The fields must satisfy the edge condition which, in the conventional MoL, minimizes the discretization error if the last line on the conductor is $p=0.265h$ away from the edge [56]. This is usually approximated by $p=0.25h$. Since the MoL scheme has been modified to a higher order error term, the edge condition must be modified accordingly. The edge condition requires (when $r \rightarrow 0$):

$$\phi_e \propto r^{1/2} \sin \theta/2, \phi_h \propto r^{1/2} \cos (\theta/2), \quad (4.28)$$

where the point (r, θ) is described in polar coordinates. When $r \rightarrow 0$, the electromagnetic fields have quasi-static characteristic, and the potentials satisfy [56]

$$\frac{\partial^2 \phi}{\partial x^2} + \frac{\partial^2 \phi}{\partial y^2} = 0. \quad (4.29)$$

Substituting (4.28) into (4.29), and using the discretization scheme (4.10) at point i , yields

$$\frac{1}{24} \{ p^{-3/2} + 10(1-p)^{-3/2} + (2-p)^{-3/2} \} + 2 \{ (1-p)^{1/2} + (2-p)^{1/2} \} = 0. \quad (4.30)$$

From this equation, the optimum distance in the modified MoL approach is found to be approximately $p=0.30$ (Fig. G.1).

4.3 Numerical results

Eq. (4.12) can be easily solved analytically for each layer of the structure. The solution has a form similar to that of the transmission line equation. Thus, a relationship between the potential functions at any two positions within a homogeneous subregion is given

$$\begin{bmatrix} \nabla^{e,h} \\ \frac{d}{dy} \nabla^{e,h} \end{bmatrix} \Big|_{y_1} = \begin{bmatrix} \cosh \kappa (y_1 - y_2) & \frac{1}{\kappa} \sinh \kappa (y_1 - y_2) \\ \kappa \sinh \kappa (y_1 - y_2) & \cosh \kappa (y_1 - y_2) \end{bmatrix} \begin{bmatrix} \nabla^{e,h} \\ \frac{d}{dy} \nabla^{e,h} \end{bmatrix} \Big|_{y_2}, \quad (4.31)$$

where

$$\kappa_j^{k+1} = \sqrt{\bar{d}_{x,j}/h^2 - (\epsilon_r^{k+1} k_0^2 - \beta^2)}, j=1,2,3,\dots,N.$$

where the elements of the diagonal matrix $\bar{d}_{x,j}$ are the eigenvalues of the transformation matrix [T].

From (4.31), the potential functions can be transformed from one interface to another. Thus, one can obtain a set of equations which contains discrete values of the transformed potential functions and discretized current distributions at the interfaces. Finally, all the transformed potential functions and tangential fields can be transformed back into the original domain by the transformation matrix [T]. Therefore, this set of equations can be written as the relationship between the tangential fields and surface current intensities at interfaces. For example, assuming a structure of three layers yields

$$[Z] \begin{bmatrix} E_z^A \\ E_x^A \\ J_z^B \\ J_x^B \end{bmatrix} = \begin{bmatrix} J_z^B \\ J_x^B \\ E_z^B \\ E_x^B \end{bmatrix}, \quad (4.32)$$

where the capital letters *A* and *B* denote the interfaces *A* and *B* (Figure 4.1), respectively. By making use of the zero tangential field on metal strips and zero current distribution in the slots, a reduced determinant equation is obtained

$$[Z]_{red} \begin{bmatrix} E_{z,slot}^A \\ E_{x,slot}^A \\ J_{z,strip}^B \\ J_{x,strip}^B \end{bmatrix} = 0, \quad (4.33)$$

for which the nontrivial solution requires

$$\det([Z]_{red}) = 0. \quad (4.34)$$

Now only the number of lines on the strips of interface B and in the slots of interface A (Figure 4.1) determine the size of the reduced eigenvalue matrix $[Z]_{red}$. The eigenvector is the reduced part of the current density distribution at interface B and of the tangential electric field at interface A , respectively.

In summary, the difference between the original MoL and the modified scheme presented here is that: a three-line discretization of the Helmholtz equations, the field continuity equations and the edge condition has been introduced leading to an $o(h^4)$ accuracy. After these modifications, the remaining numerical procedure of the modified MoL algorithm is the same as that in the original scheme [55]. However, the accuracy and convergence rate are improved greatly. Therefore, a smaller number of lines and consequently smaller matrix sizes are needed.

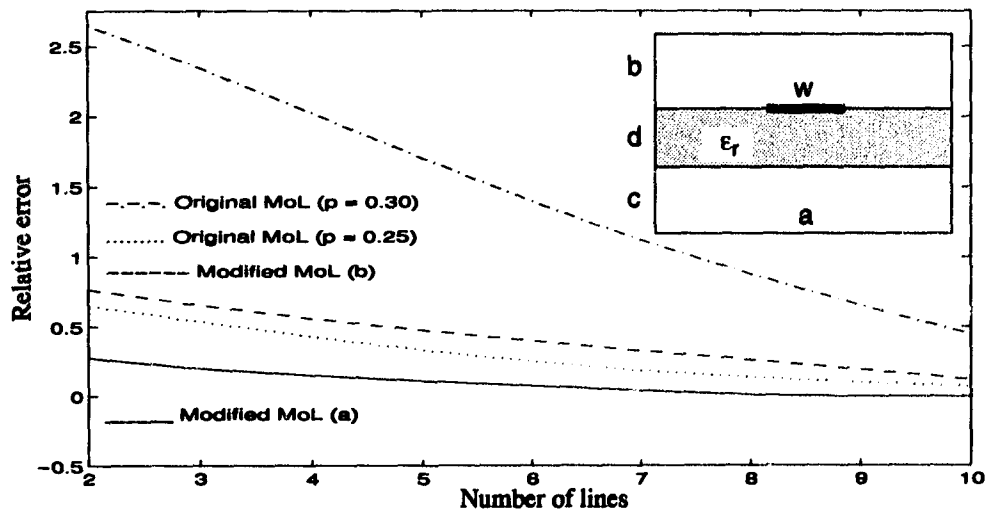


Figure 4.2. Calculation of a microstrip line, $w=d=1.25\text{mm}$, $a=b=c=12.5\text{mm}$, $\epsilon_r=8.875$, edge parameter $p = 0.30$ (case a), 0.25 (case b).

To test the new algorithm, a microstrip line is simulated and results are compared with results from the conventional MoL scheme. Fig. 4.2 clearly illustrates the improvements of the modified MoL. With only 4 lines on the strip the modified MoL achieves a

better accuracy than the conventional MoL with 8-10 lines. However, the optimum edge parameter in the modified MoL ($p = 0.30$, ph is the distance between the first discrete line and the metal edge, h is the discretization step) is slightly different from that in the original one ($p = 0.25$). The simulation of a microstrip line with tuning septums (Fig. 4.3) also confirms this conclusion.

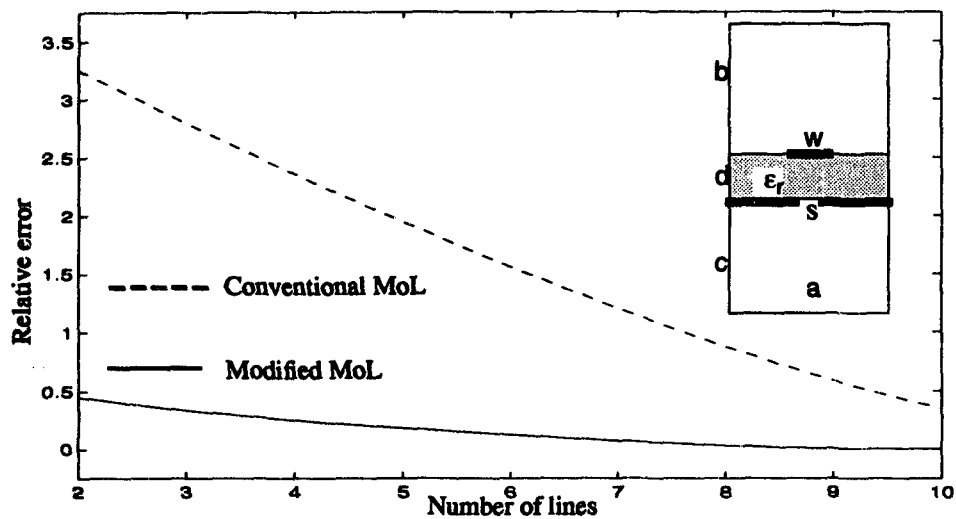


Figure 4.3 Calculation of a microstrip-slot line with tuning septums, $w=d=1.25\text{mm}$, $a=b=c=12.5\text{mm}$, $s=1\text{mm}$, $\epsilon_r=8.875$.

Chapter 5

Cylindrical method of lines

The method of lines can also be applied to solve Helmholtz equations in cylindrical coordinates. By discretizing the angular space direction, also here the Helmholtz equation becomes a set of ordinary differential equations which can be solved analytically in radial direction after an orthogonal transformation. An analytical form of the transformation matrix is derived. The method is suitable for the analysis of not only cylindrical structures but also arbitrary cross sections with homogeneous and inhomogeneous propagation media.

5.1 Introduction

Characterization of various homogeneous and inhomogeneous waveguides with cylindrical cross section is important for cylindrical multiconductor transmission lines or integrated circular waveguide components. The design of passive circuits on curved surfaces is not a simple problem due to the fact that structural details are frequently described by a mixture of cylindrical and cartesian coordinates. The problem is difficult with most existing numerical approaches, especially when there is no angular symmetry.

In the following the MoL procedure introduced in the previous chapters will be adopted for cylindrical coordinates. Most applications of the MoL are so far only for structures in a rectangular coordinate system. Although the method of lines in Cartesian coordinates has been applied also to curvilinear structures [67] by using a staircase approximation of the cylindrical boundary, this approach has a limited accuracy. For application of the MoL directly in cylindrical coordinates, very little information has been pub-

lished. Thorburn, Agostron, and Tripathi [63] discretized the r -variables in the Helmholtz equations with circular lines and successfully solved the remaining equations along the θ -direction. However, they did not elaborate on how to solve the problem at $r=0$ (center of the coordinate system) for the general case with no symmetry planes. In general, the boundary condition along $r=a$ (refer to Fig. 1 in [63]) is an electric wall, but the condition at $r=0$ is unknown except in symmetric structures. In asymmetric structures the transformation matrix to decouple the coupling differential equations at different lines requires knowledge of the boundary condition at $r=0$. To solve this problem, the authors of [66,95,96] suggested to discretize the θ -variable by radial straight lines. The authors stated that the same transformation matrices $[T]$, the difference operator $[P]$, and the eigenvalues $[\lambda]$ found for Cartesian coordinates can be used for cylindrical coordinates. Although the use of radial lines to discretize the angular space direction is a good idea and will be used in this chapter, we found that contrary to the statement in [66] for the case of asymmetric structures the finite difference operator $[P]$ in cylindrical coordinates is generally different from the one in Cartesian systems, and so are $[T]$ and $[\lambda]$. The main difficulty to overcome here is that in polar coordinates, when discretizing the structures with N lines along the radial direction, periodic boundary conditions must be satisfied with $\phi(r, \theta_k) = \phi(r, 2\pi + \theta_k)$ ($k=1, 2, \dots, N$) (Fig. 5.2). Due to the periodicity of the solution, the transformation matrices developed for Cartesian coordinates [55] are no longer applicable for the general cases.

In the following it will be shown how the general MoL algorithm can be applied to cylindrical structures.

Although the following theoretical derivations are only related to two-dimensional discontinuities, the method can be extended to spatially three-dimensional discontinuities by discretizing also the z -variable instead of assuming $\gamma=j\beta$. This topic will be discussed in next chapter.

5.2 Semianalytical solution of Helmholtz equation

The general case of a multilayered dielectric cylindrical microstrip transmission line is treated first (Fig. 5.1). Simpler cases, like waveguide structures with homogeneous

dielectric can be easily derived from the general case. The electromagnetic field in the homogeneous subregions can be derived from two independent scalar potential functions. For a two-dimensional eigenvalue problem in a cylindrical coordinate system the scalar potentials $\phi_{e,h} \exp\{j\omega t - \gamma z\}$ (assuming $\gamma = j\beta$) are directly proportional to the field components E_z and H_z . Both satisfy the Helmholtz equation in polar coordinates

$$\frac{1}{r} \frac{\partial}{\partial r} \left(r \frac{\partial \phi}{\partial r} \right) + \frac{\partial^2 \phi}{r^2 \partial \theta^2} + (k^2 - \beta^2) \phi = f(r, \theta), \quad (5.1)$$

and the boundary conditions depending on the structure and modes we are interested in ($k^2 = \omega^2 \mu \epsilon$). The electromagnetic field components are then obtained from eq. (4.1).

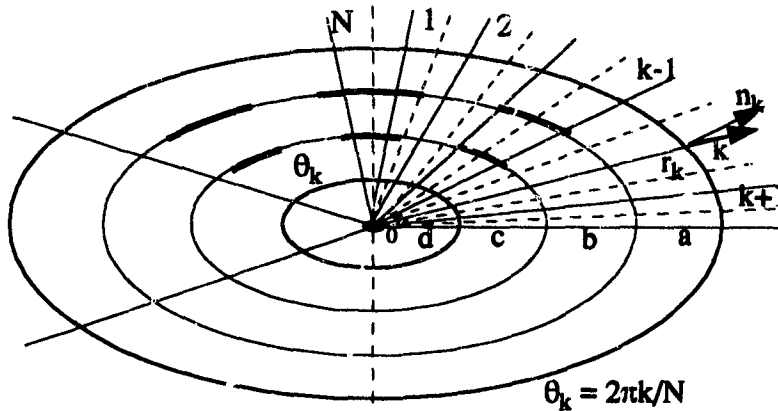


Figure 5.1 MoL discretization in a cylindrical coordinate system

Since the hybrid field problem can not be solved analytically for the whole region, the calculation domain is discretized along the angular direction by an ensemble of straight lines along the r -direction. The uniformly discretized θ -variable reads then

$$\theta_k = \theta_1 + (k-1)h = \frac{2\pi k}{N}, \quad k=1,2,\dots,N, \quad (5.2)$$

with N the number of discretization lines, and h being the angular spacing between the lines. For known reasons, the discretization lines for the electric potential function ϕ_e are shifted with respect to the magnetic lines, ϕ_h by a distance of half a discretization step, $h/2$.

Using the central finite differences

$$\left. \frac{\partial \phi_{e,h}}{\partial \theta} \right|_{k+0.5} = \frac{\phi_{e,h}|_{k+1} - \phi_{e,h}|_k}{h} + o(h^2), \quad (5.3)$$

($h=2\pi/N$), the above equation can be written in matrix form

$$h \frac{\partial \bar{\Phi}_e}{\partial \theta} \approx [D] \bar{\Phi}_e, \quad h \frac{\partial \bar{\Phi}_h}{\partial \theta} \approx -[D]^t \bar{\Phi}_h. \quad (5.4)$$

The first order finite difference operator is an N by N bi-diagonal matrix

$$[D] = \begin{bmatrix} -1 & 1 & 0 & \dots & 0 & 0 \\ 0 & -1 & 1 & \dots & 0 & 0 \\ 0 & 0 & -1 & \dots & 0 & 0 \\ \dots & \dots & \dots & \dots & \dots & \dots \\ 0 & 0 & 0 & \dots & -1 & 1 \\ 1 & 0 & 0 & \dots & 0 & -1 \end{bmatrix}, \quad -[D]^t = \begin{bmatrix} -1 & 0 & 0 & \dots & 0 & 1 \\ 1 & -1 & 0 & \dots & 0 & 0 \\ 0 & 1 & -1 & \dots & 0 & 0 \\ \dots & \dots & \dots & \dots & \dots & \dots \\ 0 & 0 & 0 & \dots & -1 & 0 \\ 0 & 0 & 0 & \dots & 1 & -1 \end{bmatrix}, \quad (5.5)$$

where t denotes the transpose of a matrix. It should be noted that the operator [D] used here for the periodic boundary condition in cylindrical coordinates is similar to that in Cartesian coordinates given by Shultz and Pregla in [55,60]. The central finite difference scheme is used again to calculate the second order partial differential operator from the first order one as

$$h^2 \frac{\partial^2 \bar{\Phi}_e}{\partial \theta^2} \Big|_i = h \frac{\partial}{\partial \theta} \left(h \frac{\partial \bar{\Phi}_e}{\partial \theta} \right) \Big|_i = h \frac{h \frac{\partial \bar{\Phi}_e}{\partial \theta} \Big|_{i+0.5} - h \frac{\partial \bar{\Phi}_e}{\partial \theta} \Big|_{i-0.5}}{h} = (-[D]^t) [D] \bar{\Phi}_e = [P] \bar{\Phi}_e, \quad (5.6)$$

$$h^2 \frac{\partial^2 \bar{\Phi}_h}{\partial \theta^2} \Big|_i = h \frac{\partial}{\partial \theta} \left(h \frac{\partial \bar{\Phi}_h}{\partial \theta} \right) \Big|_i = h \frac{h \frac{\partial \bar{\Phi}_h}{\partial \theta} \Big|_{i+0.5} - h \frac{\partial \bar{\Phi}_h}{\partial \theta} \Big|_{i-0.5}}{h} = [D] (-[D]^t) \bar{\Phi}_h = [P] \bar{\Phi}_h, \quad (5.7)$$

where $[P]=[D](-[D]^t)=(-[D]^t)[D]$, and

$$[P] = \begin{bmatrix} 2 & -1 & 0 & \dots & 0 & 0 & -1 \\ -1 & 2 & -1 & \dots & 0 & 0 & 0 \\ \dots & \dots & \dots & \dots & \dots & \dots & \dots \\ \dots & \dots & \dots & \dots & \dots & \dots & \dots \\ 0 & 0 & 0 & \dots & -1 & 2 & -1 \\ -1 & 0 & 0 & \dots & 0 & -1 & 2 \end{bmatrix}. \quad (5.8)$$

Introducing eq.(5.6) and (5.7) into eq.(5.1) yields for each uniform and source-free region a set of ordinary differential equations which are coupled with each other:

$$r \frac{d}{dr} \left(r \frac{d\bar{\Phi}}{dr} \right) + k_c^2 r^2 \bar{\Phi} - \frac{[P]\bar{\Phi}}{h^2} = \bar{\gamma}, \bar{\gamma} = \frac{h^2}{12} \frac{\partial^4 \bar{\Phi}}{\partial \theta^4} + \frac{h^4}{360} \frac{\partial^6 \bar{\Phi}}{\partial \theta^6} + o(h^6) \quad (5.9)$$

where $k_c^2 = k^2 - \beta^2$. It is found that the condition of periodicity makes the second order difference operator $[P]$ have a form of eq. (5.8) which is slightly different from the one in Cartesian coordinates in [55]. $[T]$ and $[\lambda]$ will be slightly different too. The structures in [55,60] support waveguide modes which satisfy the periodic condition but with a phase delay along the wave propagation direction (z -direction). However, in cylindrical coordinates, the field components satisfy the periodic condition without any phase delay because any physical characteristic repeats itself after rotating 360° . This periodic condition can be considered as a special periodic condition. Therefore, the task is to find an orthogonal matrix to transform the variables in order to decouple the above equation and find an analytical solution for it in radial direction. It is found that the matrix $[P]$ can be separated again into two matrices as $[P] = 2[I] - [P_0]$, where $[I]$ is an identity matrix and $[P_0]$ is of a form

$$[P_0] = \begin{bmatrix} 0 & 1 & 0 & \dots & 0 & 0 & 1 \\ 1 & 0 & 1 & \dots & 0 & 0 & 0 \\ \dots & \dots & \dots & \dots & \dots & \dots & \dots \\ \dots & \dots & \dots & \dots & \dots & \dots & \dots \\ 0 & 0 & 0 & \dots & 1 & 0 & 1 \\ 1 & 0 & 0 & \dots & 0 & 1 & 0 \end{bmatrix}. \quad (5.10)$$

Matrix $[P_0]$ can be factorized by an orthogonal matrix $[T]$ as

$$[P_0] = [T][\lambda][T]^t, \quad (5.11)$$

where $[T]^t = [T]^{-1} = [T]$, and $[T][I][T]^t = [I]$. The elements of $[T]$ and its eigenvalues are derived analytically as follows

$$T_{ij} = \{ \cos \alpha_{ij} + \sin \alpha_{ij} \} / \sqrt{N}, \quad \lambda_k = 2 \cos \alpha_k, \quad (5.12)$$

where $\alpha_{ij} = hij$, $h = 2\pi/N$, $\alpha_k = hk$, ($i, j, k = 1, 2, \dots, N$). Multiplying $[P]$ in eq.(5.8) with $[T]$ and $[T]^t$, respectively, yields $2 - \lambda_k^2 = 2(1 - \cos \alpha_k) = \mu_k^2$, and the set of coupled Helmholtz equations in eq. (5.8) can be decoupled into a set of independent ordinary differential equations of Bessel form

$$\frac{d}{dr} \left(r \frac{d\varphi_k}{dr} \right) + \left(k_c^2 - \frac{\mu_k^2}{r^2} \right) \varphi_k = 0, \quad \mu_k = \frac{2 \sin(\alpha_k/2)}{h}, \quad (5.13)$$

where φ_k ($k=1, 2, 3, \dots, N$, $\bar{\varphi} = [\varphi_1, \varphi_2, \dots, \varphi_N] = [T]\bar{\phi}$) is the transformed potential function in analogy to \bar{V} in Cartesian coordinates.

In every uniform region, a solution of eq. (5.13) may be written as a superposition of Bessel and Neumann functions of μ_k -order

$$\varphi_k = A_k Y_{\mu_k}^{(1)}(k_c r) + B_k Y_{\mu_k}^{(2)}(k_c r), \quad (5.14)$$

where A_k and B_k are constants. The Bessel functions Y_{μ_k} can be either the first kind of Bessel functions J_{μ_k} , the second kind of Bessel functions (Neumann functions N_{μ_k}), or the third kind of Bessel functions (the first and second kind of Hankel functions $H_{\mu_k}^{(1)}$ and $H_{\mu_k}^{(2)}$). The selection of these functions depends on the individual applications. It should be noted that at $r=0$ (the origin), B_k must be zero since N_{μ_k} and $H_{\mu_k}^{(2)}$ will be approaching infinity. For a region extended to infinity (open structure), A_k must be zero since the first kind of Hankel function $H_{\mu_k}^{(1)}$ is not bounded.

After eq. (5.13) is solved in every uniform region (non-uniform region can also be solved by using a Sturm-Liouville equation), the potentials $\bar{\phi}$ can be obtained by an inverse transformation $\bar{\phi}=[T]^{-1}\bar{\varphi}=[T]^t\bar{\varphi}=[T]\bar{\varphi}$ (note: the inverse and transpose of [T] are avoided since they are equivalent to the matrix [T] itself) for ϕ_e and ϕ_h respectively. As a final result the telegraphist equation in polar coordinates is obtained when a combination of the first kind of Bessel functions J_{μ_k} and the second kind of Bessel functions (Neumann functions N_{μ_k}) are used

$$\begin{aligned} \left[\begin{array}{c} \varphi_k(k_c r_1) \\ \frac{1}{k_c} \frac{d\varphi_k(k_c r_1)}{dr} \end{array} \right] &= \left[w \left(Y_{\mu_k}^{(1)}(k_c r_1), Y_{\mu_k}^{(2)}(k_c r_1) \right) \right] \left[w \left(Y_{\mu_k}^{(1)}(k_c r_2), Y_{\mu_k}^{(2)}(k_c r_2) \right) \right]^{-1} \\ &\times \left[\begin{array}{c} \varphi_k(k_c r_2) \\ \frac{1}{k_c} \frac{d\varphi_k(k_c r_2)}{dr} \end{array} \right], [w(y_1, y_2)] = \begin{bmatrix} y_1 & y_2 \\ y_1' & y_2' \end{bmatrix} \end{aligned} \quad (5.15)$$

where y_1 and y_2 denote the Bessel functions in the above equation, and the prime denotes a derivative with respect to r . This equation links the transformed potential as well as its derivatives at the two boundaries of a homogeneous subregion. To link the fields between homogeneous subregions, the tangential field continuity condition must be applied.

Since the calculation of various special functions are the most time consuming part in the MoL scheme, two aspects in practical programming may affect the efficiency and accuracy. One is to use the variables in vector and matrix form during programming as much as possible in order to take advantage of the vector calculation features, especially for MatlabTM programming. The other is to utilize any possible recursive formula instead of the direct calculation of the functions. For example, to calculate the columns of matrix [T], we can use the following recurrence relationship

$$T_{i,j+2} = \lambda_i T_{i,j+1} - T_{i,j}, j=0,1,2,3,\dots,N-2, \quad (5.16)$$

$$T_{i,0} = T_{i,N} = \frac{1}{\sqrt{N}}, T_{i,1} = \frac{1}{\sqrt{N}} (\cos ih + \sin ih). \quad (5.17)$$

5.3 Eigenvalue equation of inhomogeneous waveguides

After the Helmholtz equations are solved in each uniform region, we need to match the fields at the interfaces between the uniform regions in order to solve the whole structure. The tangential fields at interfaces between neighboring regions are obtained from ϕ_e and ϕ_h . For example, for the continuity condition of E_θ , we have

$$\frac{\beta}{\omega \epsilon_0} \left(\frac{\partial \phi_e^I}{\epsilon_{r,I} \partial \theta} - \frac{\partial \phi_e^{II}}{\epsilon_{r,II} \partial \theta} \right) = r \frac{\partial \phi_h^{II}}{\partial r} - r \frac{\partial \phi_h^I}{\partial r}.$$

When we discretize the potential functions in each region and denote the discretized potentials by vectors, we can obtain the following relationship which is useful for transforming the fields between interfaces

$$\frac{\beta}{\omega \epsilon_0} [D] \left(\frac{\bar{\phi}_e^I}{\epsilon_{r,I}} - \frac{\bar{\phi}_e^{II}}{\epsilon_{r,II}} \right) = rh \left(\frac{d\bar{\phi}_h^{II}}{dr} - \frac{d\bar{\phi}_h^I}{dr} \right).$$

Multiplying $[T]^I$ and $[T]$ from the left and right sides respectively, the above equations are diagonalized. Similarly, we obtain the continuity conditions for the other field components. Finally, transforming those potentials into the conductor interface (Fig. 5.2) and using the boundary conditions of tangential electric fields on the conductor surface, the relationship between the tangential fields E_z , E_θ and the surface current intensities J_z , J_θ at interfaces can be obtained. Now all the transformed potential functions and the discretized tangential fields can be transformed back to the original domain, which yields

$$[Z] \begin{bmatrix} E_z^I & E_\theta^I & J_z^{II} & J_\theta^{II} \end{bmatrix}^t = \begin{bmatrix} J_z^I & J_\theta^I & E_z^{II} & E_\theta^{II} \end{bmatrix}^t. \quad (5.18)$$

The capital letters I and II denote the adjacent regions I and II respectively.

By using the condition of zero tangential fields $\bar{E}_{z,\theta}=0$ on metal strips and zero current distribution on the dielectric slots $\bar{J}_{z,\theta}=0$, a reduced determinantal equation is obtained

$$[Z]_{red} \begin{bmatrix} E'_{z,slot} & E'_{\theta,slot} & J''_{z,strip} & J''_{\theta,strip} \end{bmatrix} = 0. \quad (5.19)$$

A nontrivial solution to eq. (5.19) requires the determinant of the reduced matrix $[Z]_{red}$ to be zero:

$$\det \{ [Z]_{red} \} = 0. \quad (5.20)$$

5.4 Cutoff frequencies in homogeneous waveguides

For inhomogeneous problems (i.e. transmission line with multilayered dielectrics), the discretized field continuity conditions must be satisfied at each interface. For a homogeneous waveguide (e.g. circular, elliptic hollow waveguides, or other complex contour hollow waveguides), however, a simplified procedure can be used. Taking an arbitrary contour hollow waveguide as an example (Fig. 5.2), the finite field values at $r=0$ require $B_k=0$. Assuming ideal conductivity on the contour leads to

$$[T][A_k J_{mk}] = 0, \quad (5.21)$$

for TM modes, where r_k is the radius of the k -th discretization line. Therefore, for any complex contour hollow waveguide (Fig. 5.2) one needs only to input the radius r_k of the contour ($k=1,2,3,\dots,N$) at each discretization line. The cutoff frequencies for such an arbitrary structure are then obtained from

$$\det \{ [T][J_{mk}] \} = 0, \quad (5.22)$$

with non-zero coefficients $\bar{A} = [A_1, A_2, A_3, \dots, A_N]^t$. $J_{mk} = J_{\mu_k}(k_c r_k)$ (r_k is on the conductor contour) is the μ_k -order Bessel function of $k_c r_k$. This eigenvalue equation will give all the cutoff wavenumbers for TM modes.

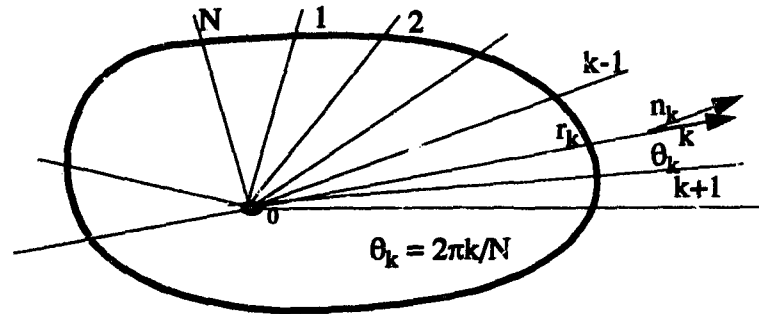


Figure 5.2 CMoL discretization for a waveguide with arbitrary contour

Similarly, TE modes can be found if we substitute the $J_{mk} = J_{\mu k}(k_c r_k)$ with

$$J_{mk}(k_c r_k) = \frac{dJ_{\mu k}(k_c r_k)}{dn_k}, \quad (5.23)$$

where, \bar{r}_k and \bar{n}_k are, respectively, the unit vectors along the k -th radial line and the outwards normal vector to the contour (Fig. 5.2). For TE modes, one needs to input an extra parameter, the inner product of the unit normal vector of the contour and the unit normal vector of the discretization lines.

The eigenvalue equation discussed above for homogeneous structures is simpler and quicker to solve than for an inhomogeneous cross-section. Symmetry of the structure may also be used to reduce the computational effort, but the transformation matrix must be modified accordingly.

5.5 Improved accuracy for the cylindrical MoL

5.5.1 Helmholtz equation

As shown for the Cartesian MoL, to reduce the discretization error also in the cylindrical MoL, the three neighboring lines are utilized and the appropriate coefficients are chosen to cancel the lower order error yielding a fourth order accuracy. The discretized Helmholtz equations in cylindrical coordinates reads as

$$[Q] r \frac{d}{dr} \left(r \frac{d\Phi}{dr} \right) + k_c^2 r^2 [Q] \Phi - \frac{[P] \Phi}{h^2} = \gamma, \bar{\gamma} = -\frac{h^4}{2 \times 5!} \frac{\partial^6 \Phi}{\partial \theta^6} + o(h^6),$$

where, [P] is the same as in eq. (5.8), and the new matrix [Q] is a tridiagonal one

$$[Q] = \frac{1}{12} \begin{bmatrix} 10 & 1 & 0 & \dots & 0 & 0 & 1 \\ 1 & 10 & 1 & \dots & 0 & 0 & 0 \\ \dots & \dots & \dots & \dots & \dots & \dots & \dots \\ \dots & \dots & \dots & \dots & \dots & \dots & \dots \\ 0 & 0 & 0 & \dots & 1 & 10 & 1 \\ 1 & 0 & 0 & \dots & 0 & 1 & 10 \end{bmatrix}. \quad (5.24)$$

The problem now is that eq. (5.24) is a set of equations coupled not only through [P] but also [Q]. In order to solve eq. (5.24) analytically, we must diagonalize [P] and [Q] at the same time with the same orthogonal matrix. We find that such an orthogonal matrix [T] exists

$$T_{ij} = \sqrt{\frac{5 + \cos \alpha_j}{2N}} \{ \sin \alpha_{ij} + \cos \alpha_{ij} \}, \quad \alpha_j = 2\pi j/N, \quad i, j=1,2,3,\dots,N. \quad (5.25)$$

where α_{ij} are α_j are the same as that in eq. (5.12). Actually, matrix [T] which diagonalizes matrices [P] and [Q] simultaneously is not unique. When we carefully study the new matrix [Q], we can further verify the existence of the orthogonal matrix [T]. In fact, the matrix [Q] can be separated as follows

$$[Q] = \frac{5}{6} [I] + \frac{1}{12} [P_0], \quad (5.26)$$

where [I] is an identity matrix, [P₀] is exactly the same as in eq. (5.10). Since [P₀] can be diagonalized by [T], the matrix [Q] is diagonalized too by the same [T] as

$$[T] [Q] [T] = \frac{5}{6} + \frac{1}{12} \lambda_k. \quad (5.27)$$

λ_k is given already in (5.9). The set of decoupled ordinary differential equations can be solved analytically in r-direction as shown before.

5.5.2 Field continuity equation

In order to take full advantage of the $o(h^4)$ accuracy, the scheme must also be applied to the continuity condition. Combining every three neighboring lines for the field

continuity conditions with appropriate coefficients, we find that the $o(h^2)$ -order errors are cancelled, and the accuracy will be of $o(h^4)$

$$\gamma = -\frac{17h^4}{2 \times 4! \times 5!} \frac{\partial^5 \Phi^{I,II}}{\partial \theta^5} + o(h^6). \quad (5.28)$$

Therefore the field continuity condition for E_θ will be

$$\frac{\beta}{\omega \epsilon_0} [D] \left(\frac{\Phi_e^I}{\epsilon_{r,I}} - \frac{\Phi_e^{II}}{\epsilon_{r,II}} \right) = [U] hr \left(\frac{d\Phi_h^{II}}{dr} - \frac{d\Phi_h^I}{dr} \right),$$

where, in analogy to the derivation of $[Q_x]$ in eq. (4.26) and eq. (4.27), $[U]$ is given as follows

$$[U] = \frac{1}{24} \begin{bmatrix} 22 & 1 & 0 & \dots & 0 & 0 & 1 \\ 1 & 22 & 1 & \dots & 0 & 0 & 0 \\ \dots & \dots & \dots & \dots & \dots & \dots & \dots \\ \dots & \dots & \dots & \dots & \dots & \dots & \dots \\ 0 & 0 & 0 & \dots & 1 & 22 & 1 \\ 1 & 0 & 0 & \dots & 0 & 1 & 22 \end{bmatrix}. \quad (5.29)$$

In a similar way the other field continuity conditions are discretized. It should be mentioned that the matrix $[U]$ can also be separated as $24[U] = [P_0] + 22[I]$. Hence, also matrices $[U]$ and $[D]$ can be diagonalized by the matrix $[T]$. The edge condition in the cylindrical MoL is found to be the same as that in Cartesian coordinates, approximately $\nu=0.3$.

5.6 SVD technique

The problem of solving eigenvalue equations is usually approached by directly evaluating the determinant of the matrix. However, due to the presence of poles, it is difficult to detect the zeros which can be near poles. This problem has been discussed in [68]. It was suggested to use the singular value decomposition technique (SVD) to eliminate poles. Although the SVD has existed in matrix algebra for decades little use has been made of this technique except in [68]. In the SVD the matrix $[Z] = [T][J_{mk}]$ in the eq.

(5.22) can be always diagonalized by two unitary matrices, $[U]$ and $[V]$ ($[U]^h[U]=[I]$ and $[V]^h[V]=[I]$) as $[U]^h[Z][V]=[S]$, where $[S]$ is a diagonal matrix whose elements are called singular values of the matrix $[Z]$ (c.f. [91]). Eq. (5.22) can be abbreviated as $[Z]\bar{a}=\bar{b}$. Then eq. (5.22) can be written as $[S]\bar{A}=\bar{B}$, where $\bar{A}=[V]^h\bar{a}$ and $\bar{B}=[U]^h\bar{b}$. Therefore, the lowest singular value approaching zero will be now exactly equivalent to eq. (5.22). The modal field and current distributions in eq. (5.22) can then be obtained from the last column of $[V]$ at the minima of the lowest $S_{\min} \rightarrow 0$.

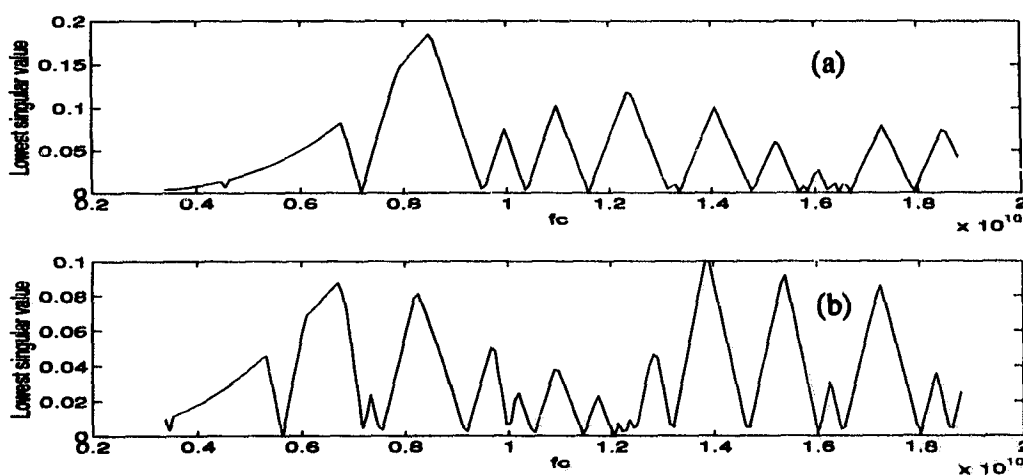


Figure 5.3 Evaluation of the lowest singular values of the eigenvalue matrix versus the cutoff frequencies of a cylindrical waveguide, $a=2.54$ cm, (a) TM modes, (b) TE modes

The determinant calculation will be equivalent to finding all the local minimum points of the lowest singular values of $[Z]$ along the frequency axis (Fig. 5.3) by using a one-dimensional line search method.

5.7 Numerical test

In order to test the MoL algorithm derived in this chapter, intensive simulations are performed for homogeneous and inhomogeneous waveguides by solving eq. (5.20) and eq. (5.22) respectively. In the following, some typical examples will be shown, and results will be compared with the literature.

5.7.1 Cylindrical microstrip lines

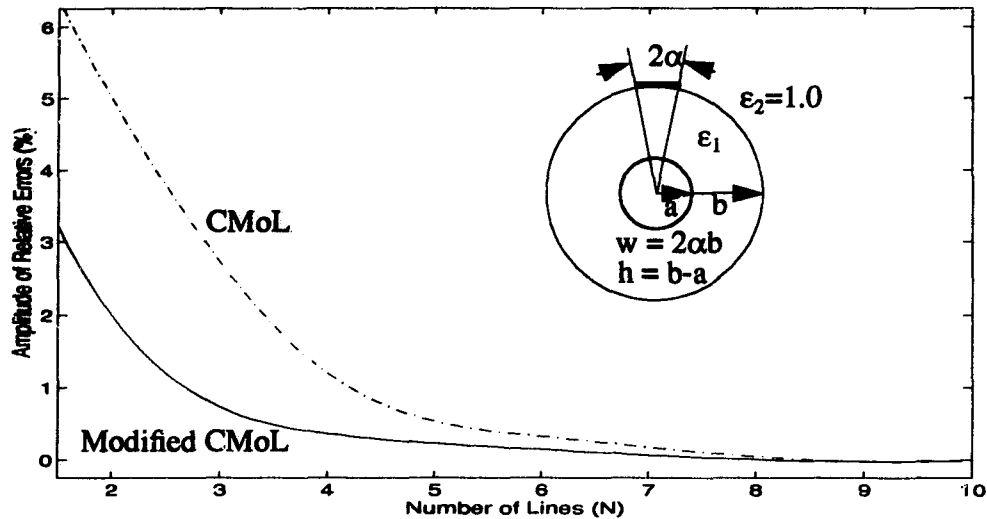


Figure 5.4 Convergence test for frequency-dependent properties of the open cylindrical microstrip lines, substrate relative dielectric constant $\epsilon_1 = 9.6$ (alumina), curvilinear coefficient $R = a/b = 0.9$

Inhomogeneous waveguides with complex cross section such as cylindrical strip-lines and microstrip transmission lines are important for planar circuits on curved substrate like antennas and their feedlines in mobile communications. A number of investigations on these inhomogeneous transmission lines have been reported in the literature (i.e. [74-79]). However, in most of these publications, only Laplace's equation has been solved instead of Helmholtz equation. Among the techniques used the conformal mapping technique is most prominent. The only full wave technique reported in the literature is [78,79]. The static and also frequency-dependent Green's function method results in [78,79] clearly showed that the full-wave analysis is necessary to account for the strong dispersion.

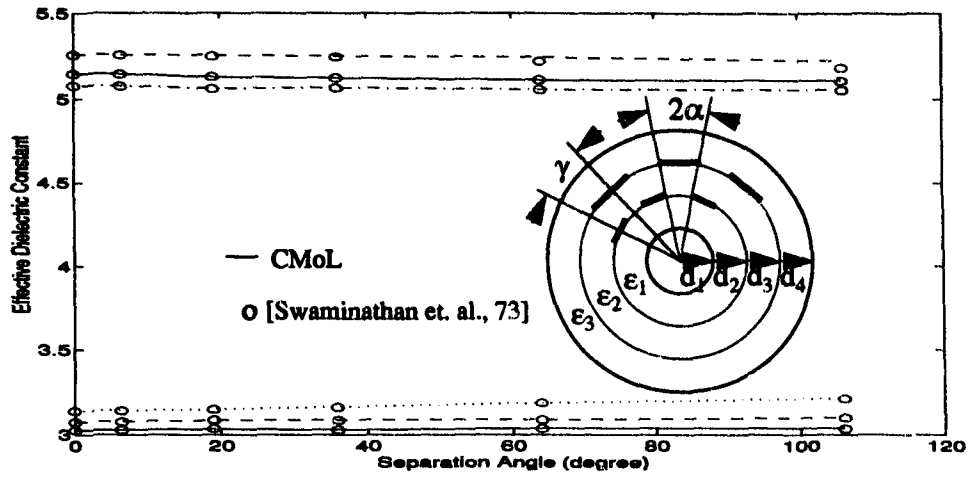


Figure 5.5 Effective dielectric constant of coupled striplines versus separation angle γ . $d_4/d_1=4$, $d_3/d_1=3$, $d_2/d_1=2$, $\epsilon_1=2$, $\epsilon_2=4$, $\epsilon_3=6$, $\alpha=10.195^\circ$

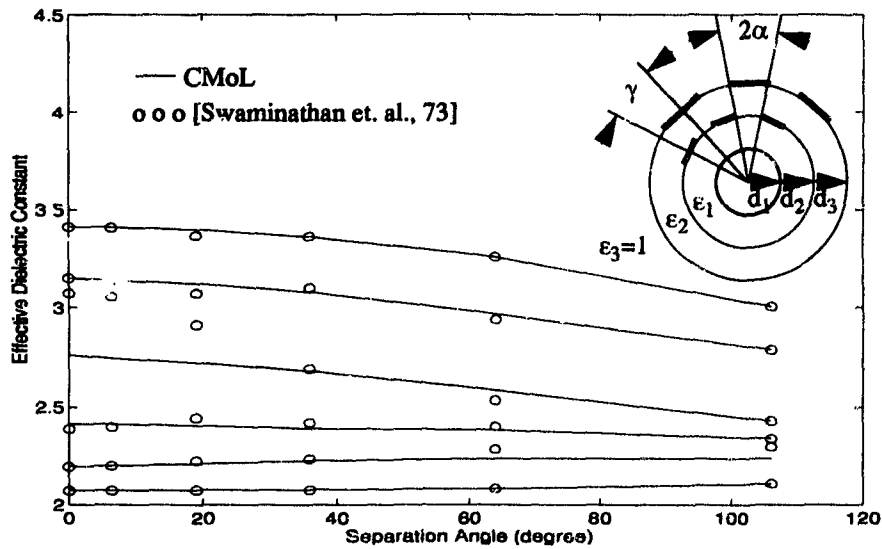


Figure 5.6 Effective dielectric constant of the open multiconductor microstrip lines versus the separation angle γ , the dimension for multilayers: $d_3/d_1 = 3$, $d_2/d_1 = 2$, $\epsilon_1 = 2$, $\epsilon_2 = 4$, $\epsilon_3 = 1$, $\alpha = 10.195^\circ$

First of all, Fig. 5.4 illustrates the advantages of using the scheme with fourth order accuracy over the one with only second order accuracy. To reach the same accuracy of the fourth order scheme, the second order scheme requires approximately twice the number of lines.

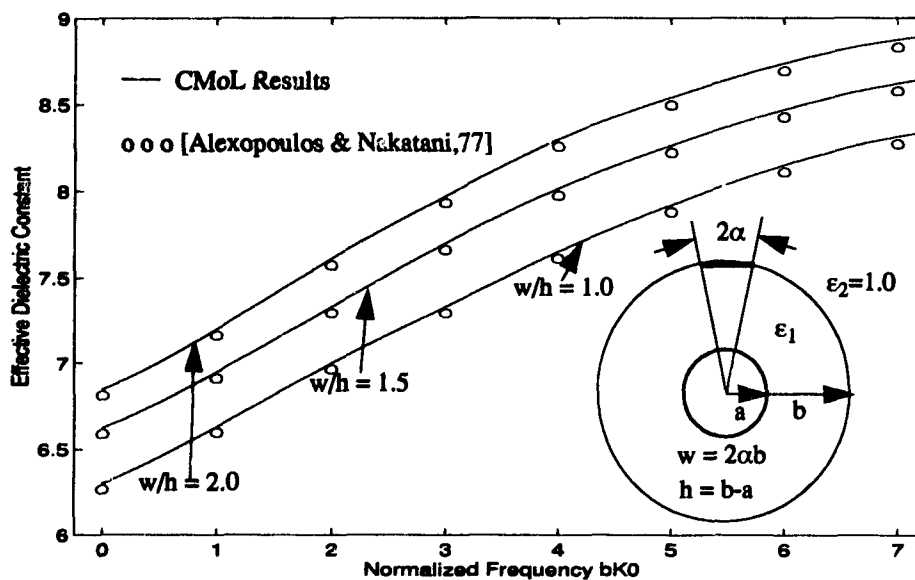


Figure 5.7 Frequency-dependent effective relative dielectric constant of the open cylindrical microstrip lines, substrate relative dielectric constant $\epsilon_1 = 9.6$ (alumina), Curvilinear coefficient $R = a/b = 0.9$

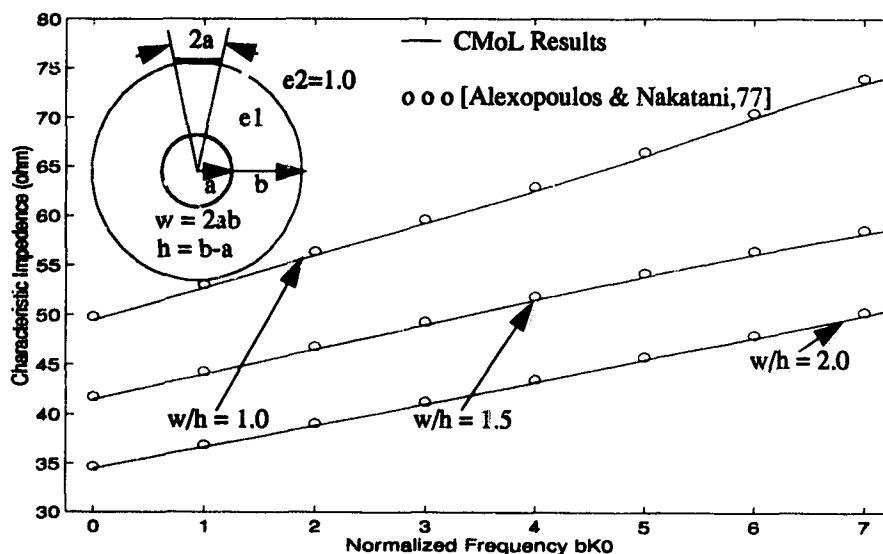


Figure 5.8 Frequency-dependent characteristic impedance of the open cylindrical microstrip lines, substrate relative dielectric constant $\epsilon_1 = 9.6$ (alumina). Curvilinear coefficient $R = a/b = 0.9$

Cylindrical striplines are then analyzed and the effective dielectric constant versus the separation angle for the six quasi-TEM modes are shown in Fig. 5.5 and Fig. 5.6 and compared to quasi-static results from the literature [73]. Both figures show the effective

dielectric permittivity for the buried coupled stripline and the coupled microstrip line, each with six stripes. Although the cylindrical MoL confirms most of the quasi-TEM modes obtained from the conformal mapping analysis [73], there is considerable disagreement with one mode in the microstrip structure (Fig. 5.5).

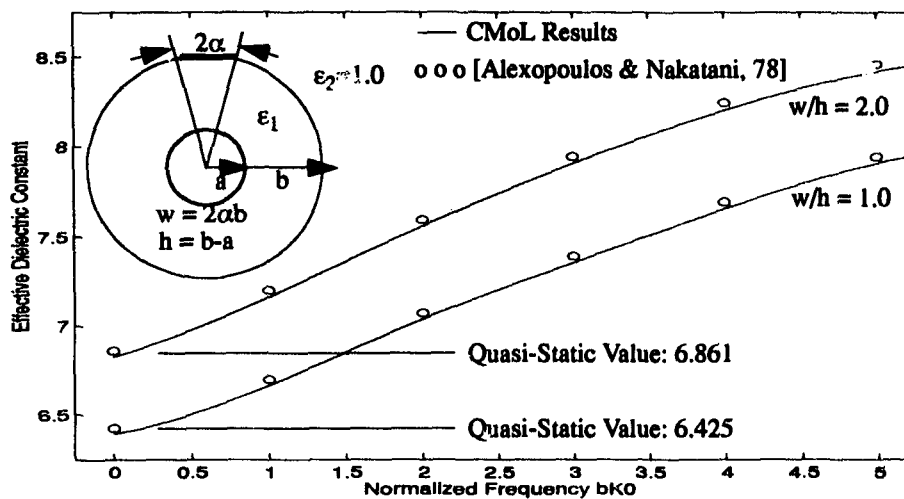


Figure 5.9 Frequency-dependent properties of the open cylindrical microstrip line, substrate relative permittivity $\epsilon_1 = 9.6$ (alumina), Curvilinear coefficient $R = a/b = 0.9$

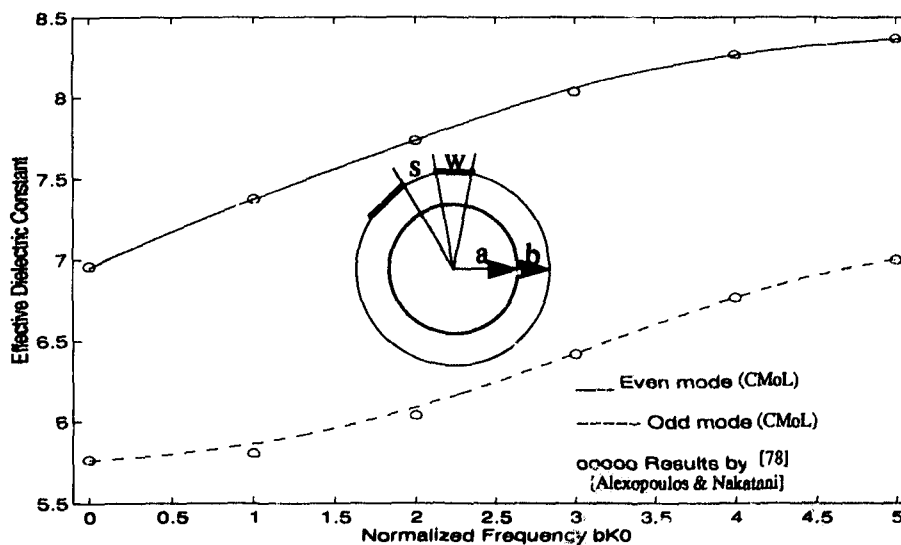


Figure 5.10 MoL results of coupled microstrip lines, $\epsilon_r = 9.6$, $w/h = 1.0$, $s/h = 1.0$, $a/b = 0.9$

Additional results shown in Fig. 5.6-5.9 confirm the accuracy of the CMoL. As

expected, the wider the strip, the lower the characteristic impedance and the higher the effective permittivity. Similar structures have been investigated in [78,79] on the basis of an integral equation approach. However, the problem with this technique is that the development of an accurate procedure for the computation of the Green's function on the substrate surface for both the source and the observation point [78,79] requires considerable computational effort to obtain accurate results. Moreover, the approach taken in [78,79] is not as flexible as the MoL technique described in this paper, because for more complex structural geometries additional preprocessing is needed, while this is not the case for the MoL. In the cylindrical MoL only the discretization size and/or the length of the radial lines need to be changed to analyze, for example, elliptical structures.

5.7.2 Homogeneous waveguide structures

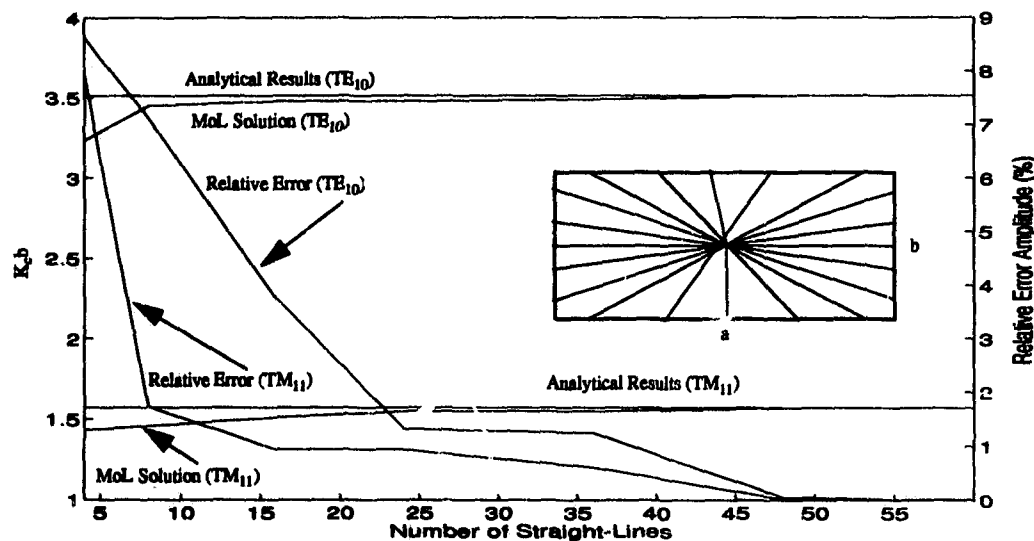


Figure 5.11 MoL results for TE₁₀ and TM₁₁ modes compared to analytical solutions for a rectangular waveguide, $b = a/2 = 3.555$ mm (WR-28)

Convergence tests for TE and TM modes in rectangular and circular waveguides are shown in Fig. 5.11 and Fig. 5.12. It is interesting to note that convergence for the TM₀₁ mode in Fig. 5.12 is possible with one line only, while the TE₁₁ mode requires at least 15-20 lines. This can be explained by the fact that the field distribution of the TM₀₁ mode is

constant in angular direction and changes only in radial direction, which can be described by one line. The field of the TE₁₁ mode, however, changes in radial and angular direction and thus requires more lines to be characterized accurately.

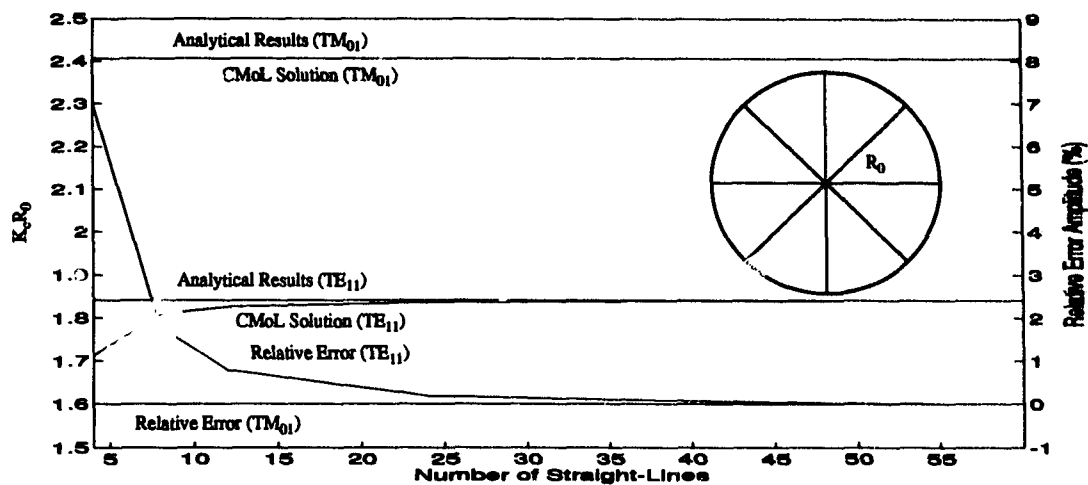


Figure 5.12 CMoL results for TE₁₁ and TM₀₁ modes compared to analytical solutions for a circular waveguide, R₀ = 2.54 cm

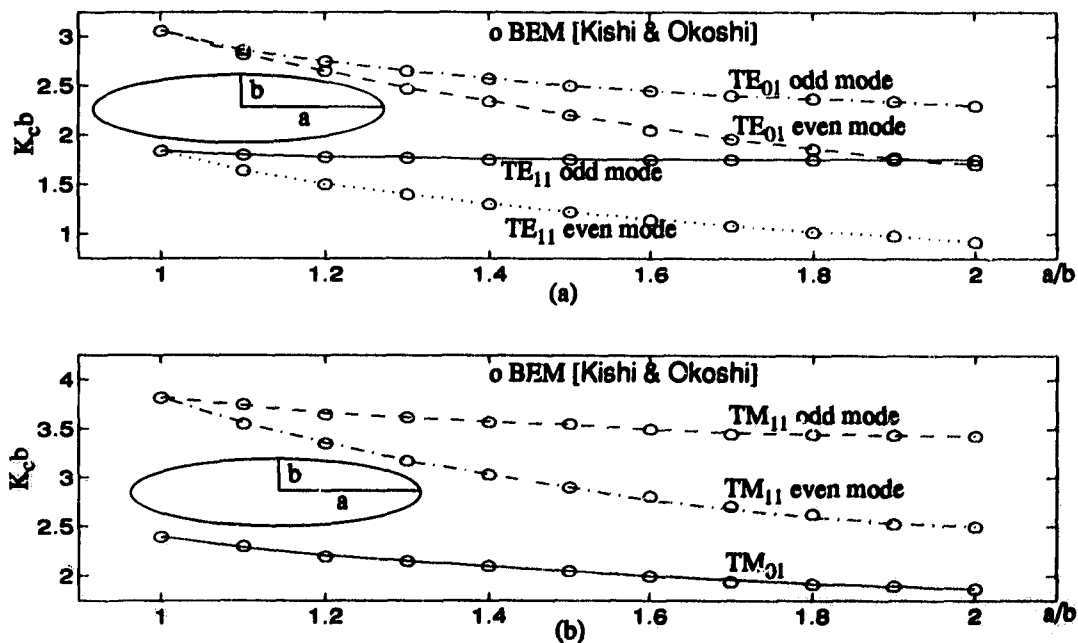


Figure 5.13 Normalized cutoff wavenumbers of elliptic waveguides for different axis ratio a/b calculated by CMoL and compared to the BEM [72], (a) TE modes, (b) TM modes

A comparison between the CMoL and BEM in elliptical waveguides shows very good agreement. This is demonstrated in Fig. 5.13 which illustrates the behavior of different higher order modes in elliptical waveguides versus the axis ratio.

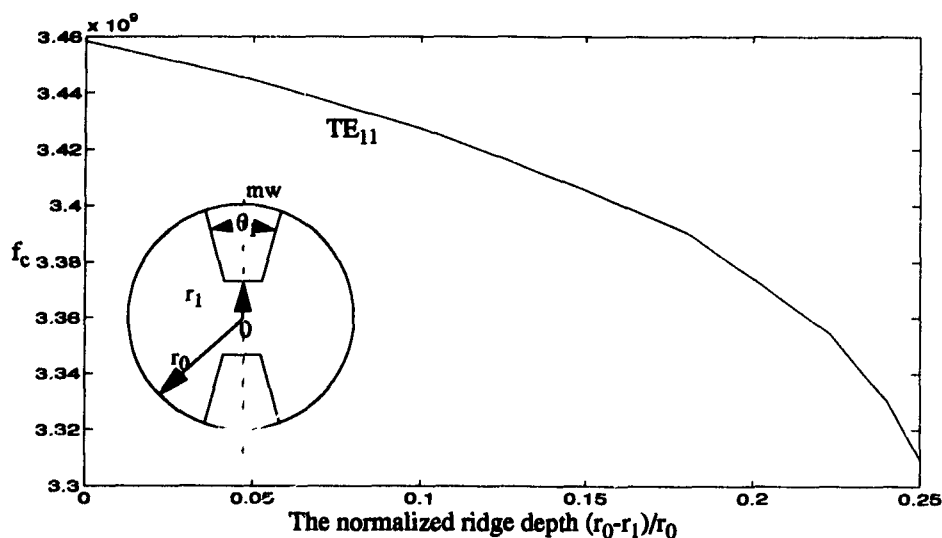


Figure 5.14 Effect of the ridges on the cutoff frequencies of the fundamental TE_{11} mode, $r_0 = 2.54$ cm

A double-ridge circular waveguide is shown in Fig. 5.14. A magnetic wall is assumed in vertical direction (polarization plane for the TE_{11} mode). In this case the cutoff frequency of the fundamental TE_{11} mode reduces with decreasing r_1 . This effect is similar to the one in a ridge loaded rectangular waveguide and needs no further explanation.

Fig. 5.15 illustrates the effect of a fifth ridge, which is the coupling element in a dual mode circular ridged waveguide (CRW) resonator. Here the influence on the first two TE modes is small while the TM mode increases its cutoff frequency even more when the ridge penetrates further into the CRW. The separation between the TM modes and the fundamental TE mode becomes larger.

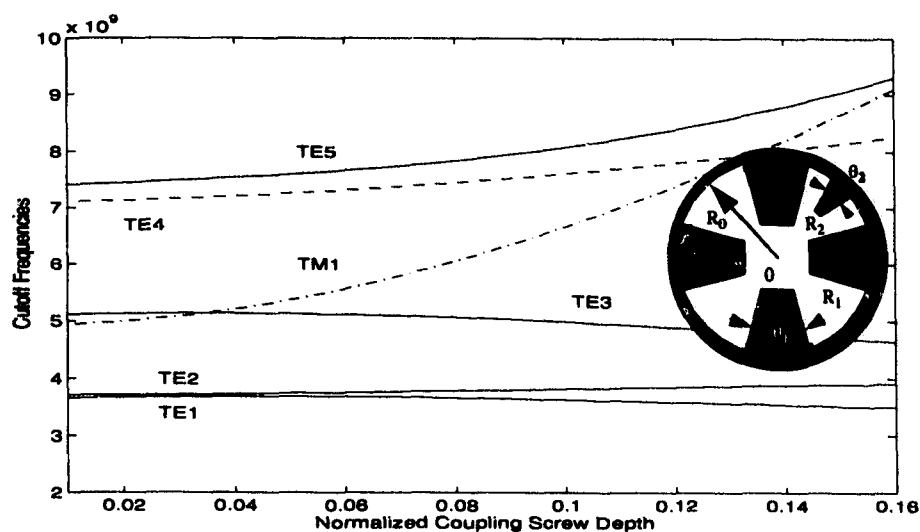


Figure 5.15 Cutoff frequencies of CRW with fifth ridge, $R_0 = 2.54$ cm, $\theta_1 = 25^\circ$, $\theta_2 = 12.5^\circ$

5.8 Conclusion and discussion

The method of lines is extended for use in cylindrical coordinates. Microstrip and stripline structures on curved multilayered substrates have been characterized. Also TE and TM mode cutoff frequencies in circular and elliptical waveguides with and without ridge loading have been calculated. In comparison with other numerical techniques good agreement was found.

Chapter 6

Characterization of resonators and cavities using the 3D CMoL

The 2D-CMoL described in the previous chapter is now extended to spatial 3D discontinuities. The advantage of the 3D CMoL is that only two out of three space variables need to be discretized, while for the third direction the Helmholtz equation can be solved analytically. The 3D CMoL is especially suitable for the analysis and design of cylindrical/rectangular cavities filled partly or totally with dielectric blocks of arbitrary shape. Results are presented for a variety of resonator structures. Of particular interest is the resonance frequency calculation of a dielectric rod of varying diameter within a rectangular cavity.

6.1 Introduction

Microwave cavities are important components in communication systems. Microwave filters and multiplexers consist of a cascade of cavities which together with coupling structures are the fundamental building blocks of these components. Characterization and design of these cavities are not a trivial task because of the high-Q resonant structures and mixed coordinates involved [80-82].

In the following the cylindrical 3D method of Lines (MoL) is utilized to discretize the angular and longitudinal space directions. The resulting Helmholtz equation is a set of coupled one dimensional differential equations. Applying the decoupling procedure described in the previous chapters, each ordinary differential equation can then be solved analytically at each line in radial direction after an orthogonal transformation. This is the first time in the literature that the CMoL is applied also to 3D problems. Some microwave

cavities are simulated to demonstrate the usefulness of the approach.

6.2 Semianalytical solution of Helmholtz equation

The microwave structures can be subdivided into several uniform regions in which a constant dielectric is assumed. Unlike in an eigenvalue problem, where the discretization of the Helmholtz equation is only related to the θ -variable, the spatial 3D discontinuity of Fig. 6.1 requires also the discretization of the z -variable. Hence the Helmholtz equation is now written in the following form

$$\frac{1}{r} \frac{\partial}{\partial r} \left(r \frac{\partial \phi}{\partial r} \right) + \frac{\partial^2 \phi}{r^2 \partial \theta^2} + \frac{\partial^2 \phi}{\partial z^2} + k_0^2 \phi = 0 \quad (6.1)$$

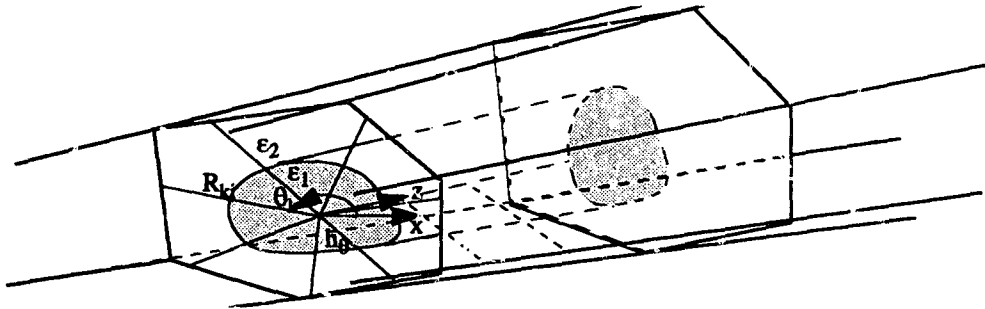


Figure 6.1 3D MoL discretization in a cylindrical coordinate system

Since the hybrid field problem can not be solved analytically for the whole region, the calculation domain is now discretized in θ - and z -directions by a number of straight lines along the r -direction. In Fig. 6.1, the θ -variables are discretized uniformly by using radial lines at $\theta_{ki} = \theta_{1i} + (k-1)h_\theta$, $k=1,2,\dots,N_\theta$, with h_θ being the angular spacing between the lines. The z -variable is discretized uniformly by using radial lines at

$$z_{ki} = z_{k1} + (i-1)h_z, \quad i=1,2,\dots,N_z \quad (6.2)$$

with h_z being the spacing between the lines in z -direction. The first order finite difference operators are approximated by the central finite differences as

$$\left. \frac{\partial \phi_{e,h}}{\partial \theta} \right|_{k+0.5} = \frac{\phi_{e,h}|_{k+1} - \phi_{e,h}|_k}{h_\theta}, \quad \left. \frac{\partial \phi_{e,h}}{\partial z} \right|_{i+0.5} = \frac{\phi_{e,h}|_{i+1} - \phi_{e,h}|_i}{h_z} \quad (6.3)$$

where the vectors $\phi_{e,h}$ are in matrix form as $\bar{\phi} = [\phi] = [\phi_{11} \ \phi_{21} \ \dots \ \phi_{k1} \ \dots \ \phi_{N_\theta 1}; \ \phi_{12} \ \phi_{22} \ \dots$

$\phi_{kz}, \dots, \phi_{N\theta}, \dots, \phi_{1i}, \phi_{2i}, \dots, \phi_{ki}, \dots, \phi_{N\theta}, \dots, \phi_{1Nz}, \phi_{2Nz}, \phi_{3Nz}, \dots, \phi_{N\theta}, \dots$, or its derivatives

$$h_\theta \frac{\partial \bar{\Phi}_{e,h}}{\partial \theta} \cong [D]_\theta \bar{\Phi}_{e,h}, \quad h_z \frac{\partial \bar{\Phi}_{e,h}}{\partial z} \cong [D]_z \bar{\Phi}_{e,h} \quad (6.4)$$

Generally, the first order difference operators $[D]_{e,h}^z$ are bi-diagonal matrices.

Using the central finite difference scheme again to calculate the second order partial differential operator from the first order ones yields

$$h^2 \frac{\partial^2 \bar{\Phi}_e}{\partial \theta^2} \Big|_k = \left(-[D]_\theta^t \right) [D]_\theta \bar{\Phi}_e = [P]_\theta \bar{\Phi}_e, \quad h^2 \frac{\partial^2 \bar{\Phi}_h}{\partial \theta^2} \Big|_k = [D]_\theta \left(-[D]_\theta^t \right) \bar{\Phi}_h = [P]_\theta \bar{\Phi}_h \quad (6.5)$$

$$h_z^2 \frac{\partial^2 \bar{\Phi}_e}{\partial z^2} \Big|_i = \bar{\Phi}_e \left(-[D]_z^t \right) [D]_z = \bar{\Phi}_e [Q]_e^t, \quad h_z^2 \frac{\partial^2 \bar{\Phi}_h}{\partial z^2} \Big|_i = \bar{\Phi}_h [D]_z^t \left(-[D]_z \right) = \bar{\Phi}_h [Q]_h^t$$

where $[P] = [D](-[D]^t) = (-[D]^t)[D]$, and $[P]$ can be found in last chapter. The finite difference operators depend on the boundary conditions. $[P]$ can be factorized by an orthogonal matrix $[T_\theta]$ as $[P] = [T_\theta][\lambda][T_\theta]^t$, where $[T_\theta]^t = [T_\theta]^{-1} = [T_\theta]$. Similarly there is an orthogonal transformation matrix $[T_z]$ to diagonalize the matrix $[Q]^t$ as $[T_z]^t [Q]^t [T_z] = \text{diag}\{\delta_k\}$. The eigenvalues of $[T_z]$ are denoted by $\text{diag}\{\beta_k\}$. Therefore, the discretized Helmholtz equation will be as follows:

$$\frac{d}{dr} \left(r \frac{d\bar{\Phi}}{dr} \right) + k_0^2 \bar{\Phi} - \frac{[P] \bar{\Phi}}{r^2 h_\theta^2} - \frac{\bar{\Phi} [Q]^t}{h_z^2} = 0 \quad (6.6)$$

We define the transformed quantities as

$$[\varphi] = [T_z^{e,h}]^t \bar{\Phi} [T_\theta^{e,h}] \quad (6.7)$$

Multiplying $[T_z]^t$ and $[T_\theta]$, respectively, from the left and right sides of eq. (6.6) to diagonalize $[P]$ and $[Q]$, the set of Helmholtz equations in eq. (6.6) can be decoupled into a set of independent ordinary differential equations of Bessel form

$$\frac{d}{dr} \left(r \frac{d\varphi_{ki}}{dr} \right) + \left(\chi_{ik}^2 - \frac{\mu_k^2}{r^2} \right) \varphi_{ki} = 0, \quad \chi_{ik}^2 = \left(k_0^2 + \frac{\delta_{ii}}{h^2} \right), \quad \mu_k = \frac{2 \sin(\alpha_k/2)}{h} \quad (6.8)$$

where φ_{ki} ($k=1,2,3,\dots,N_0$; $i=1,2,3,\dots,N_2$) is called the transformed potential function, eigenvalues δ_{ii} are the diagonal elements of a diagonal matrix. In every uniform region, a solution of eq. (6.8) may be written as a superposition of Bessel functions of μ_k -order

$$\varphi_{ki} = A_k J_{\mu_k}(\chi_{ik}r) + B_k N_{\mu_k}(\chi_{ik}r), \quad (6.9)$$

$$\varphi_{ki} = A_k J_{\mu_k}(\chi_{ik}r) + B_k H_{\mu_k}^{(2)}(\chi_{ik}r), \quad (6.10)$$

$$\varphi_{ki} = A_k H_{\mu_k}^{(1)}(\chi_{ik}r) + B_k H_{\mu_k}^{(2)}(\chi_{ik}r). \quad (6.11)$$

The selection of above equations depends on individual applications. For example, to analyze guided wave structures, the combination of the first kind and the second kind of Bessel functions in eq. (6.9) are usually used because they appropriately describe the characteristic of the standing waves in the waveguides. However, eq. (6.11) is useful for antenna applications. It should be noticed that when the region of the solution contains the origin $r=0$, B_k must be zero since N_{μ_k} and H_{μ_k} are singular. After eq. (6.8) is solved in every uniform region (non-uniform region can also be solved by using a Sturm-Liouville equation), the potentials $\bar{\phi}$ can be obtained by an inverse transformation in eq. (6.7) for $\bar{\phi}_e$ and $\bar{\phi}_h$, respectively.

6.2.1 Inhomogeneous structures

After the Helmholtz equations are solved in each uniform region, the fields at the interfaces between the uniform regions are matched in order to solve the whole structure. The tangential fields at interfaces between neighboring regions are expressed in terms of ϕ_e and ϕ_h . For instance

$$\frac{1}{\omega\mu} [D]_{\theta}^t \left(\frac{\bar{\phi}_h^{II}}{\epsilon_{r,II}} - \frac{\bar{\phi}_h^I}{\epsilon_{r,I}} \right) [D]_z^t - J_z = rh \left(\frac{d\bar{\phi}_e^I}{dr} - \frac{d\bar{\phi}_e^{II}}{dr} \right). \quad (6.12)$$

Applying the transformation matrices $[T_{\theta}]$ and $[T_z]$ from the left and the right of eq. (6.12) the field continuity equations are diagonalized to give a set of uncoupled equations. Therefore, transforming those potentials back to the original domain yields

$$[Z] \begin{bmatrix} E_z \\ E_\theta \end{bmatrix} = \begin{bmatrix} J_z \\ J_\theta \end{bmatrix}. \quad (6.13)$$

By using of the condition of zero current distribution along the dielectric interfaces, we will have the determinantal eigenvalue equation $[Z] \begin{bmatrix} E_z \\ E_\theta \end{bmatrix}' = 0$. The nontrivial solution requires that the determinant of the reduced matrix $[Z]$ is zero:

$$\det \{ [Z] \} = 0. \quad (6.14)$$

All the resonant frequencies can be obtained by solving the above equation. Subsequently all the field components and current density distributions can be obtained.

6.2.2 Homogeneous cavities

For homogeneous structures, the eigenvalue problem can be greatly simplified. All the elements in eq. (6.14) may be given in simplified forms. Using eq. (6.12) and (6.13), we can obtain the potential functions ϕ_e and ϕ_h (proportional to the tangential fields E_z and H_z) on the shielding surface contour as

$$[G]\bar{A} = \bar{\phi} \quad (6.15)$$

where the field coefficient vector is defined as

$$\bar{A} = [A_{11} \ A_{21} \dots \ A_{N\theta 1}, \ A_{12} \ A_{22} \dots \ A_{N\theta 2}, \dots, \ A_{1 N_z} \ A_{2 N_z} \dots \ A_{N\theta N_z}] \quad (6.16)$$

Applying the boundary conditions $\sigma \bar{\phi} = 0$ (ϕ_e for TM modes and ϕ_h for TE modes) on the shielding contour an eigenvalue problem is obtained as $\det\{[G]\} = 0$. For example, for TM modes, the boundary conditions $\bar{\phi}_e = 0$ ($E_z = 0$) on the shielding contour requires that

$$\det \left\{ \begin{bmatrix} [G_{11}] & [G_{12}] & \dots & [G_{1k_\theta}] & \dots & [G_{1N_\theta}] \\ \dots & \dots & \dots & \dots & \dots & \dots \\ [G_{i_\theta 1}] & [G_{i_\theta 2}] & \dots & [G_{i_\theta k_\theta}] & \dots & [G_{i_\theta N_\theta}] \\ \dots & \dots & \dots & \dots & \dots & \dots \\ [G_{N_\theta 1}] & [G_{N_\theta 2}] & \dots & [G_{N_\theta k_\theta}] & \dots & [G_{N_\theta N_\theta}] \end{bmatrix} \right\} = 0 \quad (6.17)$$

where

$$[G_{i_0 k_0}]_{N_z \times N_z} =$$

$$\begin{bmatrix} T_{11}^z T_{i_0 k_0}^\theta J_{\mu_{k_0}}(\chi_{ik} r_{k_0 1}) & \dots & T_{j_z 1}^z T_{i_0 k_0}^\theta J_{\mu_{k_0}}(\chi_{ik} r_{k_0 i_z}) & \dots & T_{N_z 1}^z T_{i_0 k_0}^\theta J_{\mu_{k_0}}(\chi_{ik} r_{k_0 N_z}) \\ \dots & \dots & \dots & \dots & \dots \\ T_{1 i_z}^z T_{i_0 k_0}^\theta J_{\mu_{k_0}}(\chi_{ik} r_{k_0 1}) & \dots & T_{j_z i_z}^z T_{i_0 k_0}^\theta J_{\mu_{k_0}}(\chi_{ik} r_{k_0 i_z}) & \dots & T_{N_z i_z}^z T_{i_0 k_0}^\theta J_{\mu_{k_0}}(\chi_{ik} r_{k_0 N_z}) \\ \dots & \dots & \dots & \dots & \dots \\ T_{1 N_z}^z T_{i_0 k_0}^\theta J_{\mu_{k_0}}(\chi_{ik} r_{k_0 1}) & \dots & T_{j_z N_z}^z T_{i_0 k_0}^\theta J_{\mu_{k_0}}(\chi_{ik} r_{k_0 i_z}) & \dots & T_{N_z N_z}^z T_{i_0 k_0}^\theta J_{\mu_{k_0}}(\chi_{ik} r_{k_0 N_z}) \end{bmatrix}$$

(6.18)

χ_{ik} is given in eq.(6.8). Similarly, we can obtain an eigenvalue equation for TE modes but with Bessel functions replaced by their derivatives to satisfy the TE mode boundary conditions $\bar{\phi}_h = 0$ ($H_z = 0$) along the conductor shielding contour \bar{R} (Appendix H).

6.3 Numerical results

The 3D CMoL has been tested for circular (Fig. 6.2) and rectangular (Fig. 6.3) cavities and compared to analytical solutions. It was found that the convergence of the method depends on the specific type of mode considered. For example, the analytical solution for the TM_{010} mode in Fig. 6.2 is already reached with only 20-25 lines, while the TE_{111} mode requires approximately 35 lines. For the rectangular resonator (Fig. 6.3) a larger number of lines is needed because of the approximation of the rectangular boundary by radial discretization lines. Loading the cylindrical cavity with a cylindrical dielectric block of varying radius reduces the resonant frequency of the first resonator mode, which is of course expected. The same effect is obtained when we insert a cylindrical dielectric block into a rectangular cavity (Fig. 6.5). The novelty of the analysis here is that the structure contains subregions which are described by a rectangular (rectangular cavity) and a cylindrical coordinate system (dielectric rod). To discretize this 3D structure (for all the higher order modes) requires approximately 50 lines in the a-b-plane and 12-lines in the longitudinal direction (L). Fig. 6.4 shows dielectric loaded cylindrical cav-

ities. Fig. 6.6 illustrates the fundamental mode resonant frequency for a non-uniform dielectric rod with varying height of the partially thicker diameter. It should be noted that the transition between the thin rod diameter (r_0) and the thick section is made smoothly rather than abruptly. This is done to demonstrate the flexibility of the 3D CMoL.

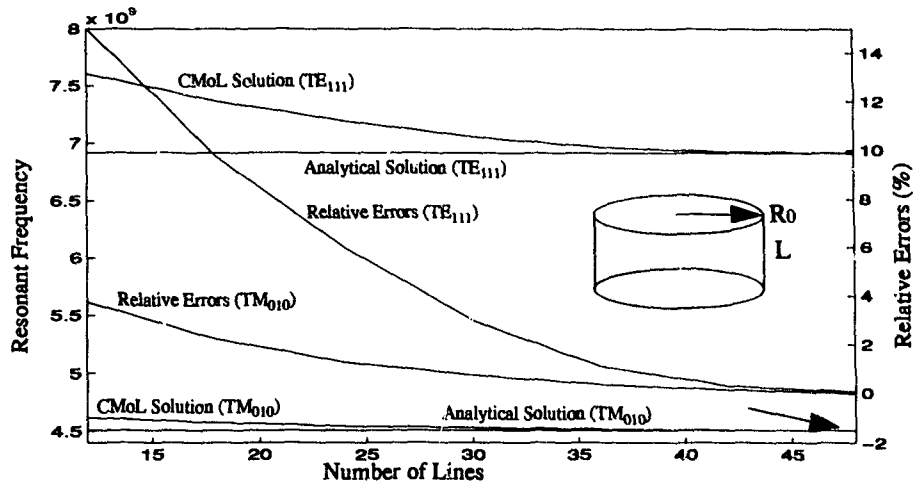


Figure 6.2 Resonant frequencies of TE₁₁₁ and TM₀₁₀ modes by 3D cylindrical MoL compared to the analytical solutions for a circular waveguide, $L = R_0 = 2.54$ cm

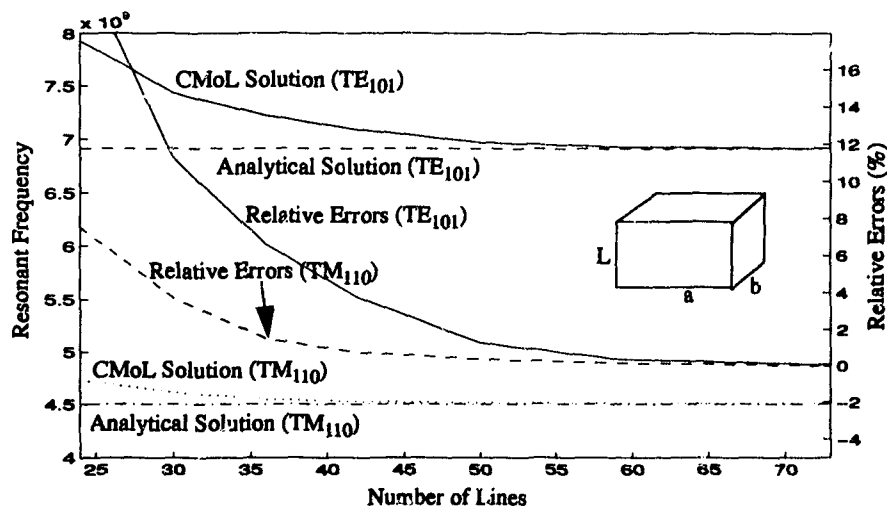


Figure 6.3 Resonant frequencies of TE₁₀₁ and TM₁₁₀ modes by 3D cylindrical MoL compared to the analytical solutions for a rectangular waveguide, $L = b = a/2 = 3.555$ mm

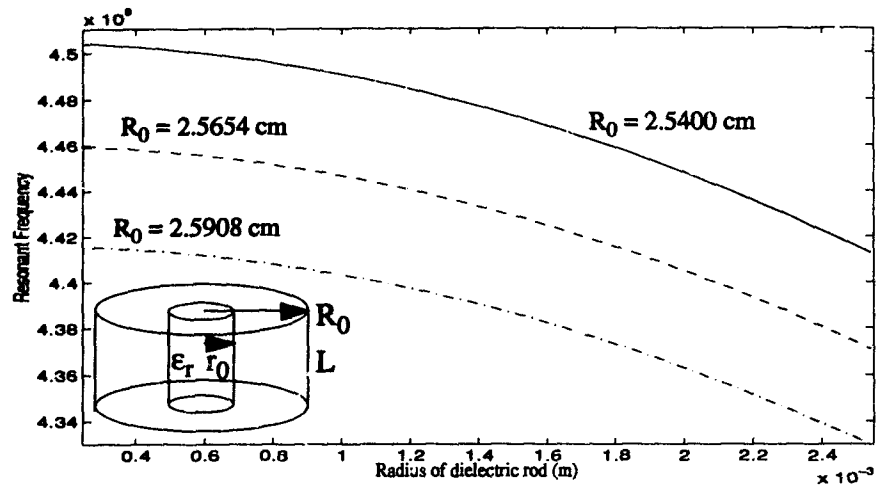


Figure 6.4 3D CMoL calculation of resonant frequencies of the TM_{010} mode in a dielectric-loaded ($\epsilon_r=2.2$) circular waveguide cavity; $L = R_0 = 2.54$ cm, 2.5654 cm, 2.5908 cm

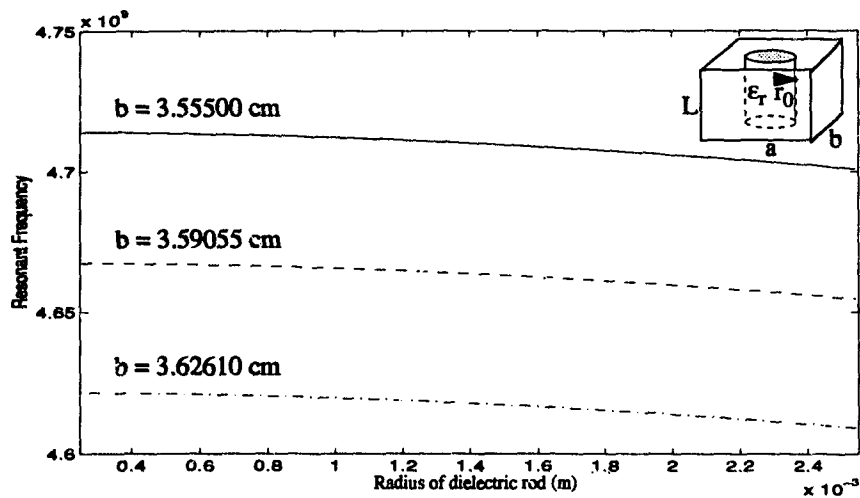


Figure 6.5 3D CMoL calculation of Resonant frequencies of TM_{110} mode in a dielectric-loaded ($\epsilon_r=2.2$) rectangular waveguide cavity; $L = b = a/2 = 3.555$ cm, 3.59055 cm, 3.62610 cm

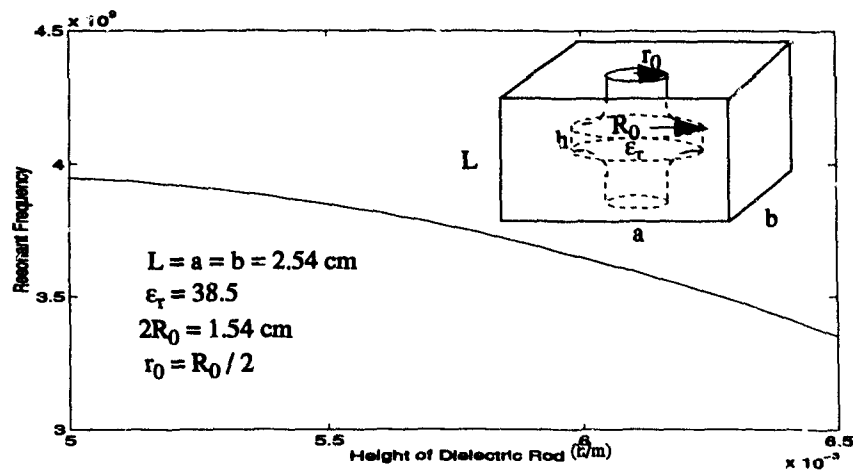


Figure 6.6 Resonant frequencies of a dielectric loaded waveguide cavity, $a = b = L = 2.54 \text{ cm}$, $R_0 = 1.54 \text{ cm}$, $r_0 = R_0 / 2$, $\epsilon_r = 38.5$

6.4 Conclusion

A 3D cylindrical method of lines has been presented for the analysis and the design of microwave resonators of arbitrary shape. Cylindrical and rectangular cavities are calculated with and without partial dielectric filling.

Chapter 7

Analysis of waveguide discontinuities by CMoL

In the previous chapter (6) a resonant model of the 3D CMoL was introduced. In this chapter, the 3D CMoL is extended to S-parameter analysis of discontinuities in guided wave structures.

7.1 S-Parameter extractions by cavity model

The CMoL is combined with the cavity model calculate the scattering parameters of guided wave structures. The CMoL resonant model is utilized to determine the resonant frequencies of the enclosed discontinuity or equivalently the resonant lengths of the transmission lines connecting the discontinuity for a given frequency. These resonant lengths or frequencies are then used to extract the equivalent network parameters (for instance, the reactances in Fig. 7.1 and the S-parameters in Fig. 7.2) representing the discontinuity.

7.1.1 Cavity Model

The determination of the equivalent circuit parameters of a two-port network via the evaluation of the resonant frequencies of the network inserted between reactive terminations is equivalent to the experimental technique known as the tangent method [71]. Similar ideas have been widely used in numerical modeling of microwave circuits such as in [1,64,65]. This cavity model is utilized in CMoL in this chapter to analyze waveguide discontinuities.

Considering first a discontinuity of a waveguide (planar waveguide such as a CPW or cylindrical waveguide such as a coaxial waveguide) short end in Fig. 7.1a which can be treated as an equivalent reactance shown in Fig. 7.1b. The voltage minimum points satisfy

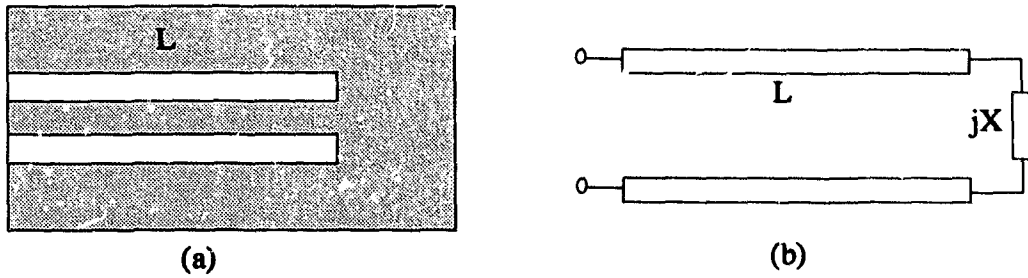


Figure 7.1 (a) Waveguide short end, and (b) equivalent circuit.

$$\tan(2\pi L/\lambda) + X = \tan(\theta) + X = 0 \tag{7.1}$$

The reflection coefficient of the CPW short end is given as

$$\Gamma = -\exp(2j\theta) \tag{7.2}$$

Consequently, the location of voltage minimum points determines the equivalent reactance X. The above equations are nothing else but the resonant condition of the transmission line of length L loaded with a reactance X. The resonant frequency for a fixed length L or the resonant length L for a given frequency will determine the equivalent circuit X, or equivalently the S-parameters.

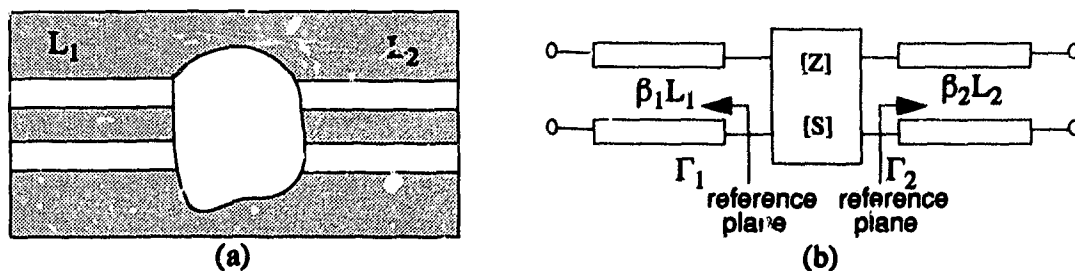


Figure 7.2 (a) A 2-port CPW discontinuity, and (b) equivalent circuit.

Considering now a two-port discontinuity of Fig. 7.2, where the two transmission

line ends are terminated by two electric- (or magnetic-) wall planes to form a cavity.

Looking into the discontinuity from the reference planes, the voltages and currents are connected by equivalent circuit parameters

$$\begin{bmatrix} V_1 \\ V_2 \end{bmatrix} = \begin{bmatrix} Z_{11} & Z_{12} \\ Z_{21} & Z_{22} \end{bmatrix} \begin{bmatrix} I_1 \\ I_2 \end{bmatrix}. \quad (7.3)$$

On the other hand, looking towards the electric-wall planes from the reference planes, it is well known that

$$\begin{bmatrix} V_1 \\ V_2 \end{bmatrix} = \begin{bmatrix} jZ_1 \operatorname{tg}(\beta_1 L_1) & 0 \\ 0 & jZ_2 \operatorname{tg}(\beta_2 L_2) \end{bmatrix} \begin{bmatrix} -I_1 \\ -I_2 \end{bmatrix}, \quad (7.4)$$

where β_i and Z_i ($i=1,2$) are the propagation constants and characteristic impedances of the waveguide sections on the left and right sides of the discontinuity, respectively. From the above equations, we obtain a system of homogeneous equations as

$$\begin{bmatrix} Z_{11} + jZ_1 \operatorname{tg}(\beta_1 L_1) & Z_{12} \\ Z_{21} & Z_{22} + jZ_2 \operatorname{tg}(\beta_2 L_2) \end{bmatrix} \begin{bmatrix} I_1 \\ I_2 \end{bmatrix} = \begin{bmatrix} 0 \\ 0 \end{bmatrix}, \quad (7.5)$$

from which the non-trivial solutions for the currents results in the resonant equation

$$F(L_1, L_2, f) = \{Z_{11} + jZ_1 \operatorname{tg}(\beta_1 L_1)\} \times \{Z_{22} + jZ_2 \operatorname{tg}(\beta_2 L_2)\} - Z_{12} \times Z_{21} = 0 \quad (7.6)$$

where $Z_{12}=Z_{21}$ for reciprocal circuits. By fixing the frequency f , three sets of resonant lengths of the cavities are calculated from MoL, and subsequently Z_{11} , Z_{12} , and Z_{22} are determined.

7.1.2 Procedure of S-parameter calculation

To extract the S-parameters from the above knowledge, we proceed as follows:

- (1) We first assume a discontinuity enclosed into a cavity.
- (2) The resonant frequencies or equivalently the resonant lengths of the cavity are

calculated by following the CMoL techniques covered in previous chapters.

(3) Then the S-parameters of the discontinuity can be extracted from the resonant frequencies or equivalently the resonant lengths as follows [1]

$$s_{11} = -\frac{(a_1\Gamma_{1a} + b_1\Gamma_{1b} + c_1\Gamma_{1c})}{\Delta}; \quad s_{22} = -\frac{(a_2\Gamma_{2a} + b_2\Gamma_{2b} + c_2\Gamma_{2c})}{\Delta}; \quad (7.7)$$

$$a_1 = \Gamma_{2a}(\Gamma_{1b} - \Gamma_{1c}); \quad b_1 = \Gamma_{2b}(\Gamma_{1c} - \Gamma_{1a}); \quad c_1 = \Gamma_{2c}(\Gamma_{1a} - \Gamma_{1b});$$

$$a_2 = \Gamma_{1a}(\Gamma_{2c} - \Gamma_{2b}); \quad b_2 = \Gamma_{1b}(\Gamma_{2a} - \Gamma_{2c}); \quad c_2 = \Gamma_{1c}(\Gamma_{2b} - \Gamma_{2a});$$

$$\Delta = a_1 + b_1 + c_1 = a_2 + b_2 + c_2;$$

$$s_{12} = (s_{11} + \Gamma_1)(s_{22} + \Gamma_2); \quad (7.8)$$

$$\Gamma_{1a} = \exp\{-2j\theta_{1a}\} = \exp\{-2j\beta_{1a}L_{1a}\}, \dots, \text{etc.}$$

where (L_{1a}, L_{2a}) , (L_{1b}, L_{2b}) , and (L_{1c}, L_{2c}) are three pairs of resonant lengths. Although the least square curve-fitting scheme may be used for more than three pairs of resonant lengths, exactly three pairs of resonant lengths are assumed in this thesis.

7.2 Hybrid-boundary model for CMoL

In the previous section, to analyze waveguide discontinuities the cavity model combined with CMoL needs at least three calculations of the cavity resonant frequencies. Moreover, to determine a resonant frequency the eigenvalue equation (6.14) or (6.17) must be evaluated in the CMoL at numerous frequency points. Therefore the numerical effort in the cavity model is very large. However, these efforts can be avoided when inhomogeneous boundary conditions are utilized in the CMoL. This is described in the following.

7.2.1 Introduction

As shown in the previous chapter and last section, the method of lines is well suited for analyzing three dimensional resonators and periodic structures. However, to avoid multiple calculations the boundary conditions must be treated differently. To avoid the cavity model, Worm [57] tackled the microstrip discontinuity by introducing inhomogeneous boundary conditions to the input port and assuming a short or an open circuit at the output port to obtain a homogeneous boundary condition. However, this method still needs three calculations. Wu, Yu, and Vahldieck considered the same discontinuity problem by using the hybrid boundary conditions [54]. In the first case the incident and excited waves were tackled individually and in the second case only the reflection coefficient was shown. Chung and Chrang [64] improved these techniques in the Cartesian MoL to model CPW discontinuities in one calculation.

The past work in the 3D MoL area is confined within Cartesian coordinates. In this section, inhomogeneous boundary conditions [64] are realized in cylindrical coordinates with the reflection and transmission coefficients as unknowns. The CMoL is developed to calculate three dimensional discontinuities. The calculation can be done in a single calculation instead of three. Therefore the calculation time is improved by an order of three.

7.2.2 Hybrid boundary conditions in CMoL

The formulation of the CMoL is similar to that in the last two chapters. The difference here is to assume inhomogeneous boundary conditions at reference planes instead of ideal electric or magnetic walls assumed for cavities and resonators. A regionally constant dielectric is assumed in each uniform region of the structures under study. The electromagnetic field components E_z and H_z which are proportional to the scalar potentials $\phi_{e,h} \exp\{j\omega t\}$ also satisfy the Helmholtz equation in a polar coordinate system given in (6.1) and the boundary conditions depending on the structure and modes we are interested in.

Since the hybrid field problem can not be solved analytically for the whole region,

the fields are discretized in θ - and z -directions by a number of straight lines along the r -direction as shown in Fig. 7.3. The waveguides are assumed to be single-moded and extend uniformly to infinity in the $+z$ and $-z$ directions, respectively. Let a mode (usually the fundamental one) propagate toward the discontinuity from the left side, some of the power is reflected back to form a standing wave on the left, and the remaining power is transmitted to the right side. Near the transition region higher order modes are excited, but they have vanished at the reference plane far from the discontinuity (Fig. 7.2). Hence, only the dominant mode needs to be considered.

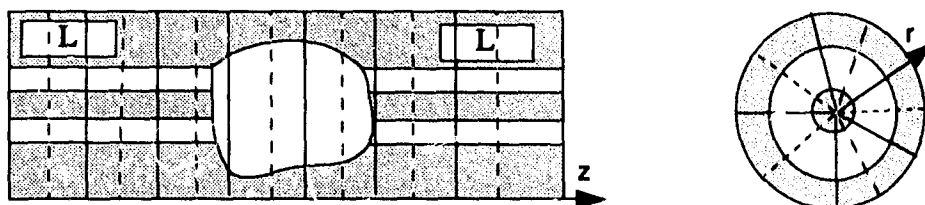


Figure 7.3 Waveguide discontinuities in cylindrical coordinates.

The boundary conditions at the input port ($z=0$) are [57]

$$E_z|_{z=0} = (1-R)e_{zi} \quad (7.9)$$

$$\frac{\partial H_z}{\partial z}|_{z=0} = -j\beta_i(1-R)h_{zi}, \quad (7.10)$$

and at the output port ($z=L$) are

$$E_z|_{z=L} = Te_{zo}, \quad (7.11)$$

$$\frac{\partial H_z}{\partial z}|_{z=L} = -j\beta_o Th_{zo}, \quad (7.12)$$

where e_{zi} (e_{zo}), h_{zi} (h_{zo}), and β_i (β_o) are the modal fields and the propagation constant of the input (output) port. R and T are the unknown voltage reflection coefficient and transmission coefficient, respectively.

Introducing the above boundary conditions into the finite difference expression for

the z derivatives of the E_z and H_z field yields:

$$h_z \frac{\partial E_z}{\partial z} \leftrightarrow ([D_z] \otimes [I_x]) E_z + T [I_x] E_{zo} - (1 - R) [I_x] E_{zi}, \quad (7.13)$$

$$h_z \frac{\partial H_z}{\partial z} = - \left(r_{ze} [D_z] r_{zh}^{-1} \otimes [I_x] \right) H_z, \quad (7.14)$$

$$h_z^2 \frac{\partial^2 E_z}{\partial z^2} \leftrightarrow - [P_{ze}] E_z - T \left([D_z]' \otimes [I_x] \right) E_{zo} - (1 - R) \left([D_z]' \otimes [I_x] \right) E_{zi}, \quad (7.15)$$

$$h_z^2 \frac{\partial^2 H_z}{\partial z^2} \leftrightarrow - [P_{zh}] H_z + T [I_x] H'_{zo} - (1 - R) [I_x] H'_{zi}, \quad (7.16)$$

where \otimes denotes the Kronecker product. To simplify the description of the method, the following formulations are in form of Kronecker product. The input and output field components (subscript i for input and o for output) are denoted as follows:

$$E_{zi} = \begin{bmatrix} 1 \\ 0 \end{bmatrix} \otimes e_{zi}, \quad E_{zo} = \begin{bmatrix} 0 \\ 1 \end{bmatrix} \otimes e_{zo}, \quad (7.17)$$

$$H_{zi} = j\beta_i \begin{bmatrix} 1 \\ 0 \end{bmatrix} \otimes h_{zi}, \quad H_{zo} = j\beta_o \begin{bmatrix} 0 \\ 1 \end{bmatrix} \otimes h_{zo}. \quad (7.18)$$

The transformation matrices are also expressed by a Kronecker product as follows:

$$[P_{ze}] = [D_z]' [D_z] \otimes [I_x], \quad [P_{zh}] = [D_z] [D_z]' \otimes [I_x],$$

where $[D_z]$ is given in Chapter 6.

Since the discretization along the θ -direction is the same as that used in Chapter 5 and Chapter 6, the same transformation matrices described there can be used to transfer a set of discretized Maxwell's equations, similar to that in eq. (5.13), into an uncoupled and ordinary set of equations:

$$\frac{d}{rdr} \left(r \frac{d\Phi_{ki}}{dr} \right) + \left(\chi_{ik}^2 - \frac{\mu_k^2}{r^2} \right) \Phi_{ki} = \begin{cases} \frac{1}{h_z^2} [T_e]^i [D_z]^i \{ TE_{zo} - (1-R) E_{zi} \} \text{ for e-lines} \\ -\frac{1}{h_z^2} [T_h] \{ TH'_{zo} - (1-R) H'_{zi} \} \text{ for h-lines} \end{cases}.$$

$$\chi_{ik}^2 = \left(k_0^2 + \frac{\delta_{ii}}{h_z^2} \right), \quad \mu_k = \frac{2 \sin(\alpha_k/2)}{h}, \quad (7.19)$$

where $[T_e]$ and $[T_h]$ are the normalized eigenvector matrices of $[P_{ze}]$ and $[P_{zh}]$, and μ_k and δ_{ii} are their eigenvalues, respectively. The general forms for these eigenvalues are given in Chapter 5 and Chapter 6.

For inhomogeneous structures, first, eq. (7.19) can be solved analytically in each uniform region. Then, all the other tangential field components satisfy the boundary conditions at the interfaces between uniform regions (Chapter 5 and Chapter 6). Therefore, a set of ordinary differential equations in the transformed domain are obtained, which can be transformed back to the spatial domain to a set of inhomogeneous equations:

$$\begin{bmatrix} J_x \\ J_z \end{bmatrix} = Y \begin{bmatrix} E_x \\ E_z \end{bmatrix} - (1-R) Y_i \begin{bmatrix} E_{xi} \\ E_{zi} \end{bmatrix} - T Y_o \begin{bmatrix} E_{xo} \\ E_{zo} \end{bmatrix}. \quad (7.20)$$

After taking into account that the currents vanish on non-metal (dielectric) interfaces and tangential fields vanish on conductor regions, a reduced matrix equation will result. If the line number in z-direction is N_e for e-lines and N_h for h-lines, respectively, we have a set of total $N_e + N_h$ linear equations but with $N_e + N_h + 2$ unknowns since R and T are treated as unknowns. To obtain two additional equations we consider the currents at the planes inside the calculation domain at $z=h_{z1}$ and $z=L-h_{zN}$. At these planes,

$$J_z|_{z=h_{z1}} = \left(e^{-j\beta_0 h_{z1}} - R e^{j\beta_0 h_{z1}} \right) J_{zi}, \quad (7.21)$$

$$J_z|_{z=L-h_{zN}} = T e^{j\beta_0 h_{zN}} J_{zo}, \quad (7.22)$$

where J_{zi} and J_{zo} are the z-direction modal current distribution functions of input and output ports, respectively.

Therefore two more equations are added to eq. (7.21) which can then be solved by Gaussian elimination to get the reflection coefficient R and the transmission coefficient T. Therefore, all the S-parameters or equivalent circuit parameters can be obtained.

7.3 Numerical results

To illustrate the potential of the above procedures, first of all, a coaxial step filter is analyzed in Fig. 7.4. A relatively coarse discretization is used with 5 lines in wave propagation direction and 12 lines in angular direction for each section. A typical calculation for each frequency is about 18 minutes on a SunSparc workstation. Convergence test shows that further increase of the number of lines does not improve the accuracy. The results agree reasonably well with the experimental data [92,85]. If structural symmetry is considered, it is expected that the algorithm becomes considerably faster.

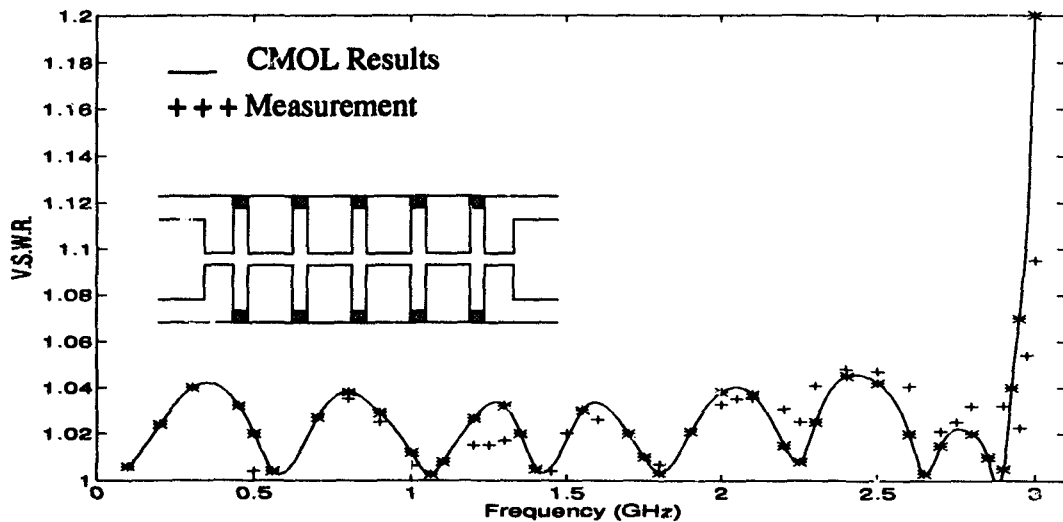


Figure 7.4 Coaxial Low-Pass Filter

Another example is shown in Fig. 7.6, where a coaxial step discontinuity is discretized by the CMoL with a number of straight lines, utilizing hybrid (inhomogeneous)

boundary conditions to both ends. The equivalent circuit can be approximated as a shunt capacitance.

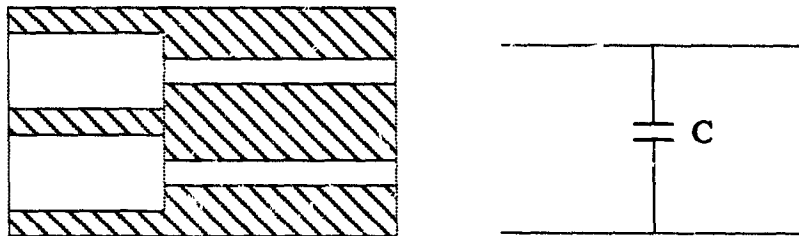


Figure 7.5 Discretization of discontinuity of coaxial line steps and its equivalent circuit

The calculation results are shown in Fig. 7.6 for a simple discontinuity of concentric steps in width. The results are compared to literature for a case when $\tau=r_3/r_1=10$ ([92,85]). Due to the symmetry and simplicity of the structure, the typical cpu time consumed is only about 1-10 seconds on a Sun Sparc workstation.

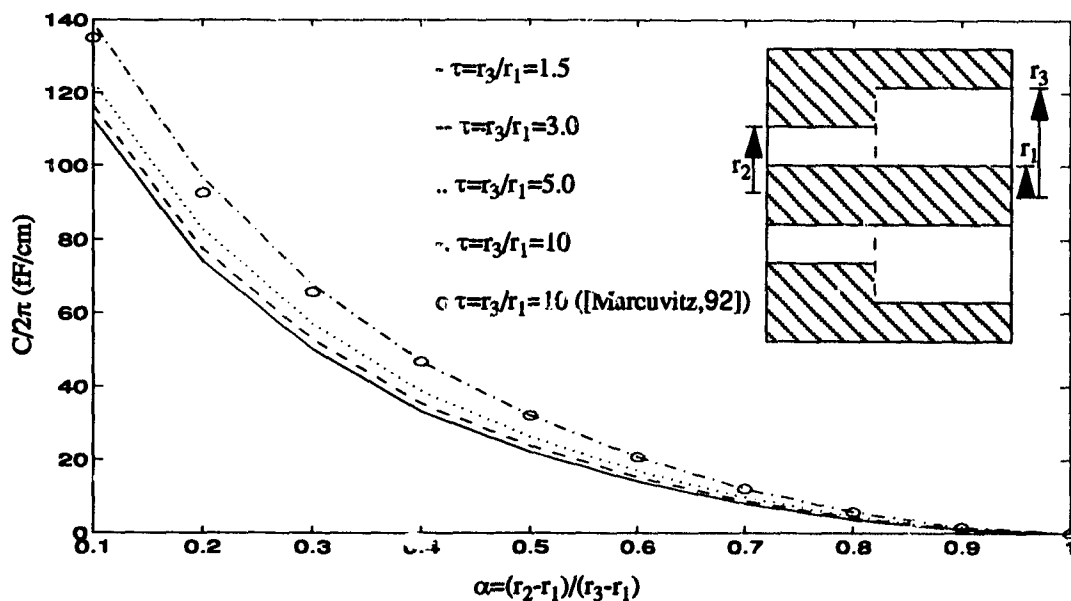


Figure 7.6 Capacitance of coaxial line steps versus $\alpha=(r_2-r_1)/(r_3-r_1)$

The last example is a circular waveguide bandpass filter which was originally designed by the mode matching method (MMM) [84]. Totally 80 lines in wave propaga-

tion direction and 35 lines in angle direction are used to discretize the whole calculation domain. About 40 minutes are consumed on a SunSparc workstation.

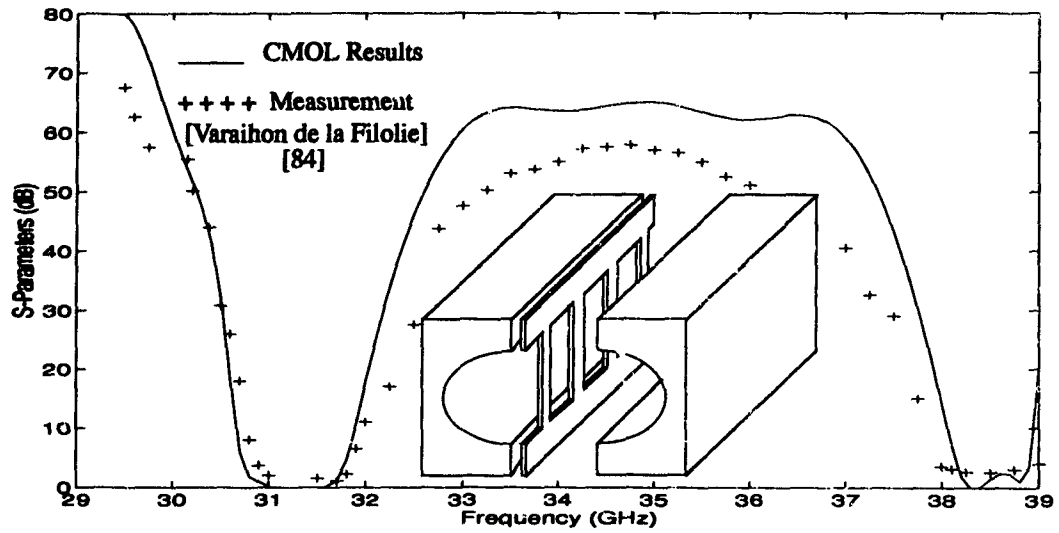


Figure 7.7 Circular Waveguide Band-Pass Filter calculated by CMOL.

Chapter 8

Conclusion and future work

The Finite Difference Time Domain (FDTD) method and the Method of Lines (MoL) are applied to model electromagnetic fields in the microwave integrated circuits (MIC) as well as waveguide components. A modified FDTD grading scheme with enhanced efficiency and improved accuracy has been presented. The modified FDTD method is then used to a variety of microwave circuits including 2D and 3D problems. For 2D analysis, this thesis proposes a novel full-wave FDTD algorithm and its modified versions. This new 2D FDTD method reduces original memory space and CPU run time requirements that are key problems of the method. In second part of the thesis, the MoL is developed and modified to analyze a class of microwave circuits. First of all, a higher order scheme is proposed for discretized Helmholtz equation, continuity equations, and edge conditions. This new algorithm can have better accuracy with the same memory space and CPU run time requirements. From another point of view, it reduces matrix size and computational time greatly with a same accurate result. Finally, a cylindrical MoL is proposed with general cases. The higher order schemes are also developed in cylindrical coordinates.

To continue the work in this thesis, first of all, the MoL can be combined with the

mode matching technique to deal with many microwave circuits and components. The efficiency and accuracy of the MoL will be greatly improved.

Secondly, if the FDTD method can adopt the idea from the semi-analytical MoL in some space direction or the time variable, the efficiency and accuracy of the FDTD method can be improved.

Finally, the stability and dispersion relations of the FDTD method applied to superconductor applications have not been derived explicitly. These stability and numerical dispersion relation are very important especially for nonlinear analysis. People in this field have been using trial-and-error method to get around this difficult question. This task is out of context and beyond my ability at this moment. However, with certain help from mathematicians, this topic needs to be done.

These three topics will be studied in the future research.

Bibliography

- [1] T. Itoh (Ed), *Numerical Techniques for Microwave and Millimeter-wave Passive Structures*, John Wiley & Sons, New York, 1989.
- [2] K. S. Yee, "Numerical solution of initial boundary value problems involving Maxwell's equations in isotropic media, *IEEE Trans. Antennas Propagat.*, vol. AP-14, no.5, pp.302-307, May 1966.
- [3] A. Taflove and M. E. Brodwin, "Numerical solution of steady-state electromagnetic scattering problems using the time-dependent Maxwell's equations," *IEEE Trans. Microwave Theory Tech.*, vol.MTT-23, no.8, pp.623-630, Aug. 1975.
- [4] G. Mur, "Absorbing boundary conditions for the finite-difference approximation of the time-domain electromagnetic-field equations," *IEEE Trans. Electromagn. Compat.*, vol.EMC-23, no.11, pp.377-382, Nov. 1981.
- [5] S. Yoshida and I. Fukai, "Transient analysis of a stripline having a corner in three-dimensional space," *IEEE Trans. Microwave Theory Tech.*, vol.MTT-32, pp.491-498, May 1984.
- [6] B. Engquist and A. Majda, "Absorbing boundary conditions for the numerical simulation of waves," *Math. Comp.*, vol.31, pp.629-651, 1977.
- [7] Z. Liao, H. L. Wong, B. Yang, and Y. Yuan, "A transmission boundary for transient wave analysis," *Scientia Sinica, Series A*, vol.XXVII, no.10, pp.1062-1076, Oct. 1984.
- [8] R. L. Higdon, "Absorbing boundary conditions for difference approximations to the multi-dimensional wave equation," *Math. Comput.*, vol.47, no.176, pp.437-459, Oct. 1986.
- [9] J. Fang and K. K. Mei, "Super-absorbing boundary algorithm for solving electromagnetic problems by time-domain finite difference method," *1988 IEEE AP-S/URSI Intern. Symp.*, pp.472-475, Syracuse, NY, June 6-10, 1988.
- [10] C.E. Reuter, R.M. Joseph, E.T. Thiele, D.S. Katz, and A. Taflove, "Ultrawideband absorbing boundary condition for termination of waveguiding structures in FD-TD simulation," *IEEE Microwave and Guided Wave Letters*, vol.4, no.10, pp.334-336, Oct. 1994.

- [11] J.-P. Berenger, "A perfectly matched layer for free-space simulation in finite difference computer codes," EUROEM'94, Bordeaux, France, May 1994.
- [12] D. S. Katz, E. T. Thiele, and A. Taflove, "PML in 3D FDTD," *IEEE Microwave and Guided Wave Letters*, vol.4, no.8, pp.268-270, Aug. 1994.
- [13] J. Fang, "Absorbing boundary conditions applied to model wave propagation in microwave integrated-circuits," submitted to *IEEE Trans. Microwave Theory Tech.*
- [14] D. H. Choi and W. J. R. Hoefer, "The finite difference time domain method and its application to eigenvalue problems," *IEEE Trans. Microwave Theory Tech.*, vol.MTT-34, no.12, pp.1464-1470, Dec. 1986.
- [15] X. Zhang, J. Fang, K. K. Mei, and Y. Liu, "Calculations of dispersive characteristics of microstrips by the time domain finite difference method," *IEEE Trans. Microwave Theory Tech.*, vol.MTT-36, No.2, pp.263-267, Feb. 1988.
- [16] Z. Bi, K. L. Wu, C. Wu, and J. Litva, "A dispersive boundary condition for microstrip component analysis using the FD-TD method," *IEEE Trans. Microwave Theory Tech.*, vol.MTT-40, no.3, pp.774-777, Apr. 1992.
- [17] B. Houshmand, T. W. Huang and T. Itoh, "Microwave structure characterization by a combination of FDTD and system identification," *IEEE Microwave Guided Wave Letters*, vol.3, no.8, pp.262-264, Aug. 1993.
- [18] J. Chen, C. Wu, K. L. Wu and J. Litva, "Combining and autoregressive (AR) spectral estimation model with the FD-TD algorithm for improved computational efficiency," *1993 IEEE MTT-S International Microwave Symposium Digest*, pp.749-752, Atlanta, Georgia, 1993.
- [19] W. Kuempel and I. Wolff, "Digital signal processing of time-domain field simulation using the system identification method," *1992 IEEE MTT-S International Microwave Symposium Digest*, pp.793-796, Albuquerque, New Mexico, 1992.
- [20] M. L. Van Blaricum and R. Mittra, "Problems and solutions associated with Prony's method for processing transient data," *IEEE Trans. Antenna Propagat.*, vol.AP-26, No.1, pp.174-182, Jan. 1978.
- [21] W. L. Ko and R. Mittra, "A combination of FDTD and Prony's methods for analyzing microwave integrated circuits," *IEEE Trans. Microwave Theory Tech.*, vol.MTT-39, no.12, pp.2176-2181, Dec. 1991.
- [22] J. A. Pereda, L. A. Vielva, A. Vegas and A. Prieto, "Computation of resonant frequencies and quality factors of open dielectric resonators by a combination of the FDTD and Prony's methods," *IEEE Trans. Microwave Guided Wave Lett.*, vol.11, no.11, pp.431-433, Nov. 1992.

- [23] H. Jin, R. Vahldieck, and S. Xiao, "An improved TLM full-wave analysis using a two-dimensional mesh," *1991 IEEE MTT-S Intern. Microwave Symp. Dig.*, pp.675-678, Boston, Jun. 1991.
- [24] H. Jin, R. Vahldieck, and S. Xiao, "A full-wave analysis of arbitrary guiding structures using a two-dimensional TLM mesh," *21th European Microwave Conf. Digest*, pp.370-377, Stuttgart, Germany, Sep. 1991.
- [25] M. C.-Marcysiak and W. K. Gwarek, "A transformed symmetrical condensed node for the effective TLM analysis of guided wave problems," *IEEE Trans. Microwave Theory Tech.*, vol.MTT-41, No.5, pp.820-823, May 1993.
- [26] S. Xiao, R. Vahldieck, and H. Jin, "A fast 2-D FDTD full wave analyzer for arbitrary guided wave structures," *IEEE Microwave and Guided Wave Letters*, vol.2, no.5, pp.165-167, May. 1992.
- [27] S. Xiao, R. Vahldieck, and H. Jin, "A fast two dimensional FDTD full-wave analyzer with adaptive mesh size," *1992 IEEE MTT-S Intern. Microwave Symp. Dig.*, pp., New Mexico, Jun. 1992.
- [28] I. S. Kim and W. J. R. Hoefer, "Numerical dispersion characteristics and stability factor for the TD-FD method," *Electron. Lett.*, vol. 26, no. 7, pp. 485-487, March 1990.
- [29] I. S. Kim and W. J. R. Hoefer, "Effect of the stability factor on the accuracy of two dimensional TD-FD simulation," *1989 IEEE AP-S Symposium Dig.*, pp. 1108-1111, 1989.
- [30] D. H. Choi and J. E. Roy, "The dispersion characteristics of the FD-TD," *1989 IEEE AP-S Symposium Dig.*, pp. 26-29, 1989.
- [31] A. Asi and L. Shafai, "Dispersion analysis of anisotropic inhomogeneous waveguides using compact 2D-FDTD," *Electron. Lett.*, vol.28, no.15, pp.1151-1152, July 1992.
- [32] A. C. Cangellaris, "Numerical stability and numerical dispersion of a compact 2-D/FDTD," *IEEE Microwave and Guided Wave Letters*, vol.3, no.1, pp.3-5, Jan. 1993.
- [33] V. J. Brankovic, D. V. Krupezevic, and F. Arndt, "An efficient 2D graded mesh FDTD algorithm for shielded or open waveguide," *IEEE Trans. Microwave Theory Tech.*, vol.MTT-40, No.12, pp.2272-2277, Dec. 1992.
- [34] S. Xiao and R. Vahldieck, "An efficient 2-D FDTD algorithm using real variables," *IEEE Microwave and Guided Wave Letters*, vol.3, no.5, pp.127-129, May, 1993.

- [35] S. Xiao and R. Vahldieck, "An improved 2D-FDTD algorithm for hybrid mode analysis of quasi-planar transmission lines," *1993 IEEE MTT-S Intern. Microwave Symp. Dig.*, pp.421-424, Atlanta, Georgia, 1993.
- [36] G. W. Zheng and K. S. Chen, "Effects of substrate anisotropy on the dispersion of transient signals in microstrip lines," *Intern. J. Inf. and Mill. Wave*, vol. 11, no.4, pp.489-498, 1990.
- [37] S. Hofschien and I. Wolff, "Improvements of 2-D-FDTD method for the simulation of small CPWs on GaAs using time series analysis," *1994 IEEE MTT-S Intern. Microwave Symp. Dig.*, pp.39-42, Dan Diego, CA, 1994.
- [38] K S. Kunz and L. Simpson, "A technique for increasing the resolution of finite difference solution of the Maxwell equation," *IEEE Trans. Electromagn. Compat.*, vol.EMC-23, no.11 pp.419-422, Nov. 1981.
- [39] I. Kim and W. J. R. Hofer, "A local mesh refinement algorithm for the FDTD method using Maxwell's equations," *IEEE Trans. Microwave Theory Tech.*, vol.MTT-38, no.6, pp.812-815, Jun. 1990.
- [40] S. S. Zivanovic, K. S. Yee, and K. K. Mei, "A subgridding method for the FDTD method to solve Maxwell's equations," *IEEE Trans. Microwave Theory Tech.*, vol.MTT-39, no.3, pp.471-479, March 1991.
- [41] S. Xiao and R. Vahldieck, "An improved 2D-FDTD algorithm for hybrid mode analysis of quasi-planar transmission lines," *1993 IEEE MTT-S International Microwave Symposium Digest*, pp.421-424, Atlanta, Georgia, 1993.
- [42] T. Shibata and E. Sano, "Characterization of MIS structure coplanar transmission lines for investigation of signal propagation in integrated circuits," *IEEE Trans. Microwave Theory Tech.*, vol.MTT-39, no.7, pp.881-889, Jul. 1990.
- [43] M. Rittweger and I. Wolff, "FDTD formulation for transient propagation in superconductors," *1992 IEEE AP-S International Symposium Digest*, pp.1960-1963, 1992.
- [44] S. M. El-Ghazaly, R. B. Hammond, and T. Itoh, "Analysis of superconducting microwave structures: Application to microstrip lines," *IEEE Trans. Microwave Theory Tech.*, vol.MTT-40, no.3, pp.499-508, 1992.
- [45] M. A. Megahed and S. M. El-Ghazaly, "Direct calculation of attenuation and propagation constants in superconducting microwave structures," *1993 IEEE AP-S International Symposium Digest*, pp.1159-1162, Jun. 1993.
- [46] K. K. Mei and G.-C. Liang, "Electromagnetics of superconductors," *IEEE Trans. Microwave Theory Tech.*, vol.MTT-39, no.9, pp.1545-1552, 1991.

- [47] J.-G. Ma and I. Wolff, "Modeling the microwave properties of superconductors," to be published in *IEEE Trans. Microwave Theory Tech.*
- [48] S. Xiao and R. Vahldieck, "Signal Propagation in Conductor-backed superconductor coplanar waveguide", *24th EuMC Digest*, pp.384-389, Cannes, France, 1994.
- [49] S. Xiao and R. Vahldieck, "An extended 2D-FDTD for lossy analysis of quasi-planar transmission lines," *1994 IEEE AP-S International Symposium Digest*, pp.421-424, Seattle, Washington, 1994.
- [50] O. R. Baicocchi, K.-S. Kong, H. Ling, and T. Itoh, "Effects of superconducting losses in pulse propagation on microstrip lines," *IEEE Microwave and Guided Wave Letters*, pp.2-4, vol.1, no.1, Jan., 1991.
- [51] J. F. Whitaker, R. Sobolewski, D. R. Dykaar, T. Hsiang and G. A. Mourou, "Propagation model for ultrafast signals on superconducting dispersive striplines," *IEEE Trans. Microwave Theory Tech.*, vol.MTT-36, pp.227-284, 1988.
- [52] T. Kitazawa, "Extended spectral domain approach," *Dig. MWE*, pp.221-226, Tokyo, Japan, Sept. 1992.
- [53] W. H. Haydl, T. Kitazawa, J. Braunstein, R. Bosch, and M. Schlechtweg, "Millimeterwave coplanar transmission lines on gallium arsenide, indium phosphide and quartz with finite metallization thickness," *1991 IEEE MTT-S Intern. Microwave Symp. Dig.*, pp.691-694, Boston, Jun., 1991.
- [54] K. Wu, M. Yu, R. Vahldieck, "Rigorous analysis of 3-D planar circuits discontinuities using the space-spectral domain approach (SSDA)," *IEEE Trans. Microwave Theory Tech.*, Special Issue on CAD, vol.MTT-40, no.7, pp.1475-1483, July 1992. (collected also in the IEEE press book, *Analysis and Design of Planar Microwave Components*, Edited by K. Gupta and M. K. Abouzahra).
- [55] U. Schulz, *A new technique for the analysis of planar microwave structures*, Ph.D. Thesis, FernUniv., Hagen, Germany, 1980.
- [56] U. Schulz, "On the edge condition with the method of lines in planar waveguides," *AEU*, vol 34, pp. 176-178, 1980.
- [57] S. B. Worm, "Full-wave analysis of discontinuities in planar waveguides by the method of lines using a source approach," *IEEE Trans. Microwave Theory Tech.*, vol. MTT-38, pp.1510-1514, 1990.
- [58] H. Diestel and S. B. Worm, "Analysis of hybrid field problem by the method of lines with nonequidistant discretization," *IEEE Trans. Microwave Theory Tech.*, vol. MTT-32, pp.633-638, 1984.

- [59] A. Dreher and R. Pregla, "Analysis of planar waveguides with the Method of lines and absorbing boundary conditions", *IEEE Microwave and Guided Wave Letters*, vol.1, pp.138-140, 1991.
- [60] S. B. Worm and R. Pregla, "Hybrid mode analysis of arbitrarily shaped planar microwave structures by the method of lines," *IEEE Trans. Microwave Theory Tech.*, vol. 32, no. 2, pp. 191-196, Feb. 1984.
- [61] K. Wu and R. Vahldieck, "Hybrid-mode analysis of homogeneous and inhomogeneous doped low-loss slow-wave coplanar transmission lines," *IEEE Trans. Microwave Theory Tech.*, vol. 39, no. 8, pp. 1348-1360, Aug. 1991.
- [62] M. Thorburn, A. Agostron, and V. K. Tripathi, "Computation of frequency-dependent propagation characteristics of microstriplike propagation structures with discontinuous layers," *IEEE Trans. Microwave Theory Tech.*, vol. 38, no. 2, pp. 148-153, Feb. 1990.
- [63] M. Thorburn, A. Biswas, and V. K. Tripathi, "Application of method of lines to cylindrical inhomogeneous propagation structures," *Electronics Letters*, vol.26, no.3, pp.170-171, 1990.
- [64] S.-J. Chung and T.-R. Chrag, "Full wave analysis of discontinuities in conductor backed coplanar waveguides using method of lines," *IEEE Trans. Microwave Theory Tech.*, vol.MTT-41, pp.1601-1605, Sept. 1993.
- [65] Y. Chen and B. Becker, "Study of microstrip step discontinuities on bianisotropic substrates using the method of lines and transverse resonance technique," *IEEE Trans. Microwave Theory Tech.*, vol.MTT-42, pp.1945-1950, Oct. 1994.
- [66] Y. Xu, Application of method of lines to solve problems in the cylindrical coordinates," *Microwave and Optical Technology Letters*, vol.1, no.5, pp.173-175, July 1988.
- [67] K. Wu and R. Vahldieck, "The method of lines applied to planar transmission lines in circular and elliptical waveguides," *IEEE Trans. Microwave Theory Tech.*, vol. 37, no. 12, pp. 1958-1963, Dec. 1989.
- [68] V. A. Labay and J. Bornemann, "Matrix singular decomposition for pole-free solutions of homogeneous matrix equation as applied to numerical modeling methods," *IEEE Microwave and Guided Wave Letters*, vol. 2, no. 2, pp. 55-57, 1992.
- [69] S. Xiao and R. Vahldieck, "Full-wave characterization of cylindrical layered multiconductor transmission lines using the MoL," *1994 IEEE MTT-S International Microwave Symposium Digest*, pp.149-152, San Diego, CA, USA, May 1994.

- [70] S. Xiao, R. Vahldieck, H. Jin and Z. Cai, "A modified MoL algorithm with faster convergence and improved computational efficiency," *1991 IEEE MTT-S International Microwave Symposium Digest*, pp. 357-360, Boston, Jun. 1991.
- [71] R. E. Collin, *Field Theory of Guided Waves*, New York, McGraw-Hill, 1960.
- [72] N. Kishi and T. Okoshi, "Proposal for a boundary-integral method without using Green's function," *IEEE Trans. Microwave Theory Tech.*, vol. 35, no. 10, pp. 887-892, Oct. 1987.
- [73] M. Swaminathan, T. K. Sarkar, and A. T. Adams, "Computation of TM and TE modes in waveguides based on a surface integral formulation," *IEEE Trans. Microwave Theory Tech.*, vol. 40, no. 2, pp. 285-297, Feb. 1992.
- [74] L. R. Zeng and Y. X. Wang, "Accurate solutions of elliptical and cylindrical striplines and microstrip lines," *IEEE Trans. Microwave Theory Tech.*, vol. 34, no. 2, pp. 259-265, Feb. 1986.
- [75] C. J. Reddy and M. D. Deshpande, "Analysis of cylindrical stripline with multilayer dielectrics," *IEEE Trans. Microwave Theory Tech.*, vol. 34, no. 6, pp. 701-706, June 1986.
- [76] C. H. Chan and R. Mittra, "Analysis of a class of cylindrical multiconductor transmission lines using an iterative approach," *IEEE Trans. Microwave Theory Tech.*, vol. 35, no. 4, pp. 415-424, April 1987.
- [77] S. S. Bedir and I. Wolff, "Extending the use of conformal mapping technique for the calculation of the quasi-TEM parameters of several cylindrical and wrapped transmission lines," *1989 IEEE MTT-S Intern. Microwave Sym. Dig.*, pp.1127-1130, Long Beach, CA, 1989.
- [78] N. Alexopoulos and A. Nakatani, "Cylindrical substrate microstrip line characterization," *IEEE Trans. Microwave Theory Tech.*, vol. 35, no. 9, pp. 843-849, Sept. 1987.
- [79] A. Nakatani and N. Alexopoulos, "Coupled microstrip line on cylindrical substrate," *IEEE Trans. Microwave Theory Tech.*, vol. 35, no. 12, pp. 1392-1398, Sept. 1987.
- [80] A.E. Atia and A.E. William, "New types of waveguide band pass filters for satellite transponders," *Comsat. Tech. Rev. 1*, no. 1, pp.21-42, 1971.
- [81] X.-P. Liang and K.A. Zaki, and A.E. Atia, "Dual mode coupling by square corner cut in resonators and filters," *IEEE Trans. Microwave Theory Tech.*, vol.MTT-39, pp.1307-1312, Aug. 1991.

- [82] X.-P. Liang and K.A. Zaki, "Modeling of cylindrical dielectric resonators in rectangular waveguides and cavities," *IEEE Trans. Microwave Theory Tech.*, vol.MTT-39, pp.2174-2181, Dec. 1993.
- [83] S. Xiao and R. Vahldieck, "Full-wave characterization of cylindrical layered multiconductor transmission lines using the MoL," *1994 IEEE MTT-S International Microwave Symposium Digest*, pp. 149-152, San Diego, CA, USA, May 1994.
- [84] B. Varaihon de la Filolie, *Field theory analysis of rectangular and circular waveguide discontinuities for filters, multiplexers and matching networks*, Ph.D dissertation, University of Victoria, Victoria, Canada, 1992.
- [85] G. Matthaei, L. Young, and E.M.T. Jones, *Microwave Filters, Impedance-matching networks, and Coupling Structures*, Dedham, MA: Artech House, 1980.
- [86] M. Naghed and I. Wolff, "A 3D finite difference calculation of equivalent capacitances of Coplanar waveguide discontinuities," *1990 IEEE MTT-S International Microwave Symposium Digest*, pp. 1143-1146, USA, May 1990.
- [87] M. Naghed and I. Wolff, "A new method for the calculation of the equivalent inductances of Coplanar waveguide discontinuities," *1991 IEEE MTT-S International Microwave Symposium Digest*, pp. 747-750, Boston, MA, USA, May 1991.
- [88] K. A. Zaki, C. Chen, and A. E. Atia, "A circuit model of probes in dual-mode cavities," *IEEE Trans. Microwave Theory Tech.*, vol.MTT-36, pp.1740-1746, Dec. 1988.
- [89] R. L. Eisenhart, P. T. Greiling, L. K. Roberts, and R. S. Robertson, "A useful equivalence for a coaxial waveguide junction," *IEEE Trans. Microwave Theory Tech.*, vol.MTT-26, pp.172-175, March 1978.
- [90] J.-F Liang and K. A. Zaki, "Coaxial probe modeling in waveguides and cavities," *1992 IEEE MTT-S International Microwave Symposium Digest*, pp. 115-118, USA, May 1992.
- [91] F. R. Gantmacher, "Matrix Theory," Chelsen Pub. Com., NY, 1960.
- [92] N. Marcuvitz (Ed), *Waveguide Handbook*, New York: McGraw-Hill, 1951.
- [93] R. S. Weis and T. K. Gaylord, "Lithium Niobate: Summary of physical properties and cristal structure," *Appl. Phys. A*, vol.37, pp.191-203, 1985.
- [94] O. G. Ramer, "Integrated optic electrooptic modulator analysis," *IEEE J. Quantum Electron.*, vol.QE-18, pp.386-392, 1982.

- [95] Y.J. He and S.-F. Li, "Analysis of arbitrary cross-section microstrip using the method of lines," *IEEE Trans. Microwave Theory Tech.*, vol.42, pp.162-164, Jan. 1994.
- [96] R. S. Chen, D. G. Fang, and X.G. Li, "Analysis of open microstrip lines by MoL," *Inter. J. Microwave and Millimeter-Wave Computer-aided Eng.*, vol.3, no.2, pp.109-113, 1993.
- [97] A. Kornatz and Pregla, "Increase of the order of approximation and improvement of the interface conditions for the method of lines," *IEEE/OSA J. Lightwave Tech.*, vol.11, pp.249-251, Fe., 1993.

Appendices

.

Appendix A

Normalized Yee's 3D FDTD scheme

The Yee's 3D FDTD scheme [15] can be normalized by the free space impedance

$$Z = \sqrt{\mu/\epsilon}$$

$$E_{x,y,z}^n(i, j, k) \Leftrightarrow E_{x,y,z}^n(i, j, k) \sqrt{Z}, \quad (\text{A.1})$$

$$E_{x,y,z}^n(i, j, k) \Leftrightarrow E_{x,y,z}^n(i, j, k) \sqrt{Z}. \quad (\text{A.2})$$

From Maxwell's equations one obtains

$$\begin{aligned} H_x^{n+0.5}(i, j, k) = & H_x^{n-0.5}(i, j, k) - s(E_z^n(i, j+1, k) - E_z^n(i, j, k) \\ & - E_y^n(i+1, j, k) + E_y^n(i, j, k)), \end{aligned} \quad (\text{A.3})$$

$$\begin{aligned} H_y^{n+0.5}(i, j, k) = & H_y^{n-0.5}(i, j, k) - s(E_x^n(i, j, k+1) - E_x^n(i, j, k) \\ & - E_z^n(i+1, j, k) + E_z^n(i, j, k)), \end{aligned} \quad (\text{A.4})$$

$$\begin{aligned} H_z^{n+0.5}(i, j, k) = & H_z^{n-0.5}(i, j, k) - s(E_y^n(i+1, j, k) - E_y^n(i, j, k) \\ & - E_x^n(i, j+1, k) + E_x^n(i, j, k)), \end{aligned} \quad (\text{A.5})$$

$$\begin{aligned} E_x^{n+1}(i, j, k) = & E_x^{n-1}(i, j, k) + s(H_z^{n+0.5}(i, j, k) - H_z^{n+0.5}(i, j-1, k) \\ & - H_y^{n+0.5}(i, j, k) + H_y^{n+0.5}(i, j, k-1)), \end{aligned} \quad (\text{A.6})$$

$$E_y^{n+1}(i, j, k) = E_y^{n-1}(i, j, k) + s(H_x^{n+0.5}(i, j, k) - H_x^{n+0.5}(i, j, k-1) - H_z^{n+0.5}(i, j, k) + H_z^{n+0.5}(i-1, j, k)), \quad (\text{A.7})$$

$$E_z^{n+1}(i, j, k) = E_z^{n-1}(i, j, k) + s(H_y^{n+0.5}(i, j, k) - H_y^{n+0.5}(i-1, j, k) - H_x^{n+0.5}(i, j, k) + H_x^{n+0.5}(i, j-1, k)), \quad (\text{A.8})$$

where $s = c\Delta t/\Delta h$. c is the speed of light. Δt and Δh are, respectively, the time step and the space step in all spatial directions ($\Delta x = \Delta y = \Delta z = \Delta h$ is assumed). The stability condition requires

$$s \leq 1/\sqrt{3}. \quad (\text{A.9})$$

Appendix B

Stability criterion and numerical dispersion of 2D FDTD

B.1 Real-variable 2D FDTD

B.1.1 Stability criterion for the real variable 2D FDTD

In order to derive the stability criterion, we must know the amplification matrix first. Let's assume that the electric and magnetic field components will have a form of

$$A_{x,y,z} = A_{0x,y,z} \exp \{ j(\omega n \Delta t - k_x i \Delta x - k_y k \Delta y) \}, \quad (\text{B.1})$$

where $A = E$ or H ; n ($n=1,2,3,\dots,M$), i ($i=1,2,3,\dots,M$) and k ($k=1,2,3,\dots,N$) are respectively the time and space discretization indexes; k_x and k_y are wave numbers respectively along the x - and y -directions. Δt , Δx , and Δy are the time and space discretization steps, respectively. We normalize the electric and magnetic fields by using the wave impedance and substitute eq. (B.1) into eq. (2.3-2.8)

$$H_x^{n+0.5} = H_x^{n-0.5} + 2jYE_z^n - 2ZE_y^n, \quad (\text{B.2})$$

$$H_y^{n+0.5} = H_y^{n-0.5} - 2jXE_z^n + 2ZE_x^n, \quad (\text{B.3})$$

$$H_x^{n+0.5} = H_x^{n-0.5} + 2jXE_y^n - 2jYE_x^n, \quad (\text{B.4})$$

$$E_x^{n+1} = E_x^n - 2jYH_z^{n+0.5} - 2ZH_y^{n+0.5}, \quad (\text{B.5})$$

$$E_y^{n+1} = E_y^n + 2jXH_z^{n+0.5} + 2ZH_x^{n+0.5}, \quad (\text{B.6})$$

$$E_z^{n+1} = E_z^n + 2jYH_x^{n+0.5} - 2jXH_y^{n+0.5}, \quad (\text{B.7})$$

where $S_x = v\Delta t/\Delta x$, $S_y = v\Delta t/\Delta y$, $v = 1/\sqrt{\mu\epsilon}$, and

$$X = S_x \sin \frac{k_x \Delta x}{2}; \quad Y = S_y \sin \frac{k_y \Delta y}{2}; \quad Z = v\Delta t\beta/2. \quad (\text{B.8})$$

From (B.5) and (B.7), one obtains

$$E_x^{n+0.5} = E_x^{n-0.5} - 2jYH_z^n - 2ZH_y^n, \quad (\text{B.9})$$

$$E_y^{n+0.5} = E_y^{n-0.5} + 2jXH_z^n + 2ZH_x^n, \quad (\text{B.10})$$

$$E_z^{n+0.5} = E_z^{n-0.5} + 2jYH_x^n - 2jXH_y^n. \quad (\text{B.11})$$

From (B.9)+(B.2), (B.10)+(B.3), and (B.11)-(B.4) one obtains

$$(H_x + E_x)^{n+0.5} = (H_x + E_x)^{n-0.5} + 2jY(E_z - H_z)^n - 2Z(H_y + E_y)^n, \quad (\text{B.12})$$

$$(H_y + E_y)^{n+0.5} = (H_y + E_y)^{n-0.5} - 2jX(E_z - H_z)^n + 2Z(H_x + E_x)^n, \quad (\text{B.13})$$

$$(E_z - H_z)^{n+0.5} = (E_z - H_z)^{n-0.5} - 2jX(H_y + E_y)^n + 2jY(E_x - H_x)^n. \quad (\text{B.14})$$

The above equations can be written in matrix form as

$$\begin{bmatrix} (H_x + E_x) \\ (H_y + E_y) \\ j(H_z - E_z) \end{bmatrix}^{n+0.5} = \begin{bmatrix} (H_x + E_x) \\ (H_y + E_y) \\ j(H_z - E_z) \end{bmatrix}^{n-0.5} + \begin{bmatrix} 0 & -2Z & -2Y \\ 2Z & 0 & 2X \\ 2Y & -2X & 0 \end{bmatrix} \begin{bmatrix} (H_x + E_x) \\ (H_y + E_y) \\ j(H_z - E_z) \end{bmatrix}^n. \quad (\text{B.15})$$

Denoting

$$U^n = \begin{bmatrix} (H_x + E_x) \\ (H_y + E_y) \\ j(H_z - E_z) \end{bmatrix}^n; T = \begin{bmatrix} 0 & -2Z & -2Y \\ 2Z & 0 & 2X \\ 2Y & -2X & 0 \end{bmatrix}; V^n = U^{n-0.5}, \quad (\text{B.16})$$

and introducing a shift of a half time step ($0.5\Delta t$) such as

$$V^{n+0.5} = U^n, \quad (\text{B.17})$$

then from eq. (B.15) one obtains

$$U^{n+0.5} = V^{n-0.5} - TU^n. \quad (\text{B.18})$$

(B.17) and (B.18) can now be written as

$$\begin{bmatrix} U \\ V \end{bmatrix}^{n+0.5} = \begin{bmatrix} -T & I \\ I & 0 \end{bmatrix} \begin{bmatrix} U \\ V \end{bmatrix}^n = A \begin{bmatrix} U \\ V \end{bmatrix}^n, \quad (\text{B.19})$$

where I is an identity matrix. The amplification matrix is as follows

$$A = \begin{bmatrix} -T & I \\ I & 0 \end{bmatrix} \quad (\text{B.20})$$

The eigenvalues λ_i of matrix $[A]$ can be obtained as

$$\begin{vmatrix} \lambda & 0 & 0 \\ 0 & \lambda & 0 \\ 0 & 0 & \lambda \end{vmatrix} \begin{vmatrix} \lambda & -2Z & -2Y \\ 2Z & \lambda & 2X \\ 2Y & -2X & \lambda \end{vmatrix} - \begin{vmatrix} 1 & 0 & 0 \\ 0 & 1 & 0 \\ 0 & 0 & 1 \end{vmatrix} = 0, \quad (\text{B.21})$$

or

$$(\lambda^2 - 1)[(\lambda^2 - 1) + 4\lambda^2(X^2 + Y^2 + Z^2)] = 0.$$

Therefore,

$$\lambda_{1,2} = \pm 1; \lambda_{3,4} = \lambda_{5,6} = \mp j\sqrt{X^2 + Y^2 + Z^2} \pm \sqrt{1 - (X^2 + Y^2 + Z^2)}$$

The stability criterion requires that all the eigenvalues λ_i ($i=1,\dots,6$) of the amplification matrix A must be bounded by a unit circle, that is, $|\lambda_i| \leq 1$. The eigenvalues are bounded if and only if

$$X^2 + Y^2 + Z^2 \leq 1; |\lambda_{3,4,5,6}| = 1 \quad (\text{B.22})$$

Hence, (B.22) gives

$$\left(\frac{v\Delta t}{\Delta x} \sin \frac{k_x \Delta x}{2}\right)^2 + \left(\frac{v\Delta t}{\Delta y} \sin \frac{k_y \Delta y}{2}\right)^2 + \left(\frac{v\Delta t \beta}{2}\right)^2 \leq \left(\frac{v\Delta t}{\Delta x}\right)^2 + \left(\frac{v\Delta t}{\Delta y}\right)^2 + \left(\frac{v\Delta t \beta}{2}\right)^2 \leq 1 \quad (\text{B.23})$$

or

$$v\Delta t \leq \frac{1}{\sqrt{\left(\frac{1}{\Delta x}\right)^2 + \left(\frac{1}{\Delta y}\right)^2 + \left(\frac{\beta}{2}\right)^2}} \quad (\text{B.24})$$

This shows clearly that the stability condition of the real-variable 2D FDTD method is different from that for the standard 2D FDTD in [2]

$$v\Delta t \leq \frac{1}{\sqrt{\left(\frac{1}{\Delta x}\right)^2 + \left(\frac{1}{\Delta y}\right)^2}} \quad (\text{B.25})$$

B.1.2 Numerical dispersion

When we insert (B.1) into (B.2)-(B.7), we have

$$H_x \sin \frac{\omega \Delta t}{2} = Y E_z + j Z E_y; H_y \sin \frac{\omega \Delta t}{2} = -X E_z - j Z E_x; H_z \sin \frac{\omega \Delta t}{2} = X E_y - j Y E_x \quad (\text{B.26})$$

$$E_x \sin \frac{\omega \Delta t}{2} = -Y H_z + j Z H_y; E_y \sin \frac{\omega \Delta t}{2} = X H_z - j Z H_x; E_z \sin \frac{\omega \Delta t}{2} = Y H_x - X H_y \quad (\text{B.27})$$

From the above equations one obtains

$$(H_x + E_x) \sin \frac{\omega \Delta t}{2} = Y (E_z - H_z) + j Z (E_y + H_y) \quad (\text{B.28})$$

$$(H_y + E_y) \sin \frac{\omega \Delta t}{2} = X (H_z - E_z) - j Z (E_x + H_x) \quad (\text{B.29})$$

$$(H_z - E_z) \sin \frac{\omega \Delta t}{2} = X (E_y + H_y) - Y (E_x + H_x) \quad (\text{B.30})$$

or in matrix form

$$\begin{bmatrix} \sin \frac{\omega \Delta t}{2} & -jZ & Y \\ jZ & \sin \frac{\omega \Delta t}{2} & -X \\ Y & -X & \sin \frac{\omega \Delta t}{2} \end{bmatrix} \begin{bmatrix} (H_x + E_x) \\ (E_y + H_y) \\ (H_z - E_z) \end{bmatrix} = D \begin{bmatrix} (H_x + E_x) \\ (E_y + H_y) \\ (H_z - E_z) \end{bmatrix} = 0 \quad (\text{B.31})$$

The non-trivial solution requires that

$$|D| = \begin{bmatrix} \sin \frac{\omega \Delta t}{2} & -jZ & Y \\ jZ & \sin \frac{\omega \Delta t}{2} & -X \\ Y & -X & \sin \frac{\omega \Delta t}{2} \end{bmatrix} = 0 \quad (\text{B.32})$$

From here the numerical dispersion relationship for the real-variable 2D FDTD method is obtained as

$$\left(\sin \frac{\omega \Delta t}{2} \right)^2 = \left(\frac{v \Delta t}{\Delta x} \sin \frac{k_x \Delta x}{2} \right)^2 + \left(\frac{v \Delta t}{\Delta y} \sin \frac{k_y \Delta y}{2} \right)^2 + \left(\frac{v \Delta t \beta}{2} \right)^2 \quad (\text{B.33})$$

It should be noted that the propagation constant β is involved here, which is not the case for the standard 2D FDTD in [2]

$$\left(\sin \frac{\omega \Delta t}{2} \right)^2 = \left(\frac{v \Delta t}{\Delta x} \sin \frac{k_x \Delta x}{2} \right)^2 + \left(\frac{v \Delta t}{\Delta y} \sin \frac{k_y \Delta y}{2} \right)^2. \quad (\text{B.34})$$

B.2 Complex-variable 2D FDTD

Similarly, we can obtain the stability condition and the dispersion relation for the complex-variable 2D FDTD method. The node field distribution and notation are the same as that in the real-variable case, but assuming a phase delay along the wave propagation direction for field components in the Maxwell's equations as

$$A|_{k+1} = A|_k \exp \{-j\beta z\}, \quad A = E_x, E_y, E_z, H_x, H_y, H_z \quad (\text{B.35})$$

Then the complex-variable 2D FDTD with $\Delta z \rightarrow 0$ can be written in a form of the eq. (3) in the literature [26].

B.2.3 Stability

Normalizing the electric and magnetic fields in eq. (B.35) by using the free

space wave impedance and substituting eq. (B.35) into the eq. (3) in [26] yields the following matrix equation

$$\begin{bmatrix} (H_x - jE_x) \\ (H_y - jE_y) \\ (H_z - jE_z) \end{bmatrix}^{n+\frac{1}{2}} = \begin{bmatrix} (H_x - jE_x) \\ (H_y - jE_y) \\ (H_z - jE_z) \end{bmatrix}^{n-\frac{1}{2}} + \begin{bmatrix} 0 & 2Z & -2Y \\ -2Z & 0 & 2X \\ 2Y & -2X & 0 \end{bmatrix} \begin{bmatrix} (H_x - jE_x) \\ (H_y - jE_y) \\ (H_z - jE_z) \end{bmatrix}^n \quad (\text{B.36})$$

where S_x, S_y, S_z, X, Y, Z , and v are exactly the same as in eq. (A.3)-(A.8). Similar algebraic steps as that in the last section will give the stability condition as

$$v\Delta t \leq \frac{1}{\sqrt{\left(\frac{1}{\Delta x}\right)^2 + \left(\frac{1}{\Delta y}\right)^2 + \left(\frac{\beta}{2}\right)^2}} \quad (\text{B.37})$$

This expression is the same as that for the real-variable compact 2D FDTD. Therefore, the complex-variable 2D FDTD with $\Delta z \rightarrow 0$ has the same stability condition as the real-variable 2D FDTD scheme.

B.2.4 Numerical dispersion

Similar to the last section, the numerical dispersion relation is derived from the following matrix equation

$$\begin{bmatrix} \sin \frac{\omega\Delta t}{2} & -jZ & jY \\ jZ & \sin \frac{\omega\Delta t}{2} & -jX \\ -jY & jX & \sin \frac{\omega\Delta t}{2} \end{bmatrix} \begin{bmatrix} (H_x - jE_x) \\ (H_y - jE_y) \\ (H_z - jE_z) \end{bmatrix} = D \begin{bmatrix} (H_x - jE_x) \\ (H_y - jE_y) \\ (H_z - jE_z) \end{bmatrix} = 0 \quad (\text{B.38})$$

in which the parameters S_x, S_y, S_z, X, Y, Z , and v are given in the eq. (A.3)-(A.8). The dispersion relation is obtained as

$$\left(\sin \frac{\omega\Delta t}{2}\right)^2 = \left(\frac{v\Delta t}{\Delta x} \sin \frac{k_x \Delta x}{2}\right)^2 + \left(\frac{v\Delta t}{\Delta y} \sin \frac{k_y \Delta y}{2}\right)^2 + \left(\frac{v\Delta t \beta}{2}\right)^2 \quad (\text{B.39})$$

which is exactly the same as that for the real-variable 2D FDTD, but different from that in [2] for the standard 2D FDTD.

B.3 Numerical results and discussion

In order to test the numerical dispersion of the 2D FDTD method, a simple lossy dielectric-filled rectangular waveguide is analyzed and compared to the analytical solution. Uniform discretization is used. The relative errors for the calculation of the attenuation coefficient for lossy rectangular waveguides using the complex 2D FDTD method [26] are given versus the discretization number along the wide side of the waveguide (Fig. B.1). The accuracy increases with increasing mesh number. The lower order modes will have a more accurate solution. It is also found that the accuracy increases when a higher stability factor is used. The same conclusion applies to the complex 2D FDTD [26]. The upper limit of the stability condition yields the best accuracy and also shortens the computation time. For the real-variable 2D FDTD with $\Delta z = 0$, results are shown in Fig. B.2. In comparison to the complex 2D FDTD approach, the real-variable compact 2D FDTD method saves half the computer memory space and also saves half the computation time.

An interesting point should be also mentioned here namely that the upper limit when $\Delta x = \Delta y = \Delta z = h$ of the stability factor for the complex 2D FDTD algorithm proposed in [26] is smaller than that for the real variable 2D FDTD scheme when $\Delta x = \Delta y = h$ and $\Delta z = 0$ ($1/\sqrt{3}$ for the former case and $1/\sqrt{2}$ for the latter one for uniform discretization in all spatial directions). The stability factor for the latter was chosen 0.65 in Fig. B.2 (a), however the complex 2D FDTD scheme in [26] would be unstable at this value resulting in an overflow of the program. Since the larger stability factor leads to smaller numerical dispersion (Fig. B.1 and Fig. B.2), it is concluded that the real-variable 2D FDTD scheme used in this thesis can have better accuracy than the one in [26] when both methods work at the upper limit of the stability factors. Therefore, in addition to the advantage of much less memory and cpu time requirement for

the real-variable scheme, better results can be obtained. It should be mentioned that the Δz value in the complex 2D FDTD [26] can affect the stability condition and accuracy if selected too large. This can be observed from Fig. B.1, where the smaller relative errors can be achieved with smaller stability factor $s = 0.25$ in Fig. B.1(a) than that with $s = 0.50$ in Fig. B.1(b). The similar conclusion also applies to the real variable 2D FDTD scheme (Fig. B.2).

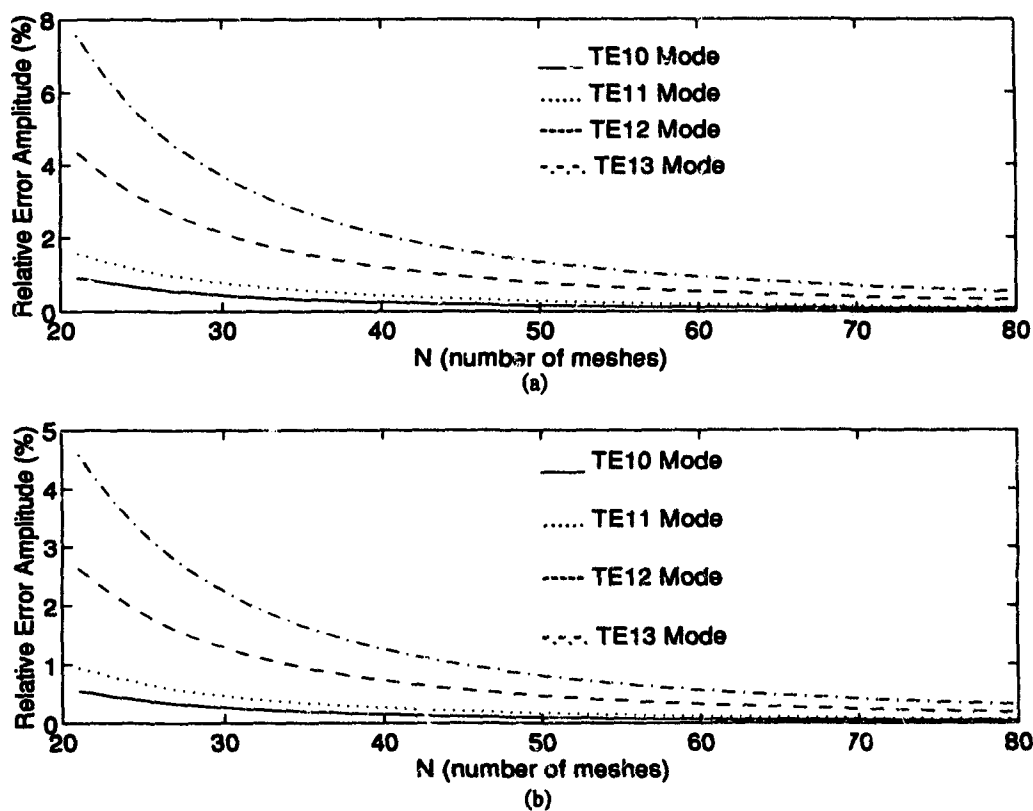


Figure B.1 Effect of the stability factor and the discretization size on the relative error of the complex 2D FDTD [26] calculation of a rectangular waveguide, WR-28 waveguide, $a=7.111$ mm, $b=3.555$ mm, $\epsilon_r=2.2$, $\tan\delta=3.0 \times 10^{-4}$, $\beta=628.0425$, (a) $s=0.50$, (b) $s=0.25$.

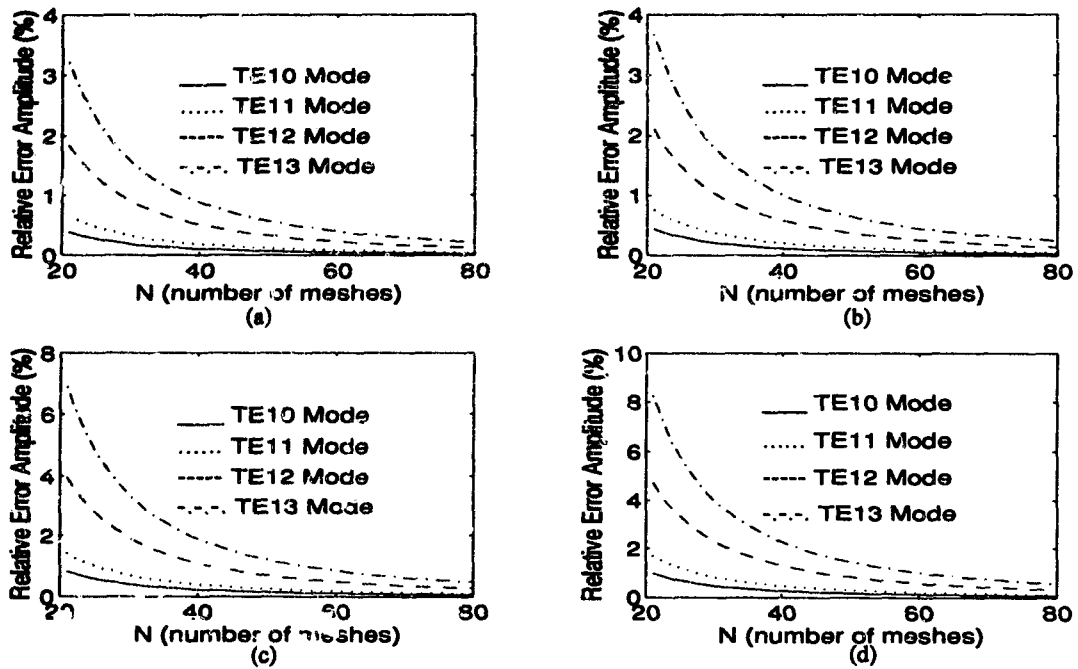


Figure B.2 Effect of the stability factor and the discretization size on the relative error of the real-variable 2D FDTD calculation of a rectangular waveguide, WR-28 waveguide, $a=7.111$ mm, $b=3.555$ mm, $\epsilon_r=2.2$, $\tan\delta=3.0 \times 10^{-4}$, $\beta=628.0425$, (a) $s=0.65$, (b) $s=0.50$, (c) $s=0.25$, (d) $s=0.125$

B.4 Conclusion

The stability criterion and dispersion relationship for various 2D FDTD methods have been derived and studied. Generally the 2D FDTD full-wave methods have stability conditions and dispersion relations that are different from the standard 2D FDTD. It was illustrated that the selection of the stability factors has significant effect on the numerical dispersion.

Appendix C

Eigenmatrix for homogeneous structures

Taking an arbitrary contour homogeneous waveguide in Fig. 5.2 as an example, the finite field values in practice at $r=0$ require $B_k=0$ due to the singularity of the Neumann function $N_{\lambda_k}(k_c r)$ at $r=0$. Assuming an ideal conductivity on the contour leads to (c.f. eq. (5.21))

$$[T] [A_k J_{\lambda_k}(k_c r_k)] = [T] [J_{\lambda_k}(k_c r_k)] \bar{A} = 0 \quad (\text{C.1})$$

for TM modes, where r_k is the radius of the k -th discretization line.

A non-trivial solution of (C.1) requires non-zero coefficients \bar{A} , i.e.,

$$\bar{A} = \begin{bmatrix} A_1 \\ A_2 \\ \cdots \\ A_k \\ \cdots \\ A_N \end{bmatrix} \neq 0 \quad (\text{C.2})$$

then

$$\det([T] [J_{\lambda_k}(k_c R_k)]) = 0 \quad (\text{C.3})$$

where $J_{\lambda_k}(k_c r_k)$ is the λ_k -order Bessel function of $k_c r_k$. The eq. (C.3) will give all the cutoff wavenumbers of TM modes. From eq. (C.1) all the modal field density distributions can be obtained.

The eigenmatrix for TM in eq.(5.22) can be explicitly written as follows

$$\det\{[A]\} = 0. \quad (C.4)$$

where

$$[A]_{TM} = \begin{bmatrix} T_{11}J_{\lambda_1}(k_c r_1) & T_{12}J_{\lambda_2}(k_c r_1) & \dots & T_{1S}J_{\lambda_S}(k_c r_1) & \dots & T_{1N}J_{\lambda_N}(k_c r_1) \\ T_{21}J_{\lambda_1}(k_c r_2) & T_{22}J_{\lambda_2}(k_c r_2) & \dots & T_{2S}J_{\lambda_S}(k_c r_2) & \dots & T_{2N}J_{\lambda_N}(k_c r_2) \\ \dots & \dots & \dots & \dots & \dots & \dots \\ T_{K1}J_{\lambda_1}(k_c r_K) & T_{K2}J_{\lambda_2}(k_c r_K) & \dots & T_{KS}J_{\lambda_S}(k_c r_K) & \dots & T_{KN}J_{\lambda_N}(k_c r_K) \\ \dots & \dots & \dots & \dots & \dots & \dots \\ T_{N1}J_{\lambda_1}(k_c r_N) & T_{N2}J_{\lambda_2}(k_c r_N) & \dots & T_{NS}J_{\lambda_S}(k_c r_N) & \dots & T_{NN}J_{\lambda_N}(k_c r_N) \end{bmatrix}_{TM} \quad (C.5)$$

Similarly, TE modes can be given if we substitute the $J_{\lambda_k}(k_c R_k)$ with

$$J_{\lambda_k}(k_c R_k) = \frac{dJ_{\lambda_k}(k_c R_k)}{dn_k}. \quad (C.6)$$

Appendix D

Orthogonal transformation matrix for CMoL

To obtain the orthogonal transformation matrix [T] (c.f. eq. (5.12)) to diagonalize matrix [P] in eq. (5.9), we can assume λ_k^2 and t_k to be the eigenvalues and the eigenvectors of [P], respectively. From

$$\left([P] - \lambda_k^2 [I] \right) t_k = 0 \quad (\text{D.1})$$

we have

$$-t_{i-1}^{(k)} + \left(2 - \lambda_k^2 \right) t_i^{(k)} - t_{i+1}^{(k)} = 0; \quad (\text{D.2})$$

let

$$t_i^{(k)} = a_k \cos i \varphi_k + b_k \sin i \varphi_k, \quad (\text{D.3})$$

it follows that

$$t_{i \pm 1}^{(k)} = a_k \cos (i \pm 1) \varphi_k + b_k \sin (i \pm 1) \varphi_k \quad (\text{D.4})$$

or

$$t_{i \pm 1}^{(k)} = t_i^{(k)} \cos \varphi_k + \sin \varphi_k (\pm b_k \cos i \varphi_k \mp a_k \sin i \varphi_k). \quad (\text{D.5})$$

Hence

$$t_{i+1}^{(k)} + t_{i-1}^{(k)} = 2t_i^{(k)} \cos \varphi_k. \quad (\text{D.6})$$

Therefore

$$(2 - \lambda_k^2) t_i^{(k)} - 2 t_i^{(k)} \cos \varphi_k = 0. \quad (\text{D.7})$$

Since $t_i^{(k)} \neq 0$, the eigenvalues λ_k^2 then take the form of

$$\lambda_k^2 = 2 - 2 \cos \varphi_k = \left(2 \sin \frac{\varphi_k}{2} \right)^2. \quad (\text{D.8})$$

Therefore, the eigenvalues are determined except that the φ_k is still unknown. In order to obtain the φ_k , in the following we will take advantage of angular periodicity of the field distribution. Since the potential function ϕ is periodic, i.e.,

$$\phi(r, \theta_k) = \phi(r, 2\pi + \theta_k) \quad (k=1, 2, 3, \dots, N). \quad (\text{D.9})$$

Also the t_k in the MoL algorithm is periodic, i.e.,

$$t_{N+1}^{(k)} = t_1^{(k)}, \quad (\text{D.10})$$

$$t_0^{(k)} = t_N^{(k)}. \quad (\text{D.11})$$

Using this periodic condition in eq. (D.10) and eq. (D.11) yields

$$\begin{bmatrix} \cos \{ (N+1) \varphi_k \} - \cos \{ \varphi_k \} & \sin \{ (N+1) \varphi_k \} - \sin \{ \varphi_k \} \\ \cos \{ N \varphi_k \} - 1 & \sin \{ N \varphi_k \} \end{bmatrix} \begin{bmatrix} a_k \\ b_k \end{bmatrix} = 0. \quad (\text{D.12})$$

A non-trivial solution for a_k and b_k requires that the determinant of the above coefficient matrix is zero, i.e., $2 \sin \varphi_k = \sin (N+1) \varphi_k - \sin (N-1) \varphi_k$, or $\cos N \varphi_k = 1$.

This is the case for all k

$$\varphi_k = 2\pi k / N, \quad k=1, 2, 3, \dots, N. \quad (\text{D.13})$$

Now, φ_k is determined. So the eigenvalues λ_k^2 are also determined. However, the coefficients a_k and b_k of the eigenvectors t_k are still undetermined. To determine those, the orthogonality of the matrix [T] must be used. The orthogonality of the matrix [T]

requires

$$[T]^N [T] = [I], \quad (D.14)$$

where $[I]$ is an identity matrix, i.e.,

$$\sum_{k=1}^N \{t_i^{(k)}\}^2 = 1. \quad (D.15)$$

Taking the first row of the matrix $[T]$ as an example, with $i=1$, $h = 2\pi/N$ and $\varphi_k = kh$, yields

$$\sum_{k=1}^N \left\{ \frac{a_k^2 + b_k^2}{2} + \frac{a_k^2 - b_k^2}{2} \cos 2hk + a_k b_k \sin 2hk \right\} = 1. \quad (D.16)$$

We can prove that

$$\sum_{k=1}^N \sin 2hk = \frac{\sin (2N+1)h - \sin h}{2 \sin h}, \quad (D.17)$$

$$\sum_{k=1}^N \cos 2hk = \frac{\cosh h - \cos (2N+1)h}{2 \sin h}. \quad (D.18)$$

However, since $\sin Nh = \sin 2\pi = 0$, then

$$\sin (2N+1)h - \sin h = \frac{1}{2} \cos (N+1)h \times \sin Nh = 0, \quad (D.19)$$

and

$$\cos (2N+1)h - \cosh h = -\frac{1}{2} \sin (N+1)h \times \sin Nh = 0. \quad (D.20)$$

Therefore, we will have

$$\frac{a_k^2 + b_k^2}{2} = \frac{1}{N}. \quad (D.21)$$

Any coefficients that satisfy the above equation will be the solution of the problem. If

$a_k = b_k = A = \text{constant}$, then, without loss of generality, we will have the special case

$$A = 1/\sqrt{N}. \quad (\text{D.22})$$

The matrix [T] and its eigenvalues are

$$T_{ij} = \{ \cos \alpha_{ij} + \sin \alpha_{ij} \} / \sqrt{N} \quad (\text{D.23})$$

$$\lambda_k^2 = 4 (\sin (\varphi_k/2))^2 \quad (\text{D.24})$$

where

$$\alpha_{ij} = hij, \quad h = 2\pi/N, \quad \varphi_k = hk, \quad i, j, k = 1, 2, \dots, N \quad (\text{D.25})$$

Appendix E

Existence of [T] for both [P] and [Q] in the modified CMoL with $o(h^4)$ accuracy

The existence of the orthogonal matrix [T] to diagonalize both [P] and [Q] for the cylindrical MoL is proven. A construction of [T] is provided.

E.1 Modification to Helmholtz equation

In analogy to the modified MoL in Cartesian coordinates (chapter 4), when we combine eq. (5.9) at three neighboring lines $k-1$, k , and $k+1$ and choose the appropriate coefficients, we can cancel the lower order error to have a higher order accuracy. The discretized Helmholtz equations can be modified as

$$\begin{aligned} & r \frac{d}{dr} \left(r \frac{d(\phi_{k+1} + 10\phi_k + \phi_{k-1})}{12dr} \right) + k_c^2 r^2 \frac{(\phi_{k+1} + 10\phi_k + \phi_{k-1})}{12} \\ &= \frac{1}{12} (\gamma_{k+1} + 10\gamma_k + \gamma_{k-1}) \\ &+ \frac{1}{12} \left(\frac{\phi_{k+2} + 10\phi_{k+1} + \phi_k}{h^2} + 10 \frac{\phi_{k+1} + 10\phi_k + \phi_{k-1}}{h^2} + \frac{\phi_k + 10\phi_{k-1} + \phi_{k-2}}{h^2} \right) \end{aligned}$$

After we develop the Taylor's series of ϕ_{k-2} , ϕ_{k-1} , ϕ_{k+1} , and ϕ_{k+2} at ϕ_k , and denote the variables in matrix and vector forms, the right side of the above equation can be written in matrix form as

$$\bar{g} = [P] \phi - \frac{h^4}{2 \times 5!} \frac{\partial^6 \bar{\phi}}{\partial \theta^6} + o(h^6) \quad (\text{E.1})$$

Therefore, the modified CMoL in eq. (5.24) can be obtained. It has a better accuracy because that the term $o(h^2)$ has been canceled and the remaining term $o(h^4)$ represents a better accuracy.

E.2 Permutability of [P] and [Q] and existence of [T]

First of all, we will prove that two permutable matrices always have common characteristic vectors since it is easy to demonstrate that the matrix [P] and matrix [Q] in eq. (5.24) are permutable, i.e., $[P][Q]=[Q][P]$ [91]. Then we can construct the matrix [T]. Generally speaking, [T] needs not to be orthogonal to diagonalize matrix [P] and matrix [Q] simultaneously.

In order to prove the existence of [T], [P] and [Q] must have common characteristic vectors. Let \bar{t} be a characteristic vector of [P]: $[P]\bar{t}=\lambda\bar{t}$, \bar{t} is not zero. Then, since [P] and [Q] are permutable, we have $[P][Q]^k\bar{t}=\lambda[Q]^k\bar{t}$ ($k=0,1,2,3,\dots$) [91]. Suppose that in the sequence of vectors \bar{t} , $[Q]\bar{t}$, $[Q]^2\bar{t}, \dots$, the first q vectors are linearly independent, while the $(q+1)$ -th vector $[Q]^q\bar{t}$ is a linear combination of the preceding ones. Then $[S]=[\bar{t}, [Q]\bar{t}, [Q]^2\bar{t}, \dots, [Q]^{q-1}\bar{t}]$ is a subspace invariant with respect to [Q], so that in this subspace [S] there exists a characteristic vector \bar{r} of [Q]: $[Q]\bar{r}=\mu\bar{r}$, \bar{r} is not zero. On the other hand, we have shown already that the vectors \bar{t} , $[Q]\bar{t}$, $[Q]^2\bar{t}, \dots, [Q]^{q-1}\bar{t}$ are characteristic vectors of [P] corresponding to one and the same characteristic value λ . Therefore every linear combination of these vectors, and in particular \bar{r} , is a characteristic vector of [P] corresponding to λ . Thus we have proved the existence of a common characteristic vector of the matrix [P] and [Q].

E.3 Derivation of matrix [T]

In the following, we will derive the matrix [T] to diagonalize the matrix [P] and [Q]. It is known that a matrix [M] is said to be normal if it satisfies $[M][M]^t=[M]^t[M]$,

with t denoting transpose; and if a matrix $[M]$ is normal, then it can be diagonalized by an orthogonal transformation. Obviously, the matrices $[P]$ and $[Q]$ are real symmetric and positive definite, a special case of a normal matrix. Therefore, they can be diagonalized by their individual orthogonal matrices $[T_1]$ and $[T_2]$. For instance, the matrix $[P]$ can be diagonalized by an orthogonal transformation in a form of $[T_1]$

$$[T_1]^t [P] [T_1] = \begin{bmatrix} \lambda_1^2 & & & \\ & \lambda_2^2 & & \\ & & \dots & \\ & & & \dots \\ & & & & \lambda_N^2 \end{bmatrix} = [\lambda] [\lambda] \quad (\text{E.2})$$

where $[\lambda] = \text{diag}([\lambda_1^2 \lambda_2^2 \dots \lambda_k^2 \dots \lambda_N^2])$.

From the above equation, we can have

$$[P] = [T_1]^{-1} [\lambda] [\lambda] \{ [T_1]^t \}^{-1} = [T_2] [T_2]^t \quad (\text{E.3})$$

where $[T_2] = [T_1] [\lambda]$ and we will have $[T_2]^{-1} [P] \{ [T_2]^t \}^{-1} = [I]$, where $[I]$ is an identity matrix. If we let $[T] = \{ [T_2]^{-1} \}^t$, then, the above equations will be

$[T]^t [P] [T] = [I]$. On the other hand, when we multiply $[T]^t$ and $[T]$ from both sides of matrix $[Q]$, we will have

$$\begin{aligned} [T]^t [Q] [T] &= \{ [T_2]^{-1} \} [Q] \{ [T_2]^{-1} \}^t \\ &= [\lambda]^{-1} [T_1]^{-1} [Q] \{ [T_1]^{-1} \}^t \{ [\lambda]^{-1} \}^t \end{aligned} \quad (\text{E.4})$$

Since $[T_1]$ is an orthogonal matrix, $[T_1]^{-1} = [T_1]^t$. Therefore,

$$[T]^t [Q] [T] = [\lambda]^{-1} [\mu^t] [\lambda]^{-1} \quad (\text{E.5})$$

where the diagonal matrix $[\lambda]$ is given in chapter 4 as $\lambda_k^2 = 2(1 - \cos\varphi_k)$. φ_k is given in Appendix A, and $[\mu^2]$ is given below.

Denoting μ_k^2 and \bar{t}_k as the eigenvalues and eigenvectors of matrix $[Q]$, then

$$\left([Q] - \mu_k^2 [I] \right) \bar{t}_k = 0 \quad (\text{E.6})$$

where, $[I]$ is an identity matrix, and $[Q]$ is a tridiagonal one, and we have

$$t_{i-1}^{(k)} + \left(10 - 12\mu_k^2 \right) t_i^{(k)} + t_{i+1}^{(k)} = 0 \quad (\text{E.7})$$

Substituting

$$t_i^{(k)} = A_k \exp \{ j i \varphi_k \} + B_k \exp \{ -j i \varphi_k \} \quad (\text{E.8})$$

into the above equation will give

$$t_i^{(k)} \left[\left(10 - 12\mu_k^2 \right) + \left(\exp \{ j \varphi_k \} - \exp \{ -j \varphi_k \} \right) \right] = 0 \quad (\text{E.9})$$

The non-trivial solution of $t_i^{(k)}$ requires

$$\mu_k^2 = (5 + \cos\varphi_k) / 6 \quad (\text{E.10})$$

Therefore, the eigenvalues and eigenvectors are determined. The eigenvalues of matrix $[T]$ are given by eq. (E.10). The eigenvectors are given by eq. (E.8).

E.4 Continuity condition in the CMoL

The first order partial derivatives of the tangential fields along the θ -axis need to be approximated by the finite differences. It is well known that the forward and backward finite differences will have a first order error of the discretization step. So we will evaluate the first order partial derivatives in the middle between the discretization lines instead of directly on the lines themselves. In this way, central finite differences can be used which results in a second order accuracy. By following the technique used in chapter 4, a higher order accuracy of $o(h^4)$ is feasible, which will be shown below.

For the tangential fields in θ -direction, the continuity conditions can always be written in a form of

$$\begin{aligned} \frac{\partial \phi_k^I}{\partial \theta} + C \frac{\partial \phi_k^{II}}{\partial \theta} + F_k &= 0, \quad \frac{\partial \phi_k^{I,II}}{\partial \theta} = \Delta \phi_k^{I,II} + \gamma_k^{I,II}, \\ \gamma_k^{I,II} &= \frac{h^2}{4!} \frac{\partial^3 \phi_k^{I,II}}{\partial \theta^3} + \frac{h^4}{2^4 5!} \frac{\partial^5 \phi_k^{I,II}}{\partial \theta^5} + o(h^6) \end{aligned} \quad (\text{E.11})$$

where C and F_k denote the terms which are independent of the θ -derivatives, Δ is the first order central finite difference operator evaluated in between the discretization lines. If we combine the continuity condition at three lines with weighted coefficients 1, q , and 1, respectively, for $k-1$, k and $k+1$, we have

$$\begin{aligned} \frac{1}{2+q} \frac{\partial}{\partial \theta} (\phi_{k-1}^{I,II} + q \phi_k^{I,II} + \phi_{k+1}^{I,II}) &= \Delta \phi_k^{I,II} + \frac{1}{2+q} (\Delta \phi_{k-1}^{I,II} + \Delta \phi_k^{I,II} - 2 \Delta \phi_{k+1}^{I,II}) + \\ &\frac{1}{2+q} (\gamma_{k-1}^{I,II} + q \gamma_k^{I,II} + \gamma_{k+1}^{I,II}) \end{aligned} \quad (\text{E.12})$$

Then by developing the Taylor's series, we have $q=22$ in order to cancel the $o(h^2)$ -order errors, and the accuracy will be on the order of $o(h^4)$

$$\bar{\gamma} = -\frac{17h^4}{2 \times 4! \times 5!} \frac{\partial^5 \bar{\phi}^{I,II}}{\partial \theta^5} + o(h^6) \quad (\text{E.13})$$

Therefore the field continuity conditions will be

$$\frac{\beta}{\omega \epsilon_0} [D] \left(\frac{\bar{\phi}_e^I}{\epsilon_{r,I}} - \frac{\bar{\phi}_e^{II}}{\epsilon_{r,II}} \right) = [U] \left(r \frac{d\bar{\phi}_h^{II}}{dr} - r \frac{d\bar{\phi}_h^I}{dr} \right) \quad (\text{E.14})$$

$$\frac{\beta}{\omega \mu} [D] \left(\frac{\bar{\phi}_e^{II}}{\epsilon_{r,II}} - \frac{\bar{\phi}_e^I}{\epsilon_{r,I}} \right) - [U] J_z = [U] \left(r \frac{d\bar{\phi}_h^I}{dr} - r \frac{d\bar{\phi}_h^{II}}{dr} \right) \quad (\text{E.15})$$

where

$$[U] = \frac{1}{24} \begin{bmatrix} 22 & 1 & 0 & \dots & 0 & 0 & 1 \\ 1 & 22 & 1 & \dots & 0 & 0 & 0 \\ \dots & \dots & \dots & \dots & \dots & \dots & \dots \\ \dots & \dots & \dots & \dots & \dots & \dots & \dots \\ 0 & 0 & 0 & \dots & 1 & 22 & 1 \\ 1 & 0 & 0 & \dots & 0 & 1 & 22 \end{bmatrix} \quad (\text{E.16})$$

Appendix F

Matrix [T] for the modified MoL in Cartesian Coordinates

The proof of existence of the orthogonal matrix [T] to diagonalize both [P] and [Q] for Cartesian coordinates is similar to that for the cylindrical modified MoL in Appendix C. A construction of [T] in Cartesian coordinates is provided in this appendix.

First, a matrix [M] is said to be normal if it satisfies

$$[M][M]^t = [M]^t[M], \quad (\text{F.1})$$

t denotes the transpose of a matrix; from algebraic theory it is known that $[M] \in R^{n \times n}$. [M] can be diagonalized if and only if the matrix [M] is normal. Therefore a normal matrix [M] can be diagonalized by an orthogonal transformation [S], such that

$$[S]^t [M] [S] = \begin{bmatrix} \lambda_1^2 & & & & \\ & \lambda_2^2 & & & \\ & & \dots & & \\ & & & \lambda_i^2 & \\ & & & & \dots \\ & & & & & \lambda_n^2 \end{bmatrix}. \quad (\text{F.2})$$

It is also shown that a real symmetric matrix is normal. Since one can easily prove that the matrix [P] in (4.12) is normal (real symmetric), there is an orthogonal transformation [T₁] to diagonalize [P], such that

$$[T_1]' [P] [T_1] = [\lambda] [\lambda], [\lambda] = \begin{bmatrix} \lambda_1 & & & & \\ & \lambda_2 & & & \\ & & \dots & & \\ & & & \lambda_i & \\ & & & & \dots \\ & & & & & \lambda_n \end{bmatrix}. \quad (\text{F.3})$$

and due to the orthogonality of $[T_1]$ ($[T_1]^t = [T_1]^{-1}$), the above equation yields

$$[P] = ([T_1]^t)^{-1} [\lambda] [\lambda] [T_1]^{-1} = ([\lambda] [T_1]^{-1})^t ([\lambda] [T_1]^{-1}) = [W]^t [W], \quad (\text{F.4})$$

where

$$[W] = [\lambda] [T_1]^{-1} \quad (\text{F.5})$$

so

$$[W]^t [P] [W] = [I] \quad (\text{F.6})$$

Therefore, $[W]$ can diagonalize matrix $[P]$. The same matrix $[W]$ can also diagonalize matrix $[Q]$. This can be shown in the following. Since $[Q]$ is symmetric, it is not difficult to prove that $[W]^t [Q] [W]$ is also symmetric. Therefore, there is also an orthogonal matrix $[T_2]$ to diagonalize $[W]^t [Q] [W]$:

$$[T_2]^t \left([W]^t [Q] [W] \right) [T_2] = [\mu] [\mu], [\mu] = \begin{bmatrix} \mu_1 & & & & \\ & \mu_2 & & & \\ & & \dots & & \\ & & & \mu_i & \\ & & & & \dots \\ & & & & & \mu_n \end{bmatrix} \quad (\text{F.7})$$

or

$$[T]^t [Q] [T] = [\mu^2], [T] = [W] [T_2] = [T_1] [\lambda]^{-1} [T_2], \quad (\text{F.8})$$

The same matrix $[T]$ will also diagonalize $[P]$ as follows (cf. (F.6))

$$[T]^t[P][T] = ([W][T2])^t[P]([W][T2]) = [W]^t[P][W] = [I] \quad (F.9)$$

Therefore, the matrices [P] and [Q] have been diagonalized simultaneously by the matrix [T] which depends on the lateral boundary conditions. The eigenvalues and eigenvectors of matrix [P] and matrix [Q] are derived in a similar way as in Appendix C. For example, eigenvalues and eigenvectors of matrix [Q] are denoted as μ_k^2 and \bar{t}_k , respectively. The eigenvalues are derived in the following. From

$$\left([Q] - \mu_k^2 [I] \right) \bar{t}_k = 0 \quad (F.10)$$

where [I] is a unit matrix, and [Q] is a tridiagonal one, then,

$$t_k^{i-1} + \left(10 - 12\mu_k^2 \right) t_k^i + t_k^{i+1} = 0, \quad i = 2, 3, \dots, N-1. \quad (F.11)$$

Substituting

$$t_k^i = A_k \exp(ji\varphi_k) + B_k \exp(-ji\varphi_k) \quad (F.12)$$

into eq. (F.11), one can obtain

$$\left(\left(10 - 12\mu_k^2 \right) + \exp(ji\varphi_k) + \exp(-ji\varphi_k) \right) t_k^i = 0, \quad (F.13)$$

and the non-trivial solution of \bar{t}_k requires that

$$\mu_k^2 = \frac{5 + \cos\varphi_k}{6} = 1 - \frac{(\sin\varphi_k/2)^2}{3} \quad (F.14)$$

where φ_k depends on the lateral boundary conditions. For instance, for the N-D boundary conditions (Neumann and Dirichlet boundary conditions for electric field are, respectively, the left and right side walls in Fig. F.1) and the D-N (Dirichlet and Neumann) boundary conditions for magnetic field respectively at left and right lateral walls in Fig. F.1),

Appendix G

$o(h^4)$ accuracy of the MoL discretization in Cartesian coordinates

In the MoL, both Helmholtz's equation and the field continuity equations involve approximations of partial derivatives by finite differences. Therefore these approximations affect the accuracy of the MoL scheme.

G.1 Discretization of Helmholtz's equation

In abbreviated form eq. (4.2) can be written as

$$\phi''_{xx}(\phi_i) + \phi''_{yy}(\phi_i) + \kappa\phi_i = 0, i = 1, 2, 3, \dots, N, \quad (G.1)$$

where the x-variable can be discretized by straight lines (Figure G.1) with the central finite difference as

$$\phi''_{xx}(\phi_i) = \Delta_i^2 + \gamma_i, \Delta_i^2 = (\phi_{i+1} - 2\phi_i + \phi_{i-1}) / h^2. \quad (G.2)$$

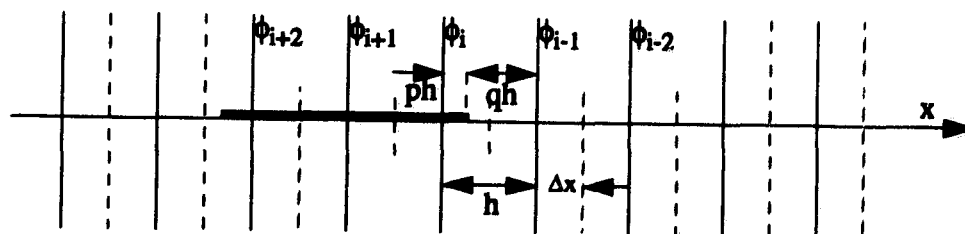


Figure G.1 MoL discretization in x-direction.

From Taylor's series expansion one obtains:

$$\phi_{i\pm 1} = \phi_i \pm h \frac{\partial}{\partial x} \phi_i + \frac{h^2}{2!} \frac{\partial^2}{\partial x^2} \phi_i \pm \frac{h^3}{3!} \frac{\partial^3}{\partial x^3} \phi_i + \frac{h^4}{4!} \frac{\partial^4}{\partial x^4} \phi_i \pm \frac{h^5}{5!} \frac{\partial^5}{\partial x^5} \phi_i + \frac{h^6}{6!} \frac{\partial^6}{\partial x^6} \phi_i + o(h^7), \quad (G.3)$$

And from here one can show that the remaining error is

$$\gamma_i = \frac{2h^2}{4!} \frac{\partial^4}{\partial x^4} \phi_i + \frac{2h^4}{6!} \frac{\partial^6}{\partial x^6} \phi_i + \frac{2h^6}{8!} \frac{\partial^8}{\partial x^8} \phi_i + o(h^8) = o(h^2). \quad (G.4)$$

Therefore, the MoL discretization of Helmholtz's equation has a second order error as shown in eq. (4.8). However it is interesting to note that if one combines eq. (G.1) and eq. (G.2) at any three neighboring lines at $i-1$, i and $i+1$ with coefficients 1 , 10 and 1 , respectively, divided by 12 , yields

$$\begin{aligned} & \{ \phi''_{i+1} + 10\phi''_i + \phi''_{i-1} \} / 12 + \Delta_i^2 + \{ \Delta_{i+1}^2 - 2\Delta_i^2 + \Delta_{i-1}^2 \} / 12 \\ & + \kappa \{ \phi_{i+1} + 10\phi_i + \phi_{i-1} \} / 12 + \gamma_i + \{ \gamma_{i+1} - 2\gamma_i + \gamma_{i-1} \} / 12 = 0. \end{aligned} \quad (G.5)$$

Comparing (G.5) with (4.10), it is evident that the discretization of Helmholtz's equation in the modified MoL has an overall error as follows

$$\begin{aligned} \gamma_{io} &= \gamma_i - \frac{1}{12} \frac{\partial^2}{\partial x^2} \{ \phi_{i+1} - 2\phi_i + \phi_{i-1} \} = \gamma_i - \frac{1}{12} \frac{\partial^2}{\partial x^2} (h^2 \Delta_i^2) \\ &= \gamma_i - \frac{h^2}{12} \frac{\partial^2}{\partial x^2} \left(\frac{\partial^2}{\partial x^2} \phi_i - \gamma_i \right) = \gamma_i - \frac{h^2}{12} \frac{\partial^4}{\partial x^4} \phi_i + \frac{h^2}{12} \frac{\partial^2}{\partial x^2} \gamma_i \\ &= \frac{2h^4}{6!} \frac{\partial^6}{\partial x^6} \phi_i + \frac{2h^6}{8!} \frac{\partial^8}{\partial x^8} \phi_i + o(h^8) + \frac{h^2}{12} \frac{\partial^2}{\partial x^2} \left\{ \frac{2h^2}{4!} \frac{\partial^4}{\partial x^4} \phi_i + \frac{2h^4}{6!} \frac{\partial^6}{\partial x^6} \phi_i + o(h^6) \right\}, \end{aligned}$$

or

$$\gamma_{io} = \frac{2h^4}{6!} \frac{\partial^6}{\partial x^6} \phi_i + \frac{2h^4}{12 \times 4!} \frac{\partial^6}{\partial x^6} \phi_i + o(h^6) = \frac{7h^4}{720} \frac{\partial^6}{\partial x^6} \phi_i + o(h^6). \quad (G.6)$$

Therefore, the discretization of Helmholtz's equation with three neighboring lines has a fourth order accuracy as shown in (4.11).

G.2 Discretization of field continuity equation

The tangential fields at interfaces between subregions involves approximations of the first order partial derivatives by finite differences. Since the forward and backward finite differences will have only \approx first order accuracy of the discretization step, the central finite differences are utilized instead to yield second order accuracy. However, by using three neighboring lines instead of two, a higher order accuracy ($o(h^4)$) is obtained.

First, when we use a central finite difference to approximate the first order partial derivatives we obtain

$$\frac{\partial}{\partial x} \phi_i = \Delta_i - \gamma_i, \Delta_i = \frac{\phi_{i+\Delta x} - \phi_{i-\Delta x}}{h}, h = 2\Delta x. \quad (\text{G.7})$$

After developing (G.7) in a Taylor's series, such that

$$\phi_{i \pm \Delta x} = \phi_i \pm \Delta x \frac{\partial}{\partial x} \phi_i + \frac{\Delta x^2}{2!} \frac{\partial^2}{\partial x^2} \phi_i \pm \frac{\Delta x^3}{3!} \frac{\partial^3}{\partial x^3} \phi_i + \frac{\Delta x^4}{4!} \frac{\partial^4}{\partial x^4} \phi_i \pm \frac{\Delta x^5}{5!} \frac{\partial^5}{\partial x^5} \phi_i + o(h^6),$$

one can find that

$$\gamma_i = \frac{\Delta x^2}{3!} \frac{\partial^3}{\partial x^3} \phi_i + \frac{\Delta x^4}{5!} \frac{\partial^5}{\partial x^5} \phi_i + o(h^6). \quad (\text{G.8})$$

Any of the field continuity equations between region k and region $k+1$ in (4.16)-(4.19) can be rewritten as

$$\frac{\partial}{\partial x} \phi_{i,k} + p \frac{\partial}{\partial x} \phi_{i,k+1} + f_i = 0, i = 1, 2, 3, \dots, N, \quad (\text{G.9})$$

which can be approximated with central finite differences in (G.7) as

$$\Delta_{i,k} - \gamma_{i,k} + p \{ \Delta_{i,k+1} - \gamma_{i,k+1} \} + f_i = 0, i = 1, 2, 3, \dots, N, \quad (\text{G.10})$$

where the discretization errors are at best of second order shown in (G.8).

Adding (G.10) at three neighboring lines together with coefficients 1, 22, and 1 respectively, then divided by 24, yields

$$\begin{aligned} & \Delta_{i,k} + \frac{1}{24} (\Delta_{i+1,k} + \Delta_{i-1,k} - 2\Delta_{i,k}) - \frac{1}{24} (\gamma_{i+1,k} + \gamma_{i-1,k} + 22\gamma_{i,k}) \\ & + p \left\{ \Delta_{i,k+1} + \frac{1}{24} (\Delta_{i+1,k+1} + \Delta_{i-1,k+1} - 2\Delta_{i,k+1}) \right. \\ & \left. - \frac{1}{24} (\gamma_{i+1,k+1} + \gamma_{i-1,k+1} + 22\gamma_{i,k+1}) \right\} + \frac{1}{24} (f_{i+1} + f_{i-1} + 22f_i) = 0 \end{aligned}$$

where

$$\begin{aligned} & \frac{1}{24} (\Delta_{i+1,m} + \Delta_{i-1,m} - 2\Delta_{i,m}) - \frac{1}{24} (\gamma_{i+1,m} + \gamma_{i-1,m} + 22\gamma_{i,m}) \\ & = \gamma_{i,m} - \frac{1}{24} \frac{\partial}{\partial x} (\phi_{i+1,m} + \phi_{i-1,m} - 2\phi_{i,m}), \quad m = k \text{ or } k+1. \end{aligned} \quad (\text{G.11})$$

The above equations can be compared to (4.23) or (4.24) and one finds that the discretization error of the modified MoL for the continuity equations is as follows

$$s_{io} = \gamma_{i,m} - \frac{h^2}{24} \frac{\partial}{\partial x} \left(\frac{\partial^2}{\partial x^2} \phi_{i,m} + \gamma_i \right),$$

where γ_i is given in (G.4) and $\gamma_{i,m}$ is given in (G.8), therefore,

$$s_{io} = \frac{\Delta x^2}{3!} \frac{\partial^3}{\partial x^3} \phi_{i,m} + \frac{\Delta x^4}{5!} \frac{\partial^5}{\partial x^5} \phi_{i,m} + o(h^6) - \frac{h^2}{24} \frac{\partial^2}{\partial x^2} \phi_{i,m} - \frac{h^2}{24} \left(\frac{2h^2}{4!} \frac{\partial^4}{\partial x^4} \phi_{i,m} + o(h^4) \right)$$

Noticing that $h = 2\Delta x$ yields

$$s_{io} = \frac{\Delta x^4}{5!} \frac{\partial^5}{\partial x^5} \phi_{i,m} - \frac{h^4}{12 \times 4!} \frac{\partial^4}{\partial x^4} \phi_{i,m} + o(h^6) = \frac{-17h^4}{8 \times 6!} \frac{\partial^4}{\partial x^4} \phi_{i,m} + o(h^6) \quad (\text{G.12})$$

Therefore a fourth order accuracy is obtained as shown in (4.25). The subscript m in the above equations denotes either k or $k+1$.

Appendix H

TE modes for homogeneous cavities

For the TE modes in the homogeneous cavities, the eigenvalue equation is the same as that in eq. (6.15)-(6.17), where the matrix elements are as follows

$$[G_{i_0 k_0}]_{N_z \times N_z} =$$

$$\begin{bmatrix} T_{11}^z T_{i_0 k_0}^\theta J_{\mu_{k_0}}'(\chi_{ik} r_{k_0 1}) & \dots & T_{j_z 1}^z T_{i_0 k_0}^\theta J_{\mu_{k_0}}'(\chi_{ik} r_{k_0 i_z}) & \dots & T_{N_z 1}^z T_{i_0 k_0}^\theta J_{\mu_{k_0}}'(\chi_{ik} r_{k_0 N_z}) \\ \dots & \dots & \dots & \dots & \dots \\ T_{1i_z}^z T_{i_0 k_0}^\theta J_{\mu_{k_0}}'(\chi_{ik} r_{k_0 1}) & \dots & T_{j_z i_z}^z T_{i_0 k_0}^\theta J_{\mu_{k_0}}'(\chi_{ik} r_{k_0 i_z}) & \dots & T_{N_z i_z}^z T_{i_0 k_0}^\theta J_{\mu_{k_0}}'(\chi_{ik} r_{k_0 N_z}) \\ \dots & \dots & \dots & \dots & \dots \\ T_{1N_z}^z T_{i_0 k_0}^\theta J_{\mu_{k_0}}'(\chi_{ik} r_{k_0 1}) & \dots & T_{j_z N_z}^z T_{i_0 k_0}^\theta J_{\mu_{k_0}}'(\chi_{ik} r_{k_0 i_z}) & \dots & T_{N_z N_z}^z T_{i_0 k_0}^\theta J_{\mu_{k_0}}'(\chi_{ik} r_{k_0 N_z}) \end{bmatrix}$$

(8.1)

Similarly χ_{ik} is given in eq.(6.8). The prime in above equation denotes the derivative of the Bessel functions.

VITA

Surname: Xiao Given Names: Shujun
Place of Birth: Jiamusi, P. R. China Date of Birth: April 24, 1963

Educational Institutions Attended:

Beijing Institute of Technology, Beijing, China	1979-1983
Beijing Institute of Technology, Beijing, China	1983-1986

Degrees Awarded:

B. S. (Honors)	Beijing Institute of Technology	1983
M.S. (Honors)	Beijing Institute of Technology	1986

Honours and Awards:

University of Victoria	Research Assistant	1990-1994
University of Victoria	Research Engineer	1994-1995
Science Council of BC	Graduate Research Engineering And Technology Award (GREAT)	1992-1995

Publications:

- [1] S. Xiao and R. Vahldieck, "Field theory analysis of circular ridge waveguides with partial dielectric filling," *1995 IEEE MTT-S International Microwave Sym. Dig.*, Orlando, Florida, May 15-19, 1995.
- [2] S. Xiao and R. Vahldieck, "Field theoretical characterization of microwave cavities," *1995 IEEE MTT-S International Microwave Sym. Dig.*, Orlando, Florida, May 15-19, 1995.
- [3] S. Xiao and R. Vahldieck, "3D FDTD simulation of superconductor coplanar waveguides," *1995 IEEE MTT-S International Microwave Sym. Dig.*, Orlando, Florida, May 15-19, 1995.

VITA. Continued

Publications, Continued:

- [4] S. Xiao and R. Vahldieck, "An extended 2D FDTD method for hybrid mode analysis of lossy and superconductor structures," *1994 IEEE AP-S International Antenna Propagat. Symposium Digest*, Seattle, WA, Jun. 1994.
- [5] S. Xiao and R. Vahldieck, "Full-wave characteristic of cylindrical layered multiconductor transmission lines using the MoL," *1994 IEEE MTT-S International Microwave Sym. Dig.*, San Diego, CA, May 23-27, 1994.
- [6] S. Xiao and R. Vahldieck, "Solution of Helmholtz equation with the method of lines in cylindrical coordinates," *1994 IEEE AP-S International Antenna Propagat. Symposium Digest*, Seattle, WA, Jun. 1994.
- [7] S.Xiao and R.Vahldieck, "Signal Propagation in Conductor-backed superconductor coplanar waveguide", *Proceedings. 24th European Microwave Conference*, pp.384-389, Cannes, France, Sept. 5-8, 1994.
- [8] S.Xiao and R.Vahldieck, "Rigorous analysis of pulse propagation on superconductor CPW", *Proceedings. Symposium on antenna technology and applied electromagnetics*, pp.589-592, Ottawa, Canada, Aug. 3-5, 1994.
- [9] S.Xiao and R.Vahldieck, "Field theory design of MHMICs using graded 3D time domain simulators with spectral estimation techniques", *Proceedings. 1994 international Conference on computational electromagnetics and its applications*, pp. 95-98, Nov. 1-4, 1994.
- [10] S.Xiao and R.Vahldieck, "Field distribution of propagation modes in superconductor coplanar transmission lines", *Proceedings. 1994 international Conference on computational electromagnetics and its applications*, pp. 470-473, Nov. 1-4, 1994.
- [11] S. Xiao and R. Vahldieck, "An improved 2D-FDTD algorithm for hybrid mode analysis of quasi-planar transmission lines," *1993 IEEE MTT-S International Microwave Symposium digest*, pp.421-424, Atlanta, Geogia, Jun. 1993.
- [12] S. Xiao and R. Vahldieck, "An efficient 2-D FDTD algorithm using real variables," *IEEE Microwave and Guided Wave Letters*, vol.3, no.5, pp.127-129, May., 1993.
- [13] S. Xiao, R. Vahldieck, and H. Jin, "A fast 2-D FDTD full wave analyzer for arbitrary guided wave structures," *IEEE Microwave and Guided Wave Letters*, vol.2, no.5, pp.165-167, May., 1992.
- [14] S. Xiao, R. Vahldieck, and H. Jin, "A fast two dimensional FDTD full-wave analyzer with adaptive mesh size," *1992 IEEE MTT-S Intern. Microwave Symp. Dig.*, pp., New Mexico, Jun. 1992.

VITA. Continued

Publications. Continued:

- [15] Z. Cai, S. Xiao, J. Bornemann and R. Vahldieck, "Tensor-based characteristic impedance calculations of microstrip on ferrite-dielectric substrates for integrated phase shifter applications", *IEE Proceedings, Vol. 139, Pt. H, pp. 125-128, Apr. 1992.*
- [16] H. Jin, R. Vahldieck, and S. Xiao, "An improved TLM full-wave analysis using a two-dimensional mesh," *1991 IEEE MTT-S Intern. Microwave Symp. Dig.*, pp.675-678 Boston, Jun. 1991.
- [17] H. Jin, R. Vahldieck, and S. Xiao, "A full-wave analysis of arbitrary guiding structures using a two-dimensional TLM mesh," *21th European Microwave Conf. Digest*, pp.370-377, Stuttgart, Germany, Sep. 1991.

PARTIAL COPYRIGHT LICENSE

I hereby grant the right to lend my dissertation to users of the University of Victoria Library, and to make single copies only for such users or in response to a request from the Library of any other university, or similar institution, on its behalf or for one of its users. I further agree that permission for extensive copying of this dissertation for scholarly purposes may be granted by me or a member of the University designated by me. It is understood that copying or publication of this dissertation for financial gain shall not be allowed without my written permission.

Title of Dissertation: Modelling of Electromagnetic Fields in MICs Based on Full-wave Space-Time Discrete Numerical Techniques

Author


(Signature)

Shujun XIAO

(Name in Block Letters)

March 29, 1996

(Date)